

EXPLORING THE PROPERTIES OF WARM AND COLD ATOMIC HYDROGEN IN THE TAURUS AND GEMINI REGIONS

HIEP NGUYEN^{1,2}, J. R. DAWSON¹, MIN-YOUNG LEE^{3,4}, CLAIRE E. MURRAY^{5,6}, SNEŽANA STANIMIROVIĆ⁷, CARL HEILES⁸,
M.-A. MIVILLE-DESCHÊNES⁹, ANITA PETZLER¹

Draft version June 18, 2019

ABSTRACT

We report Arecibo 21 cm absorption-emission observations to characterise the physical properties of neutral hydrogen (HI) in the proximity of five giant molecular clouds (GMCs): Taurus, California, Rosette, Mon OB1, NGC 2264. Strong HI absorption was detected toward all 79 background continuum sources in the $\sim 60 \times 20$ square degree region. Gaussian decompositions were performed to estimate temperatures, optical depths and column densities of the cold and warm neutral medium (CNM and WNM). The properties of individual CNM components are similar to those previously observed along random Galactic sightlines and in the vicinity of molecular clouds, suggesting a universality of cold HI properties. The CNM spin temperature (T_s) histogram peaks at ~ 50 K. The turbulent Mach numbers of CNM components vary widely, with a typical value of ~ 4 , indicating that their motions are supersonic. About 60% of the total HI gas is WNM, and nearly 40% of the WNM lies in thermally unstable regime 500–5000 K. The observed CNM fraction is higher around GMCs than in diffuse regions, and increases with increasing column density (N_{HI}) to a maximum of $\sim 75\%$. On average, the optically thin approximation (N_{HI}^*) underestimates the total column density by $\sim 21\%$, but we find large regional differences in the relationship between N_{HI} and the required correction factor, $f = N_{\text{HI}}/N_{\text{HI}}^*$. We examine two different methods (linear fit of f vs $\log_{10}(N_{\text{HI}}^*)$ and uniform T_s) to correct for opacity effects using emission data from the GALFA-HI survey. We prefer the uniform T_s method, since the linear relationship does not produce convincing fits for all subregions.

Subject headings: ISM: clouds — ISM: structure — radio lines.

1. INTRODUCTION

Neutral atomic hydrogen (HI), the most abundant gas in the interstellar medium (ISM), exists in multiple phases basically distinguished by temperature. Theoretical studies (Field et al. 1969; Silk & Werner 1969; Watson 1972; Silk 1975; McKee & Ostriker 1977; Wolfire et al. 1995, 2010) and practical observations (Radhakrishnan et al. 1972; Davies & Cummings 1975; Garwood & Dickey 1989; Liszt et al. 1993; Heiles & Troland 2003a,b) have well established a two phase model for interstellar HI gas, in which the phases (characterized by temperature and density) exist because the pressure of the ISM falls in a range where heating and cooling mechanisms permit two thermally stable states to co-exist. This model consists of cold, dense neutral medium (CNM) with kinetic temperatures $T_k \sim 30$ –200 K and volume densities of $n \sim 5$ –120

cm^{-3} , and warm, diffuse neutral medium (WNM) typically at $T_k \sim 4100$ –8800 K, $n \sim 0.03$ –1.3 cm^{-3} (McKee & Ostriker 1977; Liszt 2001; Wolfire et al. 2003). The cold gas is readily detected in HI 21 cm absorption and contributes typically 10–50% to the total HI mass (Heiles & Troland 2003a,b; Dickey et al. 2009; Stanimirović et al. 2014; Lee et al. 2015; Murray et al. 2015). The variation of the CNM fraction across interstellar environments is poorly constrained; however, it is likely higher in and around molecular clouds (Stanimirović et al. 2014, hereafter S14). The WNM can be easily detected in any direction on the sky via 21 cm emission, and plays an important role in the formation of cold gas, as well as constraining models of the interstellar medium.

The fraction of the neutral ISM that lies in the thermally unstable regime with intermediate kinetic temperatures of 500–5000 K (e.g. Dickey et al. 1977; Mebold et al. 1982; Kanekar et al. 2003; Heiles & Troland 2003a,b, hereby HT03) has been a topic of intense debate. For instance, HT03 observationally found that 48% of the total HI column density (or 30% of total out-of-plane gas) in the Arecibo Millennium survey was thermally unstable; Roy et al. (2013) estimated that at least $\sim 28\%$ of HI gas toward a sample of 33 compact extragalactic radio sources is in the unstable temperature range. From the highly sensitive 21-SPONGE survey, Murray et al. (2015) and Murray et al. (2018b) (hereafter M15 and M18, respectively) find a thermally unstable fraction of $\sim 20\%$. While these measurements (all from observations of emission/absorption pairs) are broadly consistent with a recent study by Kalberla & Haud (2018), which decomposed all-sky HI emission spectra

¹Department of Physics and Astronomy and MQ Research Centre in Astronomy, Astrophysics and Astrophotonics, Macquarie University, NSW 2109, Australia. Email: vanhiep.nguyen@hdr.mq.edu.au, nguyenvanhiepiop@gmail.com

²Australia Telescope National Facility, CSIRO Astronomy and Space Science, PO Box 76, Epping, NSW 1710, Australia

³Max-Planck-Institut für Radioastronomie, Auf dem Hugel 69, D-53121 Bonn, Germany

⁴Korea Astronomy and Space Science Institute, Daedeokdae-ro 776, 34055 Daejeon, Republic of Korea

⁵Department of Physics and Astronomy, Johns Hopkins University, Baltimore, MD 21218, USA

⁶NSF Astronomy and Astrophysics Postdoctoral Fellow

⁷Department of Astronomy, University of Wisconsin-Madison, 475 North Charter Street, Madison, WI 53706, USA

⁸Department of Astronomy, University of California, Berkeley, 601 Campbell Hall 3411, Berkeley, CA 94720-3411

⁹Laboratoire AIM, Paris-Saclay, CEA/IRFU/DAp - CNRS - Université Paris Diderot, 91191, Gif-sur-Yvette Cedex, France

from the HI4PI survey (HI4PI Collaboration et al. 2016), their estimated $\sim 41\%$ of thermally unstable HI is on the higher side relative to most recent observational studies. To keep the gas in a thermally unstable state, non-thermal processes are required, since otherwise such gas is expected to settle quickly into one of the two stable phases. Numerical ISM models suggest that dynamical processes (e.g. turbulence, shocks driven by supernova, time-dependent heating processes) may push the gas from stable phases to the thermally unstable phase (e.g. Gazol et al. 2001; Audit & Hennebelle 2005; Kim et al. 2013; Saury et al. 2014), resulting in significant amounts of unstable neutral gas. However, most recent numerical studies with detailed heating and cooling prescriptions, e.g. Kim et al. (2013); Hill et al. (2018), find a thermally unstable fraction of $< 20\%$ which is in agreement with most recent observational studies.

The measurement of HI physical properties is most commonly based on observations of the 21 cm line in emission and/or absorption. For warm HI gas at low optical depth, the column density (N_{HI}) is proportional to the brightness temperature (T_{B}) and can be directly estimated from the emission profile under the optically thin assumption, N_{HI}^* . Yet, the relation between N_{HI} and T_{B} is not as simple for cold gas, as opacity effects become significant. In that case, one needs to know both the optical depth and spin temperature to determine the true gas column density. Fortunately these can be estimated by combining the absorption and emission spectra from on-/off-source observations toward strong continuum background sources. Such studies find that in the low column density regime below $\sim 5 \times 10^{20} \text{ cm}^{-2}$, the total N_{HI} is comparable to N_{HI}^* ; but in denser regions optically thin approximation underestimates the total HI column density by at least (typically) $\sim 10\%$ (Dickey et al. 2003; HT03; Liszt 2014a; Lee et al. 2015; Nguyen et al. 2018; Murray et al. 2018a). Thus N_{HI}^* is in general a lower limit to the true N_{HI} .

On-/off-source measurements require good signal-to-noise absorption spectra, and are limited by the population of bright, compact radio continuum background sources, which precludes the creation of high-resolution, large-area Galactic maps of the true HI column density (at least in regions where the optically thin approximation is invalid). Furthermore, the derivation of true N_{HI} from these measurements can remain ambiguous due to the fact that each velocity channel contains a mixture of gas at different temperatures, and it is also possible that pencil-beam absorption measurements may under-sample the true sky distribution of dense, compact CNM structures (e.g. Fukui et al. 2018). An alternative is to use the available emission data and correct for the effects of opacity (e.g. by assuming a uniform T_{s} ; Liszt 2014b; Remy et al. 2017) or attempt to infer spin temperatures and optical depths indirectly (e.g. from dust optical depth; Fukui et al. 2015).

As a follow-up to the HI study of the Perseus molecular cloud (Stanimirović et al. 2014; Lee et al. 2015), the main goals of the present study are to (1) explore the properties of the cold and warm atomic HI gas in the proximity of five giant molecular clouds (Taurus, California, Rosette, Mon OB1, NGC 2264) as well as neighbouring diffuse and dense sightlines in and above the Galactic Plane; and (2) to build opacity-corrected HI maps by

applying optical depth corrections to emission data from the GALFA-HI survey (Stanimirović et al. 2006; Peek et al. 2011, 2018). This paper is a part of the GNOMES collaboration (the Galactic Neutral Opacity and Molecular Excitation Survey), which aims to understand the properties of neutral and molecular gas in and around molecular clouds.

There are many reasons why it is crucial to properly take into account HI opacity effects. Estimating the exact amount of each ISM phase is critical to understand the WNM-to-CNM phase transition, and to estimate the contribution made by cold optically thick HI to the so-called “dark” ISM (e.g. Grenier et al. 2005). Accurate HI column densities are also essential to test models of H_2 formation, which predict that there exists a minimum N_{HI} for H_2 formation in environments where dust shielding is dominant (compared to H_2 self-shielding); in this case, the distribution of HI column density is expected to be uniform (Krumholz et al. 2009). Interestingly, such a uniform distribution has been observed in Perseus molecular cloud by Lee et al. (2012).

Our regions of interest cover a wide range of environments, including the Galactic Plane, diffuse off-Plane sightlines and molecule-rich regions. In this work, we first employ the most direct way to estimate the optical depth, spin temperature and HI column density, by using absorption/emission spectra observed with the Arecibo radio telescope toward 79 radio continuum sources. We then derive the ratio of the “true” HI column density to the optically thin HI column density, and use this to evaluate two different methods for opacity correction.

Note that in this paper, we will define “WNM” as components detected only in emission, and “CNM” as components detected in absorption.

We organize this article as follows. In Section 2, we briefly summarize the observations and data processing techniques. In Section 3, we describe the Gaussian/pseudo-Voigt decomposition methods for absorption and emission spectral line data. In Section 4, we calculate spin temperatures, optical depths and column densities for all CNM and WNM components, and compare our results with previous observational surveys. In Section 5, we examine two methods for opacity correction and produce opacity-corrected HI maps. Finally, we summarize the results and discuss our future work.

2. OBSERVATIONS

We have conducted HI and OH absorption/emission measurements toward 79 extragalactic radio continuum sources in the vicinity of five giant molecular clouds (Taurus, California, Rosette, Mon OB1 and NGC 2264) using the Arecibo 305-m radio telescope (project a2769, PI Stanimirović). The continuum sources used in this work were selected from the NVSS catalogue (Condon et al. 1998) and have typical flux densities of $S \gtrsim 0.6 \text{ Jy}$ at 1.4 GHz. The source positions in equatorial coordinates (J2000) are presented in Figure 1. In Table 1, we list the basic information of these sources: right ascension (R.A.), declination (DEC), Galactic longitude/latitude, flux density at 1.4 GHz, and the diffuse background radio continuum emission.

The observations were conducted with Arecibo using the L-wide receiver, which permits simultaneous recording of HI (centered at 1420.406 MHz), and the two OH

TABLE 1
79 SIGHTLINES

| Sources (NVSS name) | R.A (J2000) (hh:mm:ss) | DEC (J2000) (dd:mm:ss) | l ($^{\circ}$) | b ($^{\circ}$) | $S_{1.4 \text{ GHz}}$ (Jy)* | T_{sky} (K) |
|------------------------------|---------------------------|---------------------------|-----------------------|-----------------------|--------------------------------|-------------------------|
| J034053+073525 (4C+07.13) | 03:40:53.73 | 07:35:25.40 | 178.87 | -36.27 | 1.01 | 4.07 |
| J032153+122114 (PKS0319+12) | 03:21:53.11 | 12:21:14.00 | 170.59 | -36.24 | 1.91 | 4.51 |
| J032723+120835 (4C+11.15) | 03:27:23.11 | 12:08:35.80 | 171.98 | -35.48 | 1.21 | 4.17 |
| J031857+162833 (4C+16.09) | 03:18:57.77 | 16:28:33.10 | 166.64 | -33.6 | 8.03 | 6.93 |
| J033626+130233 (3C090) | 03:36:26.56 | 13:02:33.20 | 173.15 | -33.29 | 1.99 | 4.67 |
| J035613+130535 | 03:56:13.81 | 13:05:35.80 | 177.02 | -29.78 | 0.89 | 4.14 |
| J035900+143622 (3C096) | 03:59:00.91 | 14:36:22.50 | 176.27 | -28.26 | 1.2 | 4.37 |
| J042725+085330 (4C+08.15) | 04:27:25.05 | 08:53:30.30 | 186.21 | -26.51 | 0.94 | 4.08 |
| J032504+244445 (4C+24.06) | 03:25:04.35 | 24:44:45.60 | 161.92 | -26.26 | 0.81 | 4.13 |
| J035633+190034 (4C+18.11) | 03:56:33.46 | 19:00:34.60 | 172.23 | -25.66 | 1.05 | 4.15 |
| J041140+171405 (4C+17.23) | 04:11:40.77 | 17:14:05.10 | 176.36 | -24.24 | 1.03 | 4.26 |
| J042022+175355 (3C114) | 04:20:22.17 | 17:53:55.20 | 177.3 | -22.24 | 1.11 | 4.23 |
| J042524+175525 (4C+17.25) | 04:25:24.43 | 17:55:25.30 | 178.11 | -21.31 | 0.88 | 4.16 |
| J042756+175242 (4C+17.26) | 04:27:56.98 | 17:52:42.80 | 178.56 | -20.88 | 1.01 | 4.22 |
| J044907+112128 (PKS0446+11) | 04:49:07.65 | 11:21:28.20 | 187.43 | -20.74 | 0.85 | 4.16 |
| J034008+320901 (3C092) | 03:40:08.54 | 32:09:01.30 | 159.74 | -18.41 | 1.61 | 3.95 |
| J042846+213331 (4C+21.17) | 04:28:46.64 | 21:33:31.40 | 175.7 | -18.36 | 1.34 | 4.35 |
| J040442+290215 (4C+28.11) | 04:04:42.82 | 29:02:15.90 | 166.06 | -17.22 | 0.95 | 3.69 |
| J052424+074957 (4C+07.16) | 05:24:24.04 | 07:49:57.10 | 195.51 | -15.35 | 0.82 | 4.25 |
| J051240+151723 (PKS0509+152) | 05:12:40.99 | 15:17:23.80 | 187.41 | -13.79 | 0.97 | 4.11 |
| J053239+073243 | 05:32:39.01 | 07:32:43.50 | 196.84 | -13.74 | 2.73 | 4.96 |
| J051930+142829 (4C+14.14) | 05:19:30.95 | 14:28:29.00 | 189.04 | -12.85 | 0.86 | 4.15 |
| J053450+100430 (4C+09.21) | 05:34:50.82 | 10:04:30.30 | 194.89 | -11.98 | 1.06 | 4.62 |
| J041236+353543 (4C+35.07) | 04:12:36.28 | 35:35:43.20 | 162.58 | -11.36 | 0.86 | 3.93 |
| J052109+163822 (3C138) | 05:21:09.93 | 16:38:22.20 | 187.41 | -11.34 | 8.6 | 7.59 |
| J053056+133155 (PKS0528+134) | 05:30:56.44 | 13:31:55.30 | 191.37 | -11.01 | 1.56 | 4.64 |
| J042353+345144 (3C115) | 04:23:53.25 | 34:51:44.80 | 164.76 | -10.24 | 1.3 | 3.88 |
| J060536+014512 (4C+01.17) | 06:05:36.56 | 01:45:12.70 | 206.08 | -9.37 | 0.61 | 4.07 |
| J045956+270602 (4C+27.14) | 04:59:56.09 | 27:06:02.90 | 175.83 | -9.36 | 0.93 | 3.9 |
| J051740+235110 (4C+23.14) | 05:17:40.81 | 23:51:10.20 | 180.86 | -8.01 | 0.97 | 4.32 |
| J045323+312924 (3C131) | 04:53:23.34 | 31:29:24.20 | 171.44 | -7.8 | 2.87 | 4.04 |
| J053557+175600 (4C+17.33) | 05:35:57.42 | 17:56:00.70 | 188.22 | -7.67 | 0.83 | 4.23 |
| J053444+192721 (PKS0531+19) | 05:34:44.51 | 19:27:21.70 | 186.76 | -7.11 | 7.02 | 6.48 |
| J054046+172839 (4C+17.34) | 05:40:46.05 | 17:28:39.20 | 189.21 | -6.93 | 1.47 | 4.5 |
| J050929+295755 (4C+29.16) | 05:09:29.51 | 29:57:55.80 | 174.77 | -5.97 | 1.06 | 4.03 |
| J061900+050630 | 06:19:00.21 | 05:06:30.80 | 204.66 | -4.84 | 0.69 | 4.19 |
| J062812+010926 (4C+01.19) | 06:28:12.55 | 01:09:26.00 | 209.24 | -4.64 | 0.94 | 4.27 |
| J062152+043834 (4C+04.22) | 06:21:52.90 | 04:38:34.50 | 205.41 | -4.43 | 1.06 | 4.35 |
| J062551+043540 (4C+04.24) | 06:25:51.89 | 04:35:40.20 | 205.92 | -3.57 | 0.81 | 4.28 |
| J053425+273223 (B0531+2730) | 05:34:25.73 | 27:32:23.90 | 179.87 | -2.83 | 1.04 | 4.25 |
| J061622+115553 | 06:16:22.32 | 11:55:53.90 | 198.33 | -2.2 | 0.83 | 4.41 |
| J055955+190852 (4C+19.18) | 05:59:55.70 | 19:08:52.50 | 190.09 | -2.17 | 1.03 | 4.45 |
| J060157+192216 (4C+19.19) | 06:01:57.97 | 19:22:16.30 | 190.13 | -1.64 | 0.8 | 4.43 |
| J060933+162207 (4C+16.15)** | 06:09:33.51 | 16:22:07.00 | 193.64 | -1.53 | 0.73 | 4.58 |
| J061857+133631 (4C+13.32) | 06:18:57.50 | 13:36:31.50 | 197.15 | -0.85 | 1.96 | 4.86 |
| J054844+263600 (4C+26.18)** | 05:48:44.28 | 26:36:00.30 | 182.36 | -0.62 | 1.16 | 3.98 |
| J054211+290147 (4C+29.19) | 05:42:11.81 | 29:01:47.80 | 179.53 | -0.59 | 0.98 | 4.13 |
| J063313+081318 (4C+08.21) | 06:33:13.01 | 08:13:18.90 | 203.54 | -0.27 | 1.1 | 4.46 |
| J060351+215937 (4C+22.12) | 06:03:51.56 | 21:59:37.50 | 188.07 | 0.04 | 2.77 | 5.15 |
| J062141+143211 (3C158) | 06:21:41.09 | 14:32:11.90 | 196.64 | 0.17 | 2.24 | 4.86 |
| J063215+102201 (4C+10.20) | 06:32:15.34 | 10:22:01.10 | 201.53 | 0.51 | 2.38 | 5.0 |
| J062545+144019 (4C+14.18) | 06:25:45.97 | 14:40:19.70 | 196.98 | 1.1 | 2.44 | 5.01 |
| J064516+053132 (3C167) | 06:45:16.84 | 05:31:32.00 | 207.31 | 1.15 | 1.33 | 4.76 |
| J053752+361112 (4C+36.10) | 05:37:52.39 | 36:11:12.90 | 172.98 | 2.44 | 1.04 | 4.34 |
| J062019+210229 | 06:20:19.54 | 21:02:29.70 | 190.74 | 2.94 | 0.9 | 4.33 |
| J062250+220025 (4C+22.16) | 06:22:50.64 | 22:00:25.60 | 190.16 | 3.91 | 1.06 | 4.34 |
| J065601+083407 (4C+08.23) | 06:56:01.03 | 08:34:07.10 | 205.81 | 4.91 | 0.68 | 4.12 |
| J063451+190940 | 06:34:51.38 | 19:09:40.90 | 193.99 | 5.1 | 0.84 | 4.31 |
| J065917+081331 | 06:59:17.97 | 08:13:31.80 | 206.48 | 5.48 | 0.91 | 4.12 |
| J065548+104258 (4C+10.21) | 06:55:48.36 | 10:42:58.80 | 203.85 | 5.82 | 0.91 | 4.15 |
| J064841+144020 (4C+14.20) | 06:48:41.15 | 14:40:20.60 | 199.52 | 6.04 | 1.03 | 4.17 |
| J071523+031105 (4C+03.12) | 07:15:23.75 | 03:11:05.00 | 212.82 | 6.78 | 0.67 | 3.97 |
| J071004+061705 (4C+06.28) | 07:10:04.83 | 06:17:05.40 | 209.43 | 7.0 | 0.58 | 4.05 |
| J071924+021035 | 07:19:24.88 | 02:10:35.80 | 214.18 | 7.22 | 0.66 | 3.87 |
| J064524+212145 (3C166) | 06:45:24.08 | 21:21:45.70 | 193.12 | 8.3 | 2.59 | 4.8 |
| J071028+091954 (4C+09.27) | 07:10:28.52 | 09:19:54.30 | 206.72 | 8.44 | 1.02 | 4.09 |
| J072140+053050 (PKS0719+056) | 07:21:40.87 | 05:30:50.90 | 211.43 | 9.23 | 0.83 | 4.01 |
| J070001+170922 | 07:00:01.52 | 17:09:22.30 | 198.47 | 9.58 | 0.65 | 4.09 |
| J065937+211742 (4C+21.22) | 06:59:37.81 | 21:17:42.20 | 194.63 | 11.26 | 0.57 | 3.98 |
| J071404+143620 (3C175.1) | 07:14:04.70 | 14:36:20.90 | 202.29 | 11.53 | 1.93 | 4.38 |
| J072551+103202 (4C+10.22) | 07:25:51.27 | 10:32:02.30 | 207.31 | 12.37 | 1.23 | 4.09 |
| J070937+195443 (4C+19.26) | 07:09:37.27 | 19:54:43.00 | 196.91 | 12.8 | 0.69 | 4.03 |
| J072525+123624 (PKS0722+12) | 07:25:25.60 | 12:36:24.60 | 205.35 | 13.17 | 0.61 | 3.77 |
| J072832+121010 (4C+12.30) | 07:28:32.88 | 12:10:10.50 | 206.09 | 13.67 | 1.07 | 3.92 |
| J072516+142513 (4C+14.23) | 07:25:16.80 | 14:25:13.50 | 203.64 | 13.91 | 1.07 | 3.87 |
| J072810+143736 (3C181) | 07:28:10.26 | 14:37:36.00 | 203.75 | 14.63 | 2.3 | 4.53 |
| J071810+201002 (PKS0715+20) | 07:18:10.64 | 20:10:02.70 | 197.52 | 14.74 | 0.73 | 3.98 |
| J073035+151512 (4C+15.20) | 07:30:35.41 | 15:15:12.60 | 203.42 | 15.42 | 1.54 | 4.23 |
| J073037+173951 (4C+17.41) | 07:30:37.09 | 17:39:51.50 | 201.13 | 16.42 | 0.69 | 3.94 |

*Condon et al. (1998)

**Excluded from the analysis

ground-state main lines at 1665.402 and 1667.359 MHz, with a velocity resolution of 0.16 km s^{-1} and an angular resolution of $3'.5$ at these frequencies.

We use the same observing procedure described in detail by Heiles & Troland (2003a). Briefly, we make a 17 data point observation (so-called Z16), consisting of one on-source absorption spectrum at the position of the background radio source, and 16 off-source emission spectra with innermost positions located at 1.0 HPBW and the outermost positions at $\sqrt{2}$ HPBW from the central source. This particular observation pattern was designed to measure the fluctuations of 21 cm intensity within an area with an angular diameter of $\sim 13'.5$ around the source, and take these spatial variations into account to derive an accurate off-source “expected” emission spectrum (T_{exp} , the emission profile we would observe in the absence of the radio source; see Section 3 for details of the T_{exp} derivation). Our integration time, on average, is ~ 1 hour per source (including all on- and off-source integrations); leading to a characteristic noise level in optical depth of $\sim 5 \times 10^{-3}$ per 1 km s^{-1} velocity channel.

In the 21-SPONGE survey, M15 apply a main beam efficiency of 0.94 to Arecibo emission spectra taken with the L-wide receiver. To verify that this factor is also appropriate for our dataset, we compare our T_{exp} profiles with emission data from the Arecibo GALFA-HI survey (Data Release 2, DR2; Peek et al. 2018). We extract the GALFA-HI emission spectra around the location of each source within the outermost angular radius of the Z16 observation pattern, excluding the central pixels inside the Arecibo main beam (since these may be affected by absorption), and average the remaining pixels. We then compare the resultant spectra with our T_{exp} profiles on a channel-by-channel basis, for all channels above our 5σ noise level, and find that the T_{exp} values from the present work are systematically lower by a factor of ~ 1.06 (standard deviation of 0.08). Similarly, our T_{exp} integrated intensities are found to be systematically lower than GALFA-HI by the same factor of ~ 1.06 (standard deviation of 0.04). We also make the same comparison using the Leiden-Argentine-Bonn (LAB, Hartmann & Burton 1997; Kalberla et al. 2005) and HI4PI (HI4PI Collaboration et al. 2016) surveys. While these have lower resolutions than Arecibo ($36'$ and $16'$ respectively), they are both stray-radiation-corrected and have excellent absolute calibration. We find a consistent factor of ~ 1.07 (standard deviation of 0.07). We therefore apply a beam efficiency factor of $\eta_b = 1/1.07 = 0.93$ to our data.

Note that while we do not attempt to correct for the effects of stray radiation in our data, visual inspection of our spectra reveal no strong signs of the broad, wide wings that typically characterise such contamination. Peek et al. (2011) note that contamination from stray radiation in GALFA-HI is small – typically within their 1σ uncertainties. Once the main beam efficiency has been applied, the absolute differences between our spectra and those of GALFA-HI are also small; specifically, on a velocity channel basis, the difference spectra have broad features, but these mostly fall within the 2σ uncertainty profiles of our $T_{\text{exp}}(v)$. This results in a relative difference of at most 12% between the optically thin column densities of the two surveys along our 79 sightlines, with a

median difference of $(2.0 \pm 1.1)\%$ (the uncertainty of the median is estimated by bootstrap re-sampling). Thus, our visual inspection suggests that while stray radiation is likely present at a low level, its contribution to our profiles is not significant enough to affect our scientific conclusions.

3. DATA ANALYSIS: HI ABSORPTION & EMISSION FITTING

The root of the analysis is to solve the two equations of radiative transfer for on-/off-source measurements, under the assumption that the on and off positions sample the same gas:

$$T_{\text{B}}^{\text{ON}}(v) = (T_{\text{bg}} + T_{\text{c}})e^{-\tau_v} + T_{\text{s}}(1 - e^{-\tau_v}), \quad (1)$$

$$T_{\text{B}}^{\text{OFF}}(v) = T_{\text{bg}}e^{-\tau_v} + T_{\text{s}}(1 - e^{-\tau_v}), \quad (2)$$

$$T_{\text{exp}}(v) = T_{\text{B}}^{\text{OFF}}(v) - T_{\text{bg}}. \quad (3)$$

Hence:

$$e^{-\tau_v} = \frac{T_{\text{B}}^{\text{ON}}(v) - T_{\text{B}}^{\text{OFF}}(v)}{T_{\text{c}}}. \quad (4)$$

In the above, $T_{\text{B}}^{\text{ON}}(v)$ and $T_{\text{B}}^{\text{OFF}}(v)$ are the brightness temperatures of the on-source and off-source profiles respectively, T_{s} is the spin temperature, τ_v is the optical depth, T_{c} is the brightness temperature of the continuum source, and T_{bg} is the background brightness temperature including the 2.725 K isotropic radiation from the CMB and the Galactic synchrotron background at the source position. We obtain T_{bg} from the 1.4 GHz radio continuum maps of CHIPASS (in the Southern sky Calabretta et al. 2014) and from the Stockert and Villa-Elisa telescopes (for the Northern sky Reich et al. 2001), with typical values of around 4.4 K.

Following HT03, we derive T_{exp} , the “expected” emission profile at the location of the background source. We express the 16 off-source spectra as both first and second order Taylor series expansions of T_{exp} , plus a small contribution from the source intensity attenuated by optical depth, and perform a least-squares fit for the 17-point measurements to derive simultaneously: (1) the on-source optical depth profile ($e^{-\tau_v}$), (2) the off-source expected emission spectrum as well as its spatial derivatives, (3) their uncertainty profiles: σ_{τ} (also $\sigma_{e^{-\tau}}$) and $\sigma_{T_{\text{exp}}}$. Here, we use a slightly simpler approach than HT03, by not including their fine-tuning for gain variation, under the assumption that an accurate knowledge of the spatially-varying telescope gain and beam-shape properties is required to properly account for the off-source gain. As pointed out by Stanimirović et al. (2014), we also find that the second-order Taylor expansion is noisier (because the higher order variation in HI emission requires more fitting parameters) but likely better models the actual complex variations in HI emission and thus is the more accurate approach. We therefore use the $T_{\text{exp}}(v)$ and $\tau(v)$ profiles from the second-order expansion for all sources.

In this paper, to estimate the physical properties of individual HI clouds along a sightline, we follow the methodology applied by Heiles & Troland (2003a) to the Millennium Survey HI profiles. Essentially we assume

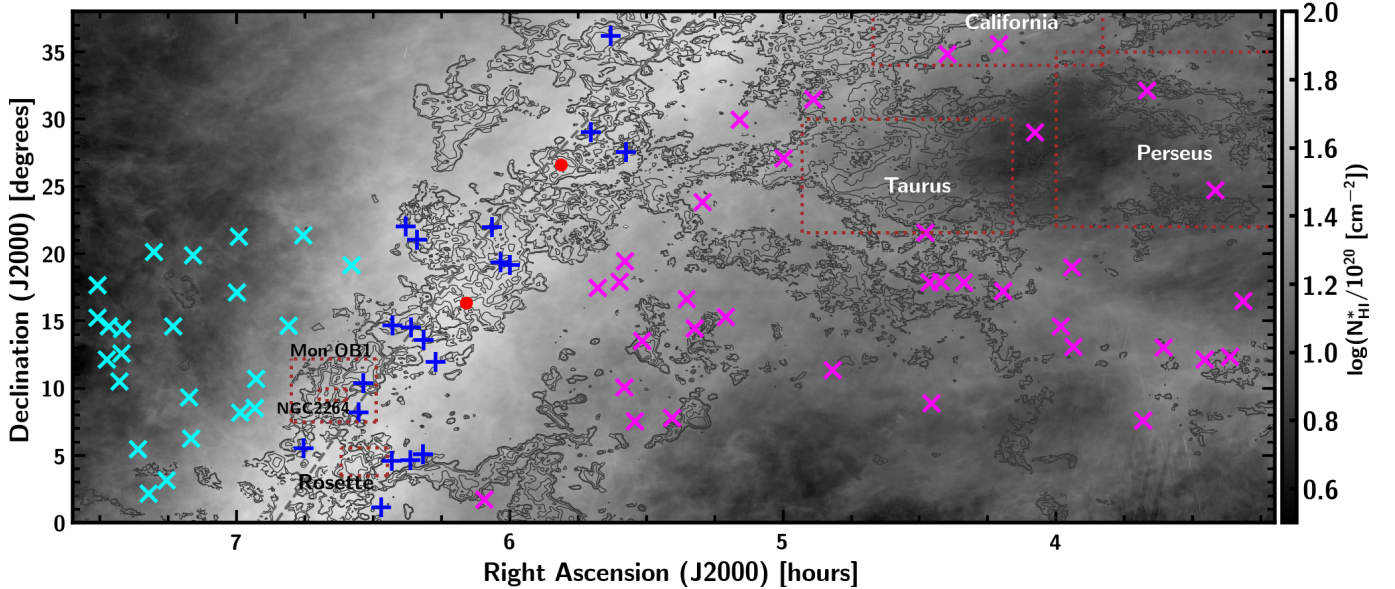


FIG. 1.— Locations of all 79 background radio continuum sources considered in this study, overlaid on the map of HI column density N_{HI}^* from the Arecibo GALFA-HI survey (DR2; Peek et al. 2018). The N_{HI}^* range is $(1-80) \times 10^{20} \text{ cm}^{-2}$. The blue plus markers show the sightlines toward 19 radio sources near the Galactic plane ($|b| < 5^\circ$), cyan crosses show the 23 sightlines above the Galactic plane, magenta crosses show the 35 sightlines below the Galactic plane, and the red dots show the two saturated sightlines excluded from the analysis (4C+16.15 and 4C+26.18). The dashed line shows the Galactic plane (Galactic latitude $b = 0^\circ$). Dotted boxes show roughly the locations of five molecular clouds. The contours represent the logarithm of integrated intensity $W_{\text{CO}(1-0)}$ from the all-sky extension to the maps of Dame et al. (2001) (T. Dame, private communication). The levels are $[0.01, 0.25, 0.75, 1., 1.75]$ in units of $\log_{10}(\text{K km s}^{-1})$.

cold gas (‘CNM’) components are seen in both absorption and emission (i.e. in both opacity and brightness temperature profiles), and warm gas (‘WNM’) is seen only in emission, giving only a brightness temperature (see Heiles & Troland 2003a for further detail). A key difference in the present work, however, is that besides Gaussian profile fitting, we also carry out pseudo-Voigt fitting, to examine whether the derived properties are affected by the choice of profile shape. Each Gaussian has three free parameters, and each pseudo-Voigt has four (see Section 3.3 for details).

3.1. Initial Component Generation

The opacity and expected emission profiles consist of multiple components at different velocities. A crucial question is how many components should be added to fit each spectrum. The noise level of the spectrum and residuals of the fit can be used as a measure of the goodness of the fit. However, while adding more components will naturally reduce the residuals, it may result in overfitting, and may not necessarily reflect physical reality. To minimise subjective judgment as much as possible, we generate a common set of initial guesses for both Gaussian and pseudo-Voigt fittings using a Savitzky-Golay filter for peak/trough detections. Note that the numbers of CNM and WNM components from these common initial guesses are not optimized for both types of fittings. We then employ the Bayesian Information Criterion (BIC) to automatically obtain the number of fit components, N_C , for the absorption ($e^{-\tau(v)}$) and emission spectra ($T_{\text{exp}}(v)$):

$$BIC = \chi^2 + d \ln(N) \quad (5)$$

where χ^2 is the chi-squared from the fit, d is the

number of free parameters (which is proportional to N_C , e.g. $d = 3N_C$ for Gaussians, and $d = 4N_C$ for pseudo-Voigts) and N is the sample size. Clearly, the BIC adds a new term to χ^2 to penalize the number of parameters in the model. For two given models, the model with the lower value of BIC is preferred. We calculate the BIC value for each value of d , and adopt the number of components from the most preferred d (see also Allison et al. 2012; Gordon et al. 2017). After this step, we have two sets of initial guesses for the Gaussian and pseudo-Voigt fittings, each with typically a different number of components. In the few cases where the spectra are either noisy or marginally saturated, we slightly adjust the initial guesses (central velocities and number of components) to allow the fits to converge.

3.2. Gaussian spectral decomposition

In this section, we decompose both the absorption and emission spectra into sets of Gaussian components. The expected emission profile $T_{\text{exp}}(v)$ consists of both warm and cold components:

$$T_{\text{exp}}(v) = T_{\text{B,CNM}}(v) + T_{\text{B,WNM}}(v) \quad (6)$$

where $T_{\text{B,CNM}}(v)$ is the brightness temperature of the cold gas and $T_{\text{B,WNM}}(v)$ is the brightness temperature of the warm gas. The on-source spectrum (Equation 4) contains only cold gas seen in absorption.

First, we fit the opacity spectrum $\tau(v)$ with a set of N Gaussian components using a least-squares method with the assumption that each component is independent and isothermal with a spin temperature $T_{\text{s},n}$:

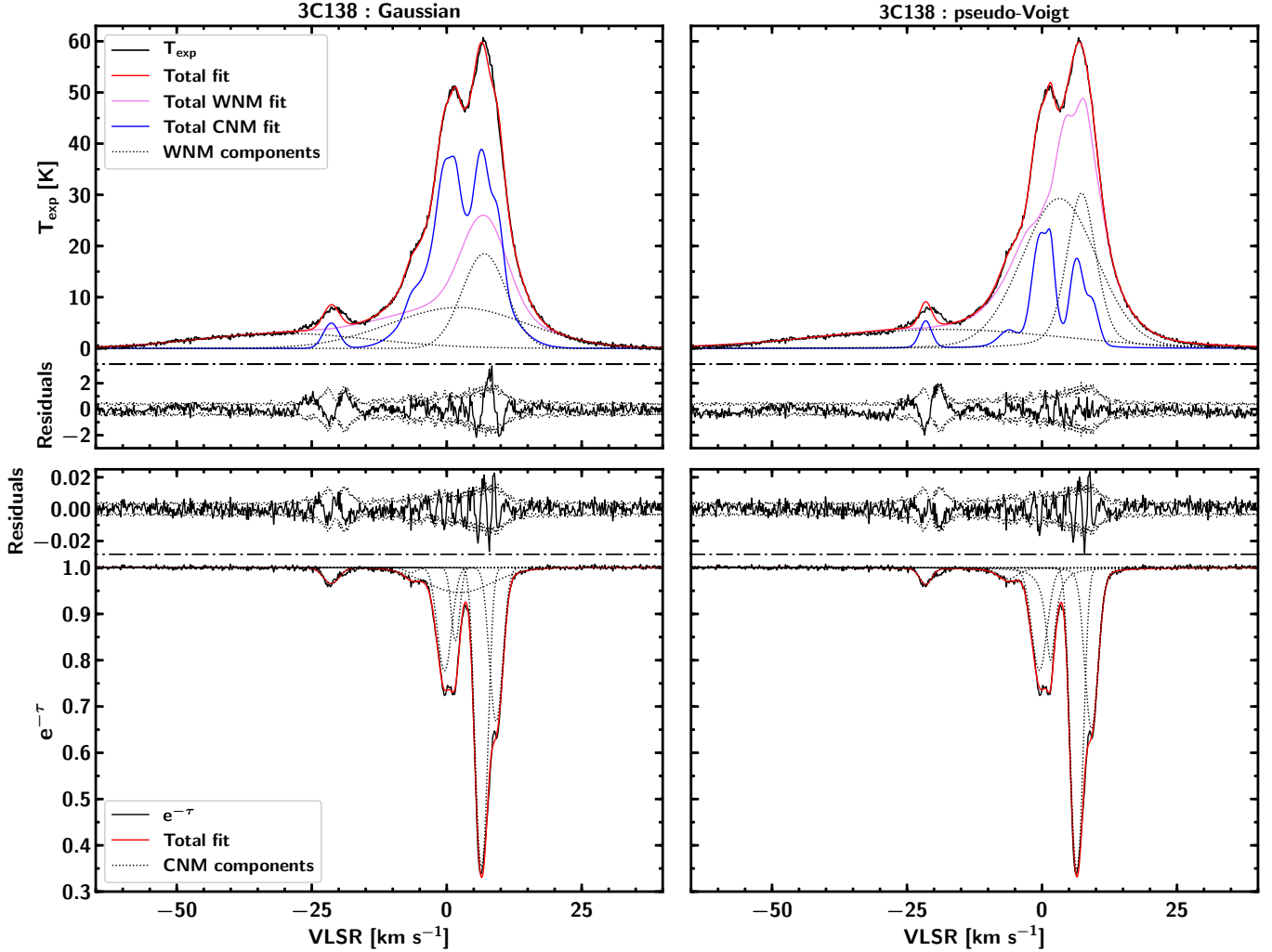


FIG. 2.— Example of Gaussian (left) and pseudo-Voigt (right) fits to a pair of emission and absorption spectra. In the upper panels, the black solid line is the expected emission profile T_{exp} ; the black dotted lines are the WNM Gaussian/pseudo-Voigt components; the pink line shows the contribution of the WNM components to the T_{exp} profile; the blue line displays the contribution to the T_{exp} profile by the CNM components from the absorption profile; the red solid line is the total WNM and CNM fit. The residuals from the fit are plotted below zero, with $\pm\sigma_{T_{\text{exp}}}$ superimposed. In the lower panels, the black line shows the optical depth profile ($e^{-\tau}$); the dotted lines are the CNM Gaussian/pseudo-Voigt components, the red line represents the fit to the optical depth profile. The residuals from the absorption fit are plotted above one, with $\pm\sigma_{e^{-\tau}}$ superimposed. The derivation of uncertainty profiles ($\sigma_{T_{\text{exp}}}$ and $\sigma_{e^{-\tau}}$) is described in Section 3.

$$\tau(v) = \sum_{n=0}^{N-1} \tau_{0,n} e^{-4\ln 2 [(v-v_{0,n})/\delta v_n]^2}. \quad (7)$$

Here the parameters used to fit the absorption spectrum, $\tau_{0,n}$, $v_{0,n}$, δv_n are respectively the peak optical depth, central velocity and FWHM of n^{th} component. These parameters are assumed to be independent, and the number of components and the initial guesses for the fit parameters are generated as described in Section 3.1. This least-squares fit gives all the values of $\tau_{0,n}$, $v_{0,n}$ and δv_n .

We now fix all the parameters derived for these CNM components (namely $\tau_{0,n}$, $v_{0,n}$ and δv_n). Next, we also use the least squares technique to fit the expected emission profile, $T_{\text{exp}}(v)$, which is assumed to consist of the N cold components seen in the absorption spectrum, plus any warm components seen only in emission. The con-

tribution of the cold components is given by

$$T_{\text{B,CNM}}(v) = \sum_{n=0}^{N-1} T_{s,n} (1 - e^{-\tau_n(v)}) e^{-\sum_{m=0}^{M-1} \tau_m(v)} \quad (8)$$

in which the subscript m describes M absorption clouds lying in front of the n^{th} cloud. For WNM, we use a set of K Gaussian functions to represent the contribution to the expected profile $T_{\text{exp}}(v)$, (where the number of components and their initial guesses are also generated as described in Section 3.1). For each k^{th} component, we assume that a fraction F_k of WNM lies in front of all CNM components, so the remaining $(1 - F_k)$ lies behind and is absorbed by CNM components. Therefore, the brightness temperature from these K WNM components is:

$$T_{\text{B,WNM}}(v) = \sum_{k=0}^{K-1} [F_k + (1 - F_k)e^{-\tau_v}] \times T_{0,k} e^{-4\ln 2 [(v-v_{0,k})/\delta v_k]^2} \quad (9)$$

Here the independent fit parameters $T_{0,k}$, $v_{0,k}$, δv_k are respectively the peak brightness temperature, central velocity and FWHM of the k^{th} emission component. This least-squares fit to the emission spectrum gives $T_{0,k}$, $v_{0,k}$, δv_k , F_k for warm components and $T_{s,n}$ for cold components. For each sightline, we perform the $T_{\text{exp}}(v)$ fit with all possible orderings of the N absorption components ($N!$), and choose the one that gives the smallest residuals. As seen in Equation 9, the fraction F_k determines the contribution of $T_{\text{B,WNM}}$ to T_{exp} and so it has an important effect on the derived CNM spin temperatures ($T_{s,n}$). However, the results of the F_k fractions from different CNM ordering fits are difficult to distinguish statistically by the difference in the fit residuals. Hence, following the suggestion in HT03, after including K WNM emission-only components, we calculate the spin temperature of CNM by assigning three values (0, 0.5, 1) to each F_k . We then experiment with all possible combinations of K WNM components (3^K) along the line of sight. We obtain the final spin temperatures $T_{s,n}$ for CNM components as a weighted average over all trials, and the weight of each trial is the inverse of the variance estimated from the residuals the $T_{\text{exp}}(v)$ fit. The uncertainty of the final spin temperature for each CNM component is estimated from the variations in T_s with F_k in all trials (as described in Section 3.5 of Heiles & Troland 2003a). Apart from the dependence of CNM T_s on the ordering of the N CNM components and the fraction F_k , we do not observe strong correlations between other independent CNM and WNM Gaussian parameters. Example spectra and fits are shown in Figures 2 and 3.

3.3. Pseudo-Voigt spectral decomposition

Gaussian fitting has been widely used in ISM radio astronomy because the velocity profiles are assumed to be truly Gaussian. This assumption holds when internal motions are characterized by thermal processes or small-scale turbulence, and the damping wings in the spectra are insignificant. However, some authors have chosen to fit pseudo-Voigt profiles instead (Planck Collaboration et al. 2015; Remy et al. 2017), with the reasoning that pseudo-Voigt function fits broad pedestals better. Therefore, we have tested both options in this work and assess the impact (if any) on the astrophysical conclusions (see Appendix A for more details).

We repeat the above fitting procedures using pseudo-Voigt functions instead of pure Gaussians. A pseudo-Voigt profile, a simple approximation for the Voigt function (Wertheim et al. 1974), is a linear combination of a Gaussian curve $G(x)$ and a Lorentzian curve $L(x)$ sharing the same full width at half-maximum values. The normalized pseudo-Voigt profile by definition is given by:

$$V(x) = \eta L(x) + (1 - \eta)G(x) \quad (10)$$

where $L(x)$ and $G(x)$ are the normalized Gaussian and Lorentzian functions, with FWHM $\delta_V = \sqrt{2(\ln 2)}\delta_G = 2\delta_L$:

$$G(x) = \frac{1}{\sqrt{\pi}\delta_G} e^{-x^2/\delta_G^2} \quad (11)$$

$$L(x) = \frac{1}{\pi\delta_L} \left(\frac{1}{1 + x^2/\delta_L^2} \right) \quad (12)$$

and η is a parameter which mixes the two functions. The results for the pseudo-Voigt fits are shown in Table 3; example spectra and fits are shown in Figures 2 and 3.

4. RESULTS

In Table 3 we list the parameters obtained from both the pseudo-Voigt and Gaussian fits for all CNM and WNM components along each sightline. Column 1 shows the Galactic longitude and latitude for each sightline; Columns 2 and 10 list the peak brightness temperature for each component. For the WNM components, this is the unabsorbed height T_{B} , quoted with its error from the fits. For the CNM components, this is the spin temperature obtained from the fits multiplied by $(1 - e^{-\tau})$ (see Equation 8), and is quoted without uncertainty. In Columns 3 and 11, we list the optical depth of each component: for CNM components this is the peak optical depth and its associated uncertainty, for WNM components it is the upper limit to peak opacity (set to be equal to the 1σ noise level in absorption at the central velocity of the emission component) and its error is not quoted. Columns 4 and 12 show the central velocities for each CNM and WNM component; Columns 5 and 13 are the linewidth (FWHM) in VLSR of each CNM and WNM component; Columns 7 and 14 list the spin temperatures: for CNM components the spin temperature is derived from the fit to the T_{exp} profile and is quoted with its error, for WNM components T_s is a lower limit calculated by the upper limit on optical depth in Columns (3, 11) $T_{s,k} = T_{0,k}/\tau_{0,k}$ and has a very large error. In Columns 8 and 15, we quote the HI column densities and their errors for each CNM and WNM component; Columns 9 and 16 are the fraction (F) of each WNM component lying in front of all CNM components or the order (O) of each CNM component along the sightline (integer numbers). The η values in Column 6 are the fractions of the Lorentzian function in the pseudo-Voigt profile. Note that while we detect HI absorption along all 79 sightlines, we exclude two sightlines (4C+16.15 and 4C+26.18) from further analysis because their opacity spectra ($e^{-\tau}$) are saturated and result in huge optical depths with enormous uncertainties.

Along the remaining 77 sightlines, the total numbers of CNM components from the Gaussian and pseudo-Voigt fits are (349, 323), with column densities of $(956.1, 1013.8) \times 10^{20} \text{ cm}^{-2}$. The numbers of WNM components are (327, 284), with column densities of $(1609.7, 1712.5) \times 10^{20} \text{ cm}^{-2}$. Thus the total (WNM+CNM) column densities derived from Gaussian and pseudo-Voigt fits in this study are $(2565.8, 2726.3) \times 10^{20} \text{ cm}^{-2}$, which equates to cold and warm gas fractions of 40% and 60%.

The distributions of properties derived from Gaussian and pseudo-Voigt fits are almost indistinguishable. For consistency with past studies, we will present the results of the Gaussian fits for the rest of this paper, however, we present a detailed comparison between the Gaussian and pseudo-Voigt fits in the Appendix A.

Figures 4, 5 and 6 show the absorption and emission spectra for all sightlines, in the Galactic Plane, Gemini and Taurus regions respectively. In a few cases, we see the presence of ‘‘emission’’ features in absorption spectra ($e^{-\tau} > 1$) toward the weakest background sources. These sources are probably quite faint to measure the HI absorption with Arecibo telescope, thus their derived

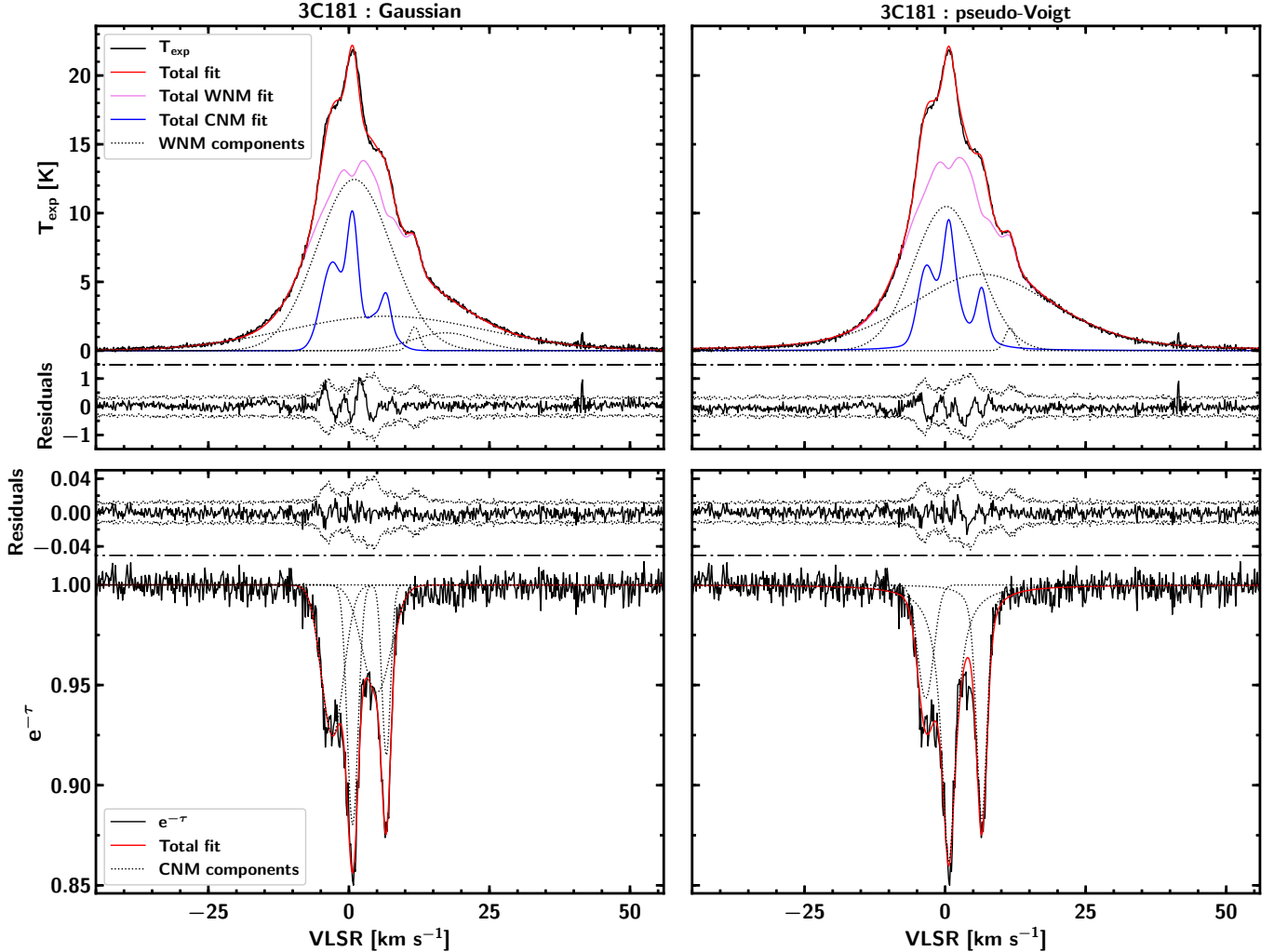


FIG. 3.— See Figure 2 for details.

absorption spectra are essentially noisier. During the spectral decompositions, we do not take these “emission” features into the fit.

Here (and from hereon) we define the ‘Galactic Plane’ as $|b| < 5^\circ$ (19 sightlines), including Rosette, Mon OB1 and NGC 2264; the ‘Gemini region’ as $b > 5^\circ$ (23 sightlines), including minimal molecular gas; and the ‘Taurus region’, including both Taurus and California, as $b < -5^\circ$ (35 sightlines) (as illustrated in Figure 1). These latitude divisions (basically based on the distribution of $W_{\text{CO}(1-0)}$ from Dame et al. 2001) roughly divide our sample into three characteristic physical regimes – in-Plane, out-of-Plane with mostly diffuse sightlines (Gemini) and out-of-Plane with many dense/molecular sightlines (Taurus). The colors in the absorption spectra in the plots indicate the HI spin temperature of each CNM component. In general, we detect strong absorption and emission in a wide range of VLSR from -10 to 50 km s^{-1} for sightlines in Gemini, from -20 to 20 km s^{-1} for those in Taurus and -50 to 50 km s^{-1} near the Galactic plane. The strongest absorption/emission is located at $\sim 0 \text{ km s}^{-1}$, and the closer to the Galactic plane, the more complex the profile shapes.

Besides the spectral decompositions, we also applied two alternative methods (one T_s per velocity channel and

single harmonic-mean T_s along full sightline) to estimate the HI spin temperature and column density from the absorption/emission pairs. We compare the results obtained from these different approaches in Appendix B.

4.1. Optical depth

The peak optical depths, τ_{peak} , derived from Gaussian fitting range from ~ 0.01 to 16.2 . The values are summarized in histograms in Figure 7 (top panel), where we show the τ_{peak} distribution for all CNM components, as well as for each individual region. As expected, the optical depths in the Galactic plane sample are the highest, with a mean and median of $(1.0, 0.63)$, and also relatively high toward Taurus, with mean and median values $(0.54, 0.37)$ – triple those toward the Gemini region $(0.18, 0.13)$. The mean and median values for the total sample are ~ 0.64 and ~ 0.35 . About 17% of the CNM components have $\tau_{\text{peak}} > 1$, namely 60/349 Gaussian components; corresponding to dense gas regions. As shown in bottom panel of Figure 7, the locations of these high optical depths are all either coincident with or close to sightlines with CO detections.

4.2. Temperatures of cold and warm gas

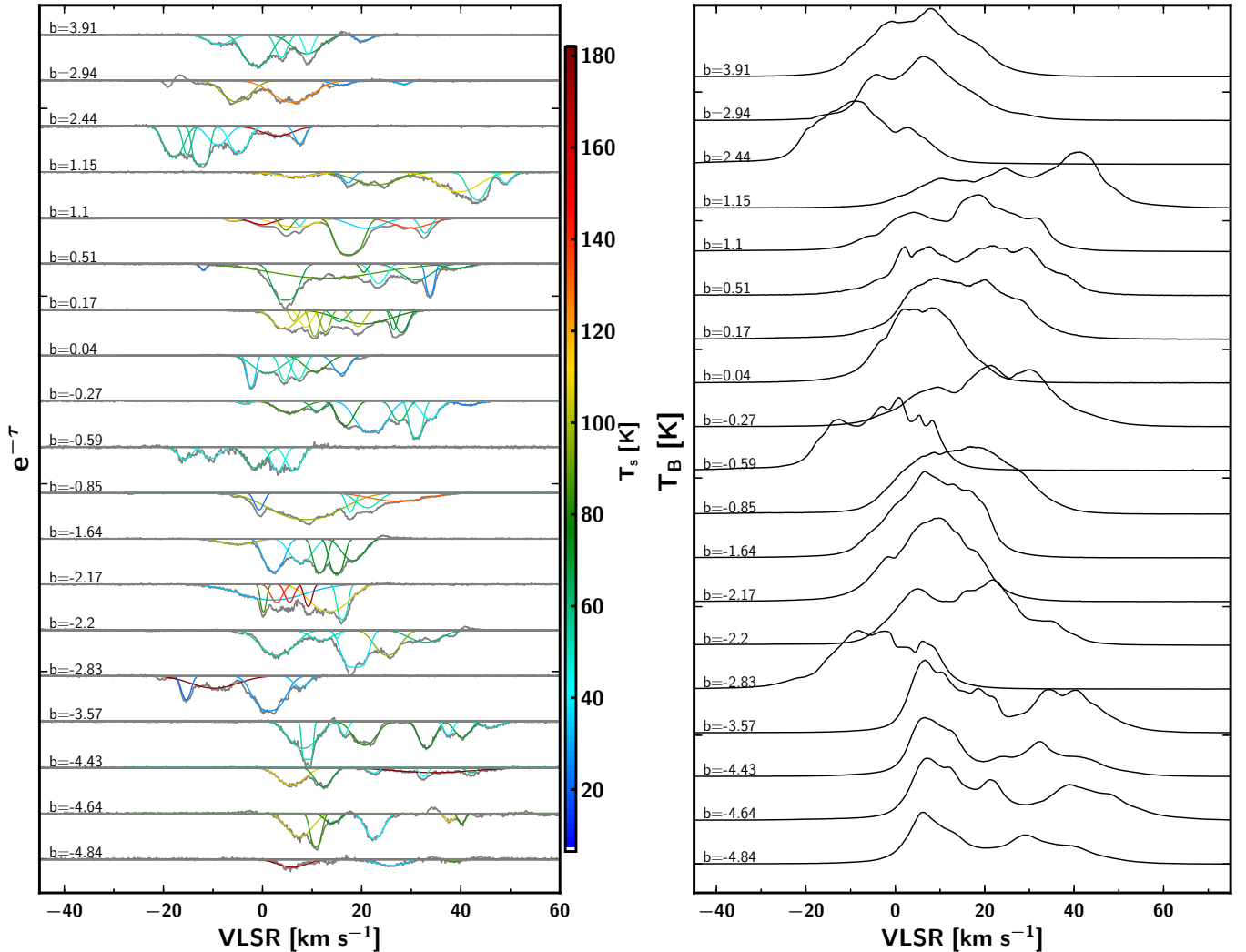


FIG. 4.— Comparisons of absorption profiles (left) and emission expected profiles (right) for 19 sightlines in near Galactic plane. The colorbar on the left panel shows the HI spin temperatures of CNM components. The sightlines are sorted in order of decreasing Galactic latitude b and are offset along the y-axis for comparison.

The cold gas is characterized by spin temperature T_s , defined from the populations of the upper and lower hyperfine levels. The spin temperature is influenced by many factors from the surrounding environment: the ambient radiation field, scattering by Lyman- α radiation, or collisions of HI atoms with electrons, protons and other H atoms. In high density CNM regions ($n \gtrsim 100 \text{ cm}^{-3}$, e.g. Shaw et al. 2017), collisions dominate the excitation of HI atoms, so that T_s is approximately equal to the kinetic temperature, T_k (e.g. Kulkarni & Heiles 1988). In contrast, in more diffuse WNM gas, collisions are insufficient to thermalise the 21 cm transition, hence T_s is generally expected to be lower than T_k (e.g. Field 1958; Deguchi & Watson 1985; Liszt 2001). However, the Lyman- α radiation field from Galactic and extragalactic sources can couple the HI spin temperature in the WNM with local gas motions. This mechanism, known as the Wouthuysen-Field effect (Wouthuysen 1952; Field 1958, 1959), requires a large number of resonance scatterings of Lyman- α photons (i.e. large optical depth) and a recoil effect of the scattering atom (i.e. momentum transfer between HI atom and Lyman- α photon). The Wouthuysen-

Field effect is likely responsible for the high WNM spin temperatures inferred from sensitive absorption studies ($\sim 10^4 \text{ K}$; Murray et al. 2014, 2017, 2018b), which cannot be explained by steady-state collisional excitation.

As expected, our Gaussian fitting shows that the FWHM of WNM components is obviously broader than that of CNM components, with a mean value of 16 km s^{-1} vs 4 km s^{-1} respectively. For the warm gas, we calculate Doppler temperature (Payne et al. 1982) from the line-width ($\Delta V = \text{FWHM}$) of each WNM component:

$$T_D = 21.86 \times \Delta V^2 \quad (13)$$

T_D is an upper limit on the kinetic temperature because the observed FWHM results from the combination of thermal and turbulent broadening. We also estimate lower limits on T_s for our WNM component, imposed by the upper limits on optical depth (see Table 3).

In Figure 8, we show the distributions of temperatures derived from the Gaussian fits to all 77 sightlines, with the top and middle panels showing CNM T_s ; and the bottom panel WNM T_D . In the top panel, we also show the T_s distributions of our three different regions; in the oth-

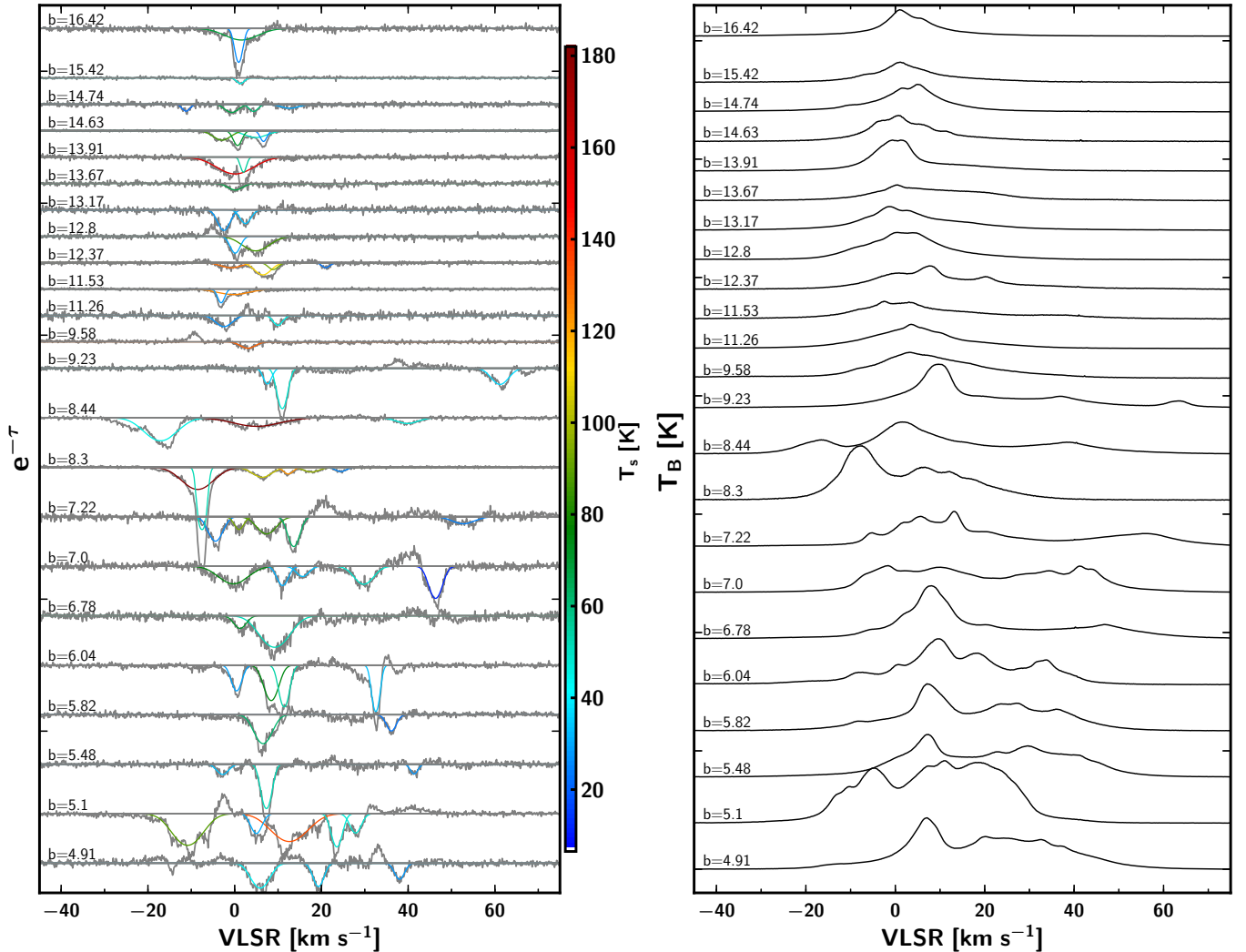


FIG. 5.— The same as Figure 4 but for 23 sightlines toward Gemini region.

ers, we plot the temperature histograms obtained from other studies (HT03, S14, M15) for comparison. Here is important to note that our optical depth sensitivity ($\sim 5 \times 10^{-3}$ per 1 km s^{-1} , obtained from the median of the 1σ noise level in optical depth spectra) is lower than that of previous studies: $\sim 2 \times 10^{-3}$ per 1 km s^{-1} for both HT03 and S14, and $\sim 9 \times 10^{-4}$ per 0.42 km s^{-1} for M15.

4.2.1. Temperatures of cold gas

For the CNM components, the spin temperatures fall in the range ~ 10 – 480 K , with our T_s distribution spreading mostly from 25 – 150 K with a peak at $\sim 50 \text{ K}$ and a median at $54.6 \pm 4.6 \text{ K}$, as well as a column-density-weighted median of $74.8 \pm 9.6 \text{ K}$ (the uncertainties of the medians are obtained from bootstrap re-sampling). Indeed, we see no obvious tail at $T_s > 200 \text{ K}$. In order to examine how T_s medians vary with the sensitivity in optical depth, we group the T_s of CNM components into four different ranges of optical depth sensitivity with similar sample sizes. From high to low sensitivities, the spin temperature medians are $61.7 \pm 16.5 \text{ K}$, $61.2 \pm 10.4 \text{ K}$, $54.3 \pm 6.6 \text{ K}$ and $48.3 \pm 8.3 \text{ K}$ respectively; and the highest T_s values belong to the highest sensitivity range. Hence, while the uncertainty is large, this (unsurprisingly) suggests

a dependence of the median measured T_s on the opacity sensitivity. This is also consistent with the fact that the highest-sensitivity survey plotted in Figure 8 (21-SPONGE; M15) measured a median T_s 25 K higher than the three others. This simply indicates that observations with improved sensitivity in HI absorption are able to directly measure the T_s of warmer HI gas (in the temperature range of UNM or WNM), resulting in a higher T_s median.

From our results, $\sim 98\%$ of CNM components (equivalent to 97% by column density of the cold gas) lie below 200 K . In fact, most of the CNM gas (80% by number of components and 74% by column density) has $T_s = 25$ – 100 K . About 14% of the gas has $100 < T_s < 200 \text{ K}$, and it contributes $\sim 22\%$ to CNM column density. The remaining of 4% of the gas is very cold with $T_s < 25 \text{ K}$ but contributes only $< 1\%$ in CNM column density. Such extremely cold gas has been observed by several studies: HT03, S14, M15, Meyer et al. (2006, 2012). In particular, Knapp & Verschuur (1972) claimed to have observed a cold HI cloud with spin temperature of 7 – 20 K ; and Wannier et al. (1999) also measured a T_s of 20 – 60 K in the Perseus B5 molecular cloud. While some fraction of very low T_s components may be spurious fits, the minimum

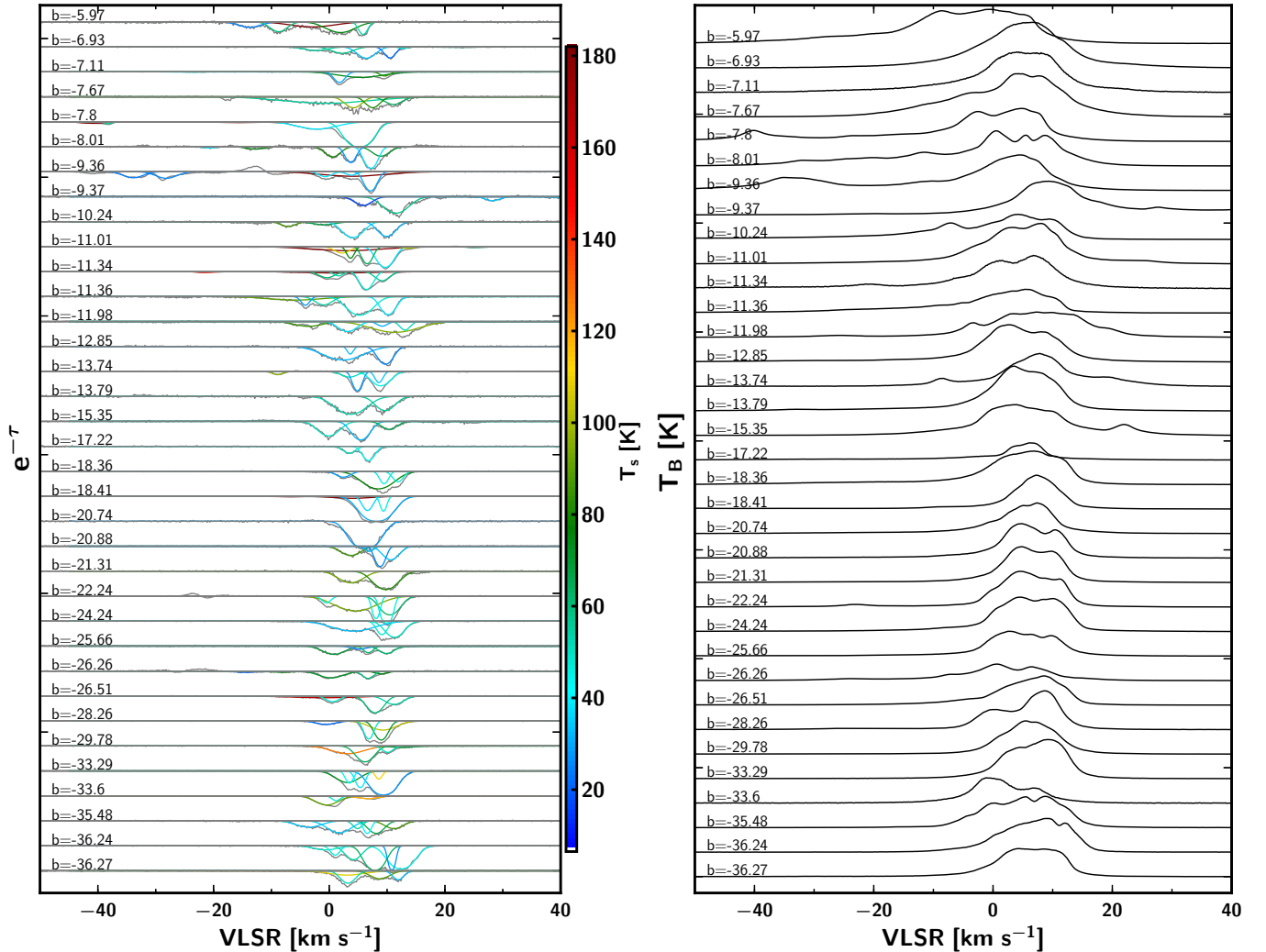


FIG. 6.— The same as Figure 4 but for 35 sightlines toward Taurus region.

CNM T_s from analytical models is ~ 20 K (Wolfire et al. 2003), and such low temperatures might also occur in regions where photoelectric heating by dust grains is reduced (e.g. Wolfire et al. 1995; Heiles & Troland 2003b).

We find no evidence for differences in the distribution of CNM spin temperatures in our three regions, despite their different characteristic environments (as shown in top panel of Figure 8). The CNM T_s distributions for the Gemini, Galactic plane and Taurus regions, have relatively close medians of 48.1 ± 8.8 K, 61.6 ± 8.7 K, 53.5 ± 4.9 K respectively, and the differences are broadly consistent with the background continuum source flux density distributions – Gemini has the highest proportion of weak sources; the Galactic plane has the lowest (as listed in Table 1). Conversely, if there were significant differences in the underlying CNM T_s distribution, then we might have observed different medians that do not scale with the background source intensity.

These T_s medians are also in good general agreement with the results from HT03 (48.8 K, along random sightlines in the Arecibo sky), S14 (49.0 K, around the Perseus molecular cloud), and Dénes et al. (2018) (48.0 K, in the Riegel-Crutcher cloud). Our values are lower than those of the 21-SPONGE survey (M15, M18 at 77.6 K, 73.6

K respectively), reflecting its higher optical depth sensitivity. More importantly, the general shape of the spin temperature histograms of the various surveys are similar, with the exception of the obvious higher- T_s tail in 21-SPONGE (see the middle panel of Figure 8). Together, this is consistent with a picture in which the spin temperature distribution of the CNM remains relatively consistent throughout the Galactic ISM; in particular, measurements along random Galactic sightlines agree well with those in fields focused around molecular clouds. Any measured differences are largely a result of higher-sensitivity observations recovering larger portions of the higher- T_s tail. This may suggest a universality of cold HI properties, which will be explored more in the following sections. The same conclusion was drawn by S14.

4.2.2. Temperatures of warm gas

For the WNM components on the bottom panel of Figure 8, we show the histogram of T_D . Most of the WNM lies below 5000 K, but the T_D distribution exhibits a long tail well beyond 20,000 K. About 45% of the WNM components (equivalent to 40% by column density) is in the thermally unstable regime with $T_D = 500$ –5000 K (see e.g. HT03, Roy et al. 2013, M15, M18), implying that

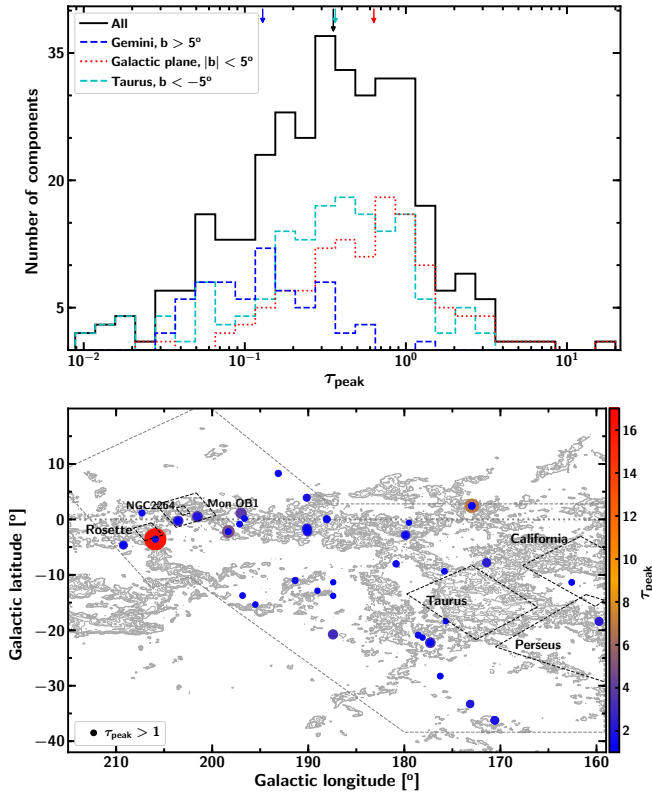


FIG. 7.— Top panel: Histograms of τ_{peak} for CNM components along 77 sightlines: black for all CNM components, blue, red and cyan for the subsamples in Gemini, Galactic plane and Taurus respectively. The arrows show the medians. Bottom panel: The locations of components having $\tau_{\text{peak}} > 1$; both the colors and sizes of the circles represent the magnitudes of τ_{peak} ; the horizontal dotted line marks the Galactic plane; the dashed rectangles roughly show the areas of molecular clouds; and the gray dashed lines roughly show the boundaries of the regions of interest.

$\sim 24\%$ of all of the atomic gas does not lie in thermal equilibrium. This fraction is consistent with previous studies: HT03 found that at least 48% of the WNM (equivalent to 30% of the total gas) is thermally unstable, and Roy et al. (2013) also found at least $\sim 28\%$ of the gas in the unstable range. The fractions in M15 and M18 are slightly lower, at $\sim 20\%$, but agree well with our finding within their uncertainties of $\gtrsim 10\%$. Nearly 14% of our WNM components have $T_D < 500$ K, corresponding to 4% in WNM column density, with the lowest limit at ~ 108 K (only two out of 349 WNM components have $T_D < 200$ K, one of which is shown in the upper panels of Figure 3). In this temperature range the WNM gas is too cold to classify as thermally unstable. From examination of the spectra, we believe these components are real, and not artifacts of poor fitting. They are not seen in absorption likely because they are thin, cold HI clouds in the diffuse medium with very low column density (as reported by Stanimirović & Heiles 2005 and Stanimirović et al. 2007). Typical 1σ upper limits on τ for these “cold” WNM components ($T_D < 500$ K) are at a median of ~ 0.07 , and thus their lower limits on T_s are at a median of 148 K. Most of the rest of the WNM (25% in component number, 37% in column density) lies between 5000 K and 20,000 K. The fraction of the gas with $T_D > 20,000$ K (not shown in the histogram) is 16% in components and 19% in column density. In reality, the gas would be

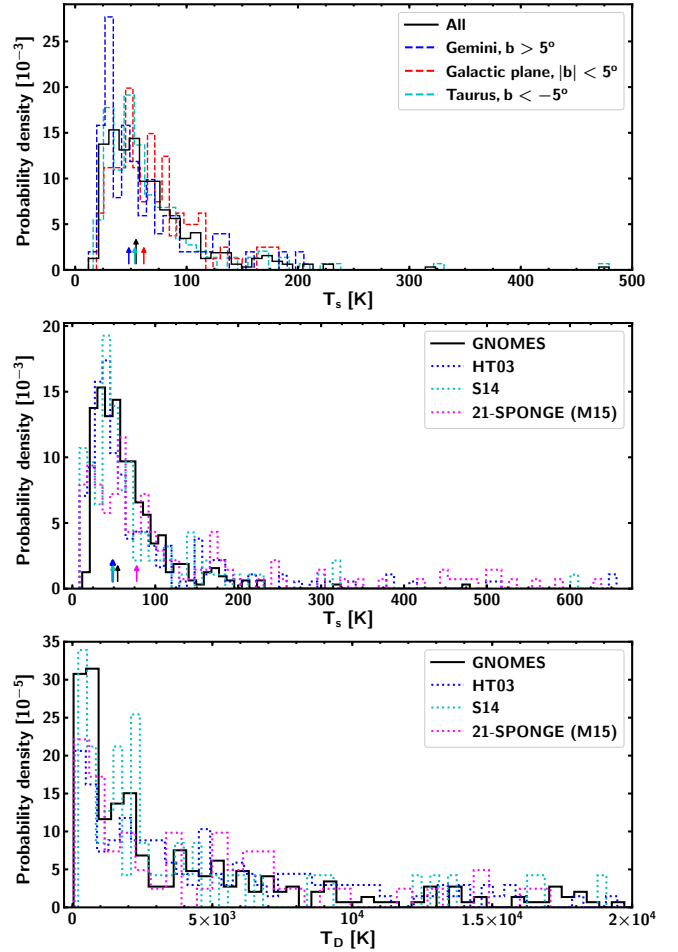


FIG. 8.— Normalized histograms of T_s for CNM components (top and middle), T_D for WNM components (bottom). In the top panel, the solid black line shows all CNM components; blue, red and cyan dashed lines show the subsamples in Gemini, the Galactic plane and Taurus respectively. In the middle and bottom panels, GNOMES is shown in solid black, HT03 in dotted blue, S14 in dotted cyan, and 21-SPONGE (M15) in dotted pink. The arrows show the medians.

ionized at temperatures above $\sim 10,000$ K, so WNM components with $T_D > 10,000$ K either must either include multiple narrower components or have highly supersonic motions (e.g. HT03).

4.3. Turbulent Mach Number Distribution

From HI observations, it is almost impossible to constrain the sonic Mach number for the WNM. However, the Mach number of non-thermal CNM motions can be estimated from the line-width ($\Delta V = \text{FWHM}$) and spin temperature. Assuming that the FWHM of each CNM component results from both thermal broadening and turbulent motions (Leung & Liszt 1976; Liszt 2001), ΔV can be expressed as:

$$\frac{(\Delta V)^2}{8 \ln 2} = \frac{k_B T_k}{m_H} + V_{\text{turb,1D}}^2 \quad (14)$$

where k_B is Boltzmann’s constant, T_k is the kinetic temperature, m_H is the mass of a hydrogen atom and $V_{\text{turb,1D}}^2$ is the one-dimensional mean square turbulent velocity which relates to the mean square three-dimensional turbulence velocity of the CNM as $V_{\text{turb,3D}}^2 = 3V_{\text{turb,1D}}^2$.

For the CNM, since thermal equilibrium is established quickly, we may assume $T_k = T_s$, then the isothermal sound speed can be computed as $C_s = \sqrt{kT_s/\mu m_H}$. Dividing ΔV and $V_{\text{turb},3\text{D}}$ by the sound speed C_s will respectively give the sonic Mach number (M_s) and the turbulent Mach number (M_t) of the CNM. Adopting a mean atomic weight of $\mu = 1.4$ for the Galactic ISM, we may write:

$$M_t = \frac{V_{\text{turb},3\text{D}}}{C_s} = \sqrt{3 \left(\frac{M_s^2}{8 \ln 2} - \mu \right)}. \quad (15)$$

We show a histogram of derived M_t values in Figure 9. The median sonic Mach number for the whole sample of 77 sources is $M_t = 4.1 \pm 0.3$, and the histogram peaks around $M_t = 3.5$ – 4.0 . This result is slightly higher than found by HT03, M15 and M18 (at $M_t = 3.4$, 2.9 and 3.1 respectively) and agrees best with S14 in the Perseus molecular cloud region ($M_t = 4.0$). We also note that Burkhart et al. (2010) find $M_t \sim 4.0$, for CNM around the SMC bar even though the gas properties in the SMC are very different from those in the Milky Way. All of these results support a picture in which internal macroscopic motions in the CNM are highly supersonic. One possible explanation for this dynamical property of the CNM is that the cold HI gas along the line of sight consists of a few individual long living CNM structures (clumps); while the individual clumps are subsonic, their relative velocities are supersonic with respect to the CNM sound speed as they were inherited from the velocity dispersion of the WNM (from which CNM was formed). This would imply that the observed Mach number along Galactic sightlines is due to the velocity dispersion from the relative motions of clumps rather than the internal velocity dispersion of the cold HI medium (e.g. Koyama & Inutsuka 2002; Heitsch et al. 2005; Hennebelle & Audit 2007; Hennebelle et al. 2007; Saury et al. 2014). Alternatively, it has been suggested that the supersonic motions of the cold HI along the edges of the SMC bar may be related to the shearing/turbulent flows and/or shocks between the bar and the surrounding gas (Burkhart et al. 2010); it is possible that similar processes may also be implicated in some Milky Way gas.

4.4. HI column density distributions

The HI column density of the cold absorbing HI along each sightline is calculated by:

$$N_{\text{HI,CNM}} = C_0 \int T_s \tau_v dv \quad (16)$$

where $C_0 = 1.823 \times 10^{18} \text{ cm}^{-2} \text{ K}^{-1} (\text{km s}^{-1})^{-1}$, and for the non-absorbing emission components, we estimate the column density as

$$N_{\text{HI,WNM}} = C_0 \int T_B dv \quad (17)$$

where T_B is the brightness temperature.

We summarize the column densities from the Gaussian fits in Figure 10. In the top panel we plot histograms of N_{HI} for all CNM and WNM Gaussian components. The two phases have similar column density distributions regardless of Galactic latitudes. They have rela-

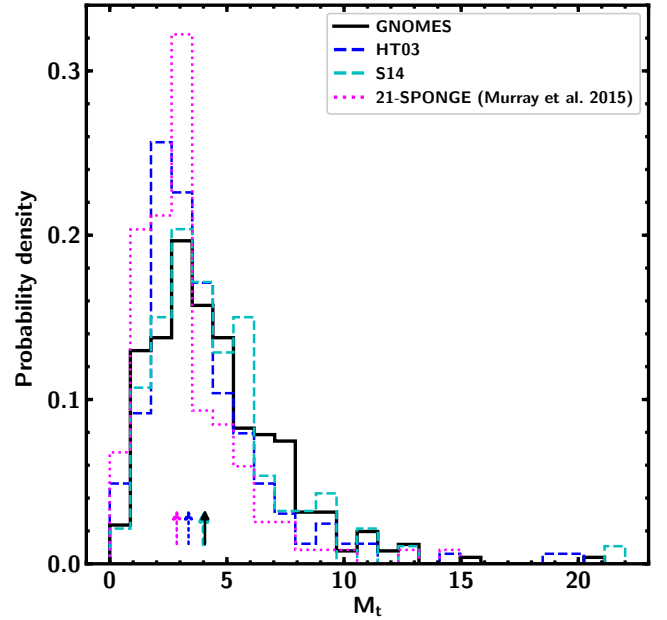


FIG. 9.— Normalized histograms of turbulent Mach numbers for all CNM Gaussian components: GNOMES in black, HT03 in blue, S14 in green and M15 in pink.

tively close medians ($1.4 \times 10^{20} \text{ cm}^{-2}$ for CNM and $2.3 \times 10^{20} \text{ cm}^{-2}$ for WNM) even though the column density ranges are enormous ($(0.04\text{--}32.0) \times 10^{20} \text{ cm}^{-2}$ for CNM and $(0.06\text{--}48.6) \times 10^{20} \text{ cm}^{-2}$ for WNM). In the three remaining panels of Figure 10, we show histograms of $\sum N_{\text{HI,CNM}}$, $\sum N_{\text{HI,WNM}}$ and total N_{HI} along sightlines (color-coded by region). Table 2 lists the means and medians of the distributions (also indicated by arrows in the histograms). Now, when summing column densities of all CNM and WNM components along each line of sight, it is obvious that the column densities distributions in the three regions are well separated, except for the case of $\sum N_{\text{HI,WNM}}$ in Gemini and Taurus. Gemini occupies the low N_{HI} regimes, the Galactic plane samples the highest N_{HI} with the sightlines toward the Perseus and Outer arms, and so Taurus is in the intermediate range. Our total CNM column density is about two thirds of the total WNM column density ($956.1 \times 10^{20} \text{ cm}^{-2}$ versus $1609.7 \times 10^{20} \text{ cm}^{-2}$). The median of total N_{HI} in Taurus is nearly double that of Gemini ($23.8 \times 10^{20} \text{ cm}^{-2}$ against $11.5 \times 10^{20} \text{ cm}^{-2}$), but only about one third of the N_{HI} median in Galactic plane ($79.0 \times 10^{20} \text{ cm}^{-2}$). While the N_{HI} distribution in Galactic plane is widely spread, the histograms of other regions are concentrated in well-defined ranges. Most Galactic plane sightlines ($|b| < 5^\circ$) with high column densities ($N_{\text{HI}} > 50 \times 10^{20} \text{ cm}^{-2}$) are close to NGC 2264 and Rosette molecular clouds where the CO contours peak; on the contrary, all other diffuse sightlines above the plane are found further away from the two molecular clouds ($b > 5^\circ$), and apparently do not have significant CO detections. In most cases, the CNM contributes significantly to the total HI column density.

In Figure 11, we compare our results with the findings of previous surveys (here HT03, S14 and M15) that applied the same basic methodology in observation and data analysis, but for different regions of the sky. In all cases, our N_{HI} distributions are slightly shifted to-

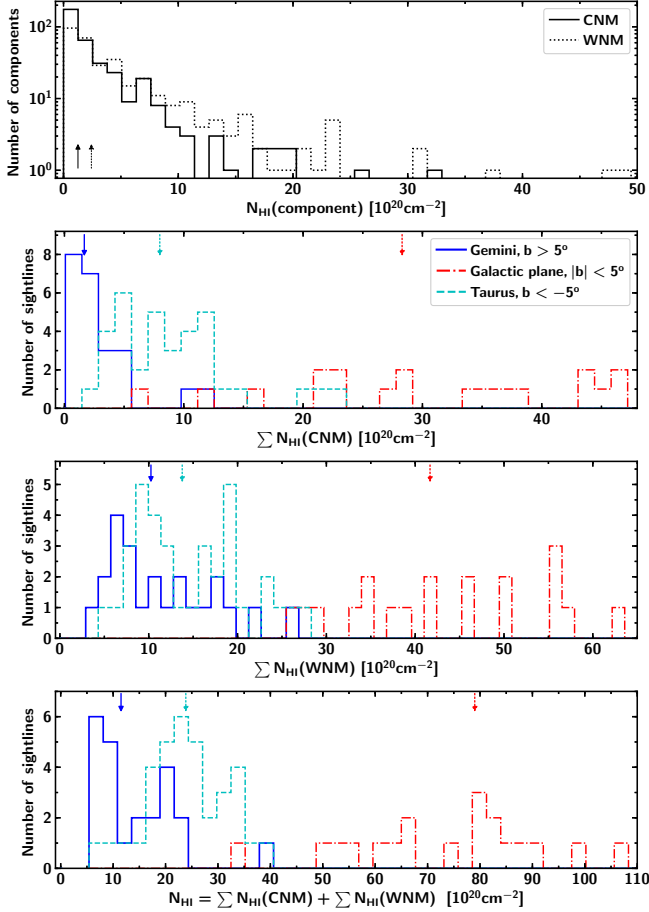


FIG. 10.— Histograms of N_{HI} for all CNM (solid) and WNM (dotted) Gaussian components (top), $\sum N_{\text{HI,CNM}}$ (second panel), $\sum N_{\text{HI,WNM}}$ (third panel), and total $N_{\text{HI}} = \sum N_{\text{HI,CNM}} + \sum N_{\text{HI,WNM}}$ (bottom) for all sightlines in different regions: blue for Gemini, red for Galactic plane, cyan for Taurus. The arrows show the medians.

TABLE 2
MEANS AND MEDIANS OF HISTOGRAMS IN FIGURE 10

| Region | Mean N_{HI} [10^{20} cm^{-2}] | Median N_{HI} [10^{20} cm^{-2}] |
|---|---|---|
| CNM, Gemini ($b > 5^\circ$) | 2.7 | 1.7 |
| CNM, Galactic plane ($ b < 5^\circ$) | 30.3 | 28.3 |
| CNM, Taurus ($b < -5^\circ$) | 9.1 | 8.0 |
| WNM, Gemini | 11.6 | 10.3 |
| WNM, Galactic plane | 43.4 | 41.7 |
| WNM, Taurus | 14.8 | 13.8 |
| CNM+WNM, Gemini | 14.3 | 11.5 |
| CNM+WNM, Galactic plane | 73.7 | 79.0 |
| CNM+WNM, Taurus | 23.9 | 23.8 |

ward higher column densities. Our lowest N_{HI} median is found in the Gemini region, which is comparable with the median from S14 for Perseus molecular cloud ($10.3 \times 10^{20} \text{ cm}^{-2}$) and M15 ($10.4 \times 10^{20} \text{ cm}^{-2}$), but still higher than that obtained by HT03 ($5.5 \times 10^{20} \text{ cm}^{-2}$). These differences likely reflect genuine differences in the sightlines probed by the different studies. The present work contains a high proportion of positions either in the

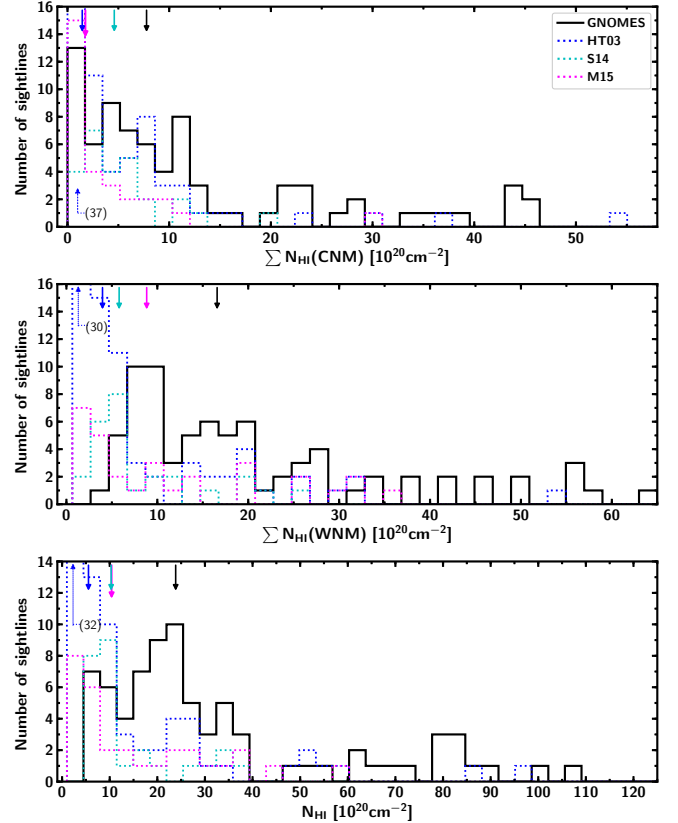


FIG. 11.— Histograms of $\sum N_{\text{HI,CNM}}$ (top), $\sum N_{\text{HI,WNM}}$ (middle) and total $N_{\text{HI}} = \sum N_{\text{HI,CNM}} + \sum N_{\text{HI,WNM}}$ (bottom) for each sightline estimated from Gaussian decomposition fit: black for Gnomes, blue for HT03, cyan for S14 and pink for M15. The solid downward arrows show the medians. The upward arrows indicate the maximum values beyond the tops of the figure (HT03 only).

Galactic Plane or close to molecular regions; meanwhile, HT03 and M15 mostly observed random sightlines in the neighborhood of the Solar system, and the S14 sightlines around Perseus mostly sampled material away from the main body of the molecular cloud.

4.5. N_{HI}^* vs N_{HI}

The optically thin HI column density, N_{HI}^* , is directly estimated from the expected emission profile, so is proportional to the profile area. On the contrary, to calculate the opacity-corrected N_{HI} one needs both spin temperature and optical depth, which can be derived from the combination of on-/off-source spectra. Based on our results, we can compare the two estimates. The ratio $f = N_{\text{HI}}/N_{\text{HI}}^*$ for all 77 sightlines is plotted as a function of total N_{HI} in Figure 12. For the full sample, f has a mean and median of 1.28 and 1.21 respectively. At low column densities below $\sim 1 \times 10^{21} \text{ cm}^{-2}$, N_{HI}^* is comparable to the corrected N_{HI} ($f \sim 1.0$); the ratio then rises as column density increases, reaching $f \sim 1.8$ by the time N_{HI} has increased by an order of magnitude ($1 \times 10^{22} \text{ cm}^{-2}$). Interestingly, the ratio $N_{\text{HI}}/N_{\text{HI}}^*$ for the Gemini region is almost flat and consistent with unity over the whole of its N_{HI} range $(5\text{--}40) \times 10^{20} \text{ cm}^{-2}$, and as seen in the lower panel, no sightlines in this region fall within CO contours. Meanwhile, the ratio f around Taurus stays mostly around the mean value of 1.3, whereas within the

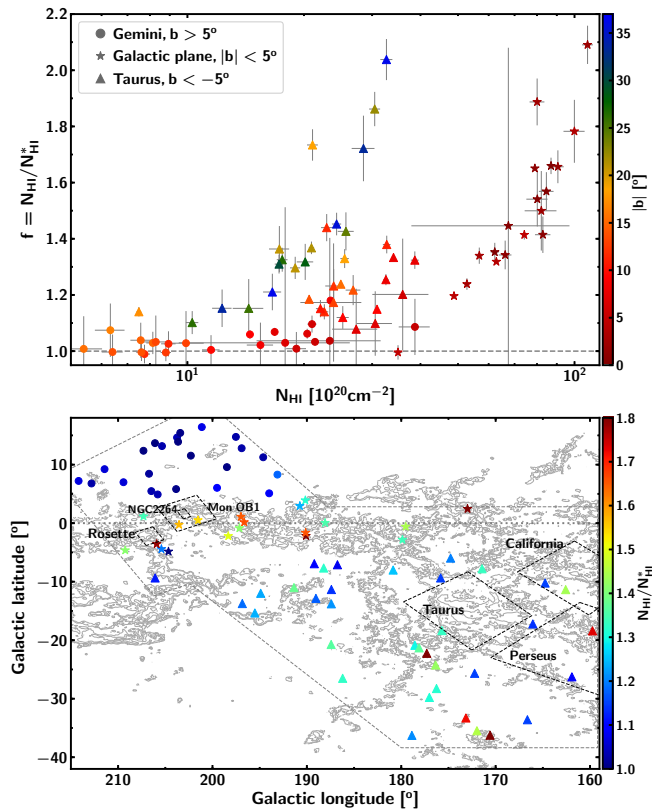


FIG. 12.— Top panel: $f = N_{\text{HI}}/N_{\text{HI}}^*$ as a function of N_{HI} in Gemini (dots), Galactic plane (stars) and Taurus (triangles) regions. The colors represent the absolute values of Galactic latitude $|b|$; the dashed line marks where $N_{\text{HI}}^* = N_{\text{HI}}$. Bottom panel: The map of $f = N_{\text{HI}}/N_{\text{HI}}^*$ for our 77 sightlines toward the three regions; the horizontal dotted line shows the Galactic plane; the dashed rectangles roughly show the areas of molecular clouds; and the gray dashed lines roughly show the boundaries of the regions of interest. The colors represent the values of the ratio f .

Galactic plane it exhibits a rising trend with N_{HI} . This indicates that significant corrections are needed to account for opacity effects, especially in denser gas regimes or at low latitudes (see also Dickey et al. 2003; Bihl et al. 2015).

Nevertheless, the question of how best to correct for HI opacity effects when emission/absorption pairs are not available is still open (see the discussion in Section 5). A few methods have been proposed: e.g. a linear correlation between f and $\log_{10}(N_{\text{HI}}^*)$ (Dickey et al. 2000; Lee et al. 2015) or a simple isothermal correction assuming the same T_s along the lines-of-sight (as employed by Liszt 2014b; Remy et al. 2017). The general increase of the correction factor f as a function of N_{HI} is obvious, but the relationship between the two appears to be environmentally dependent, as just discussed above for our regions. Literature values of f include ~ 1.1 in the range $N_{\text{HI}} = (3.9\text{--}13.0) \times 10^{20} \text{ cm}^{-2}$ for 26 sightlines within and around the Perseus molecular cloud (Lee et al. 2015); $f \sim (1.1\text{--}1.3)$ for 79 random sightlines in Millennium survey (HT03); and $f < 1.2$ for reddenings of $E(B - V) \lesssim 0.5$ mag, for sightlines at high Galactic latitudes (Liszt 2014a).

4.6. The CNM fraction, F_{CNM}

In the first panel of Figure 13, we present the variation of the CNM fraction ($F_{\text{CNM}} = N_{\text{CNM}}/N_{\text{HI}}$) as a function of N_{HI} . While the F_{CNM} does increase with N_{HI} , there is clearly a very large scatter. We measure median values of $F_{\text{CNM}} = 0.43$ and 0.37 respectively for the Galactic plane and Taurus regions – more than double the value of 0.16 for Gemini. We find 9/77 sightlines with $F_{\text{CNM}} < 0.1$, all of them in Gemini, above the Galactic Plane. The highest F_{CNM} values are found in the proximity of the giant molecular clouds (Rosette, NGC 2264 and in the south of Taurus and California) as shown in the map in the lower panel of the Figure. The Taurus F_{CNM} median is comparable to the value of 0.35 found in Perseus (S14) – a similar region in and around a molecular cloud. Similarly, the median for the Gemini region is consistent with the value of 0.20 found by M15 and 0.23 by HT03, both of which sampled largely diffuse sightlines. Thus, the CNM fraction around molecular clouds seems to be higher than in diffuse regions. This agrees well with a scenario in which a high CNM fraction is required for molecule formation, and GMCs are built-up stage by stage – from WNM-rich gas to CNM-rich gas to molecular clouds.

Overall the F_{CNM} from all GNOMES sightlines does not exceed 75% – a result that agrees with the F_{CNM} range observed in different regions of the Galaxy by HT03 and S14, also using the Arecibo telescope, and M15 and M18, using the VLA for absorption. Our CNM fraction is also close to the range of $F_{\text{CNM}} \sim 40\text{--}70\%$ found in the numerical simulations of Kim et al. (2014).

In Figure 14, we plot F_{CNM} against the $N_{\text{HI}}/N_{\text{HI}}^*$ ratio. Obviously, $N_{\text{HI}}/N_{\text{HI}}^*$ increases with the increase of F_{CNM} as expected. This simply demonstrates that the higher the CNM fraction is along the line-of-sight, the more important the opacity correction is. Nevertheless, we note that with the CNM fraction below 20%, N_{HI}^* is consistent with N_{HI} , to within the errors. After this point, the $N_{\text{HI}}/N_{\text{HI}}^*$ ratio rises up to a value of ~ 2 as F_{CNM} increases from 20% to 75%.

5. HI OPACITY CORRECTIONS

Pursuing the ultimate goal of deriving “true” N_{HI} maps toward our three regions around Taurus and Gemini, we will test two methods of opacity correction using HI emission data from the GALFA-HI survey. This is an important preparatory step for future work aiming to derive dark gas maps in these two regions using dust and γ -ray data as tracers of total proton column density.

5.1. From the best fit of $f = N_{\text{HI}}/N_{\text{HI}}^*$ vs $\log_{10}(N_{\text{HI}}^*)$

The first method estimates an appropriate correction factor for each sightline from the best fit of $f = N_{\text{HI}}/N_{\text{HI}}^*$ vs $\log_{10}(N_{\text{HI}}^*/10^{20})$, using the data from all 77 sightlines (e.g. Lee et al. 2015). From our data, the ratio f increases with increasing N_{HI}^* , with a Pearson linear coefficient of 0.5. To find an appropriate correlation, we fit the datapoints using four models: linear, quadratic, first-order exponential (in the form of $e^{ax} + b$) and second-order exponential ($e^{ax^2} + b$). We then compute the “Bayesian factors” (R) and “Bayesian p -values” (p) from the Bayesian model selection for each pair of models, finding $R(\text{linear}/\text{quadratic}) = 72.08$, $p(\text{linear}) =$

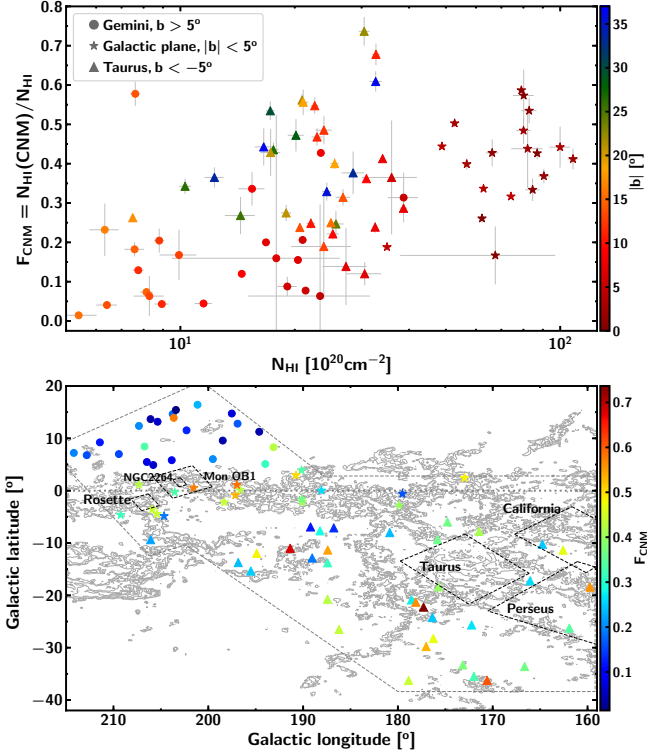


FIG. 13.— Top panel: $F_{\text{CNM}} = N_{\text{CNM}}/N_{\text{HI}}$ as a function of total N_{HI} toward Gemini (dots), Galactic plane (stars) and Taurus (triangles) regions. The colors represent the absolute values of Galactic latitude $|b|$. Bottom panel: The map of F_{CNM} for all 77 sightlines toward the three regions; the horizontal dotted line shows the Galactic plane; the dashed rectangles roughly show the areas of molecular clouds; and the gray dashed lines roughly show the boundaries of the regions of interest. The colors represent the values of F_{CNM} .

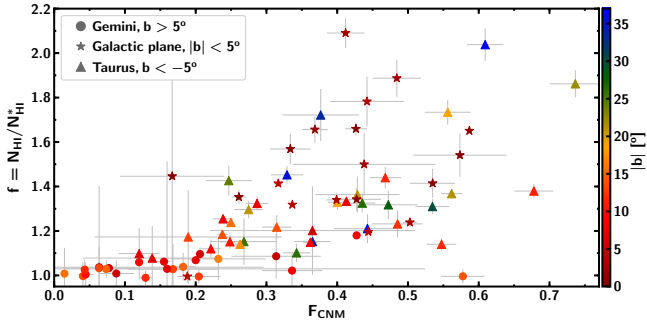


FIG. 14.— $f = N_{\text{HI}}/N_{\text{HI}}^*$ versus F_{CNM} along 77 sightlines. The colors represent the absolute values of Galactic latitude $|b|$.

98.6%; $R(\text{linear/first-order exponential}) = 1.22$, $p(\text{linear}) = 54.9\%$; $R(\text{linear/second-order exponential}) = 1.02$, $p(\text{linear}) = 50.5\%$. Thus the Bayesian factors favor the linear model (since their R values are greater than 1 and their p -values are greater than 50%). It is worth noting that the linear model is definitely much more preferred than the quadratic, but the posterior probability in favor of the first-order exponential model is 46% (compared to the linear model), which is too large to support rejecting the exponential model; meanwhile the posterior probabilities in favor of the second-order exponential and linear models are almost the same. Figure 15 shows the general linear fit of $f = N_{\text{HI}}/N_{\text{HI}}^*$ vs $\log_{10}(N_{\text{HI}}^*/10^{20})$ with

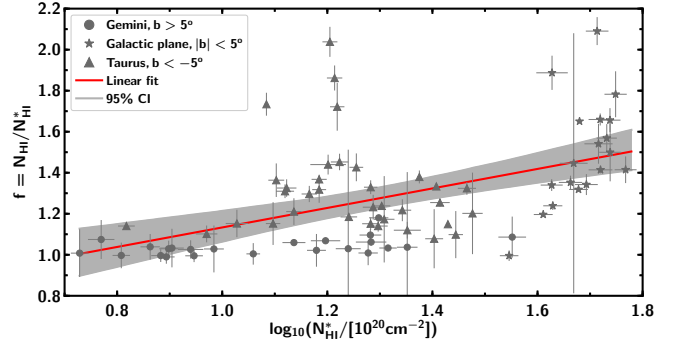


FIG. 15.— Ratio $f = N_{\text{HI}}/N_{\text{HI}}^*$ versus $\log_{10}(N_{\text{HI}}^*/10^{20})$. The red line represents the best linear fit: $f = (0.47 \pm 0.09)\log_{10}(N_{\text{HI}}^*/10^{20}) + (0.66 \pm 0.12)$. The shaded region shows the 95% confidence interval (CI) obtained from bootstrap re-sampling.

95% confidence intervals obtained from bootstrap re-sampling. The correction factor from the best fit is: $f = (0.47 \pm 0.09)\log_{10}(N_{\text{HI}}^*/10^{20}) + (0.66 \pm 0.12)$ (see also Lee et al. 2015, for the gas around Perseus molecular cloud). The HI column density obtained from this method is denoted as $N(\text{HI})_{\text{fit}}$. We note that our slope is quite different from Lee et al. (2015)'s. However, as mentioned before, it is clear that the correction factor and its variation with N_{HI} for each region are quite distinct, hence applying a single linear relationship for all regions may not be reliable. In fact, when fitting on a region-by-region basis we find that the best fit for the Gemini region is nearly flat with $f = (0.09 \pm 0.04)\log_{10}(N_{\text{HI}}^*/10^{20}) + (0.94 \pm 0.04)$; for sightlines through the Galactic plane area the correction factor increases rapidly as N_{HI}^* increases: $f = (2.41 \pm 0.93)\log_{10}(N_{\text{HI}}^*/10^{20}) - (2.57 \pm 1.57)$; but the best fit f for Taurus region decreases with increasing N_{HI}^* : $f = (-0.18 \pm 0.26)\log_{10}(N_{\text{HI}}^*/10^{20}) + (1.54 \pm 0.32)$. A linear correlation between f and $\log_{10}(N_{\text{HI}}^*)$ is therefore not convincing for every region.

5.2. Using region-dependent uniform T_s

The second approach is to apply a simple isothermal correction to GALFA-HI using a single value of spin temperature for each sub-region. Here, an opacity-corrected HI column density is obtained by integrating the following function of brightness temperature (T_B), and spin temperature T_s (e.g. Lockman & Savage 1995; Wakker et al. 2011):

$$N_{\text{HI}}^{\text{ISO}} = 1.823 \times 10^{18} \int T_s \ln \left[\frac{T_s}{T_s - T_{\text{exp}}} \right] dv. \quad (18)$$

This approximation has the advantage that with an appropriate value of T_s , it only requires HI emission spectra to estimate N_{HI} , but it is not applicable at high optical depths where $T_s \approx T_B$ because the denominator in Equation 18 approaches zero. By conducting a least square fit of the HI column densities obtained from this isothermal assumption and those from the Gaussian decomposition method (Section 4.4) using T_s as a parameter, we find best fit spin temperatures of $T_s = 217.7$ K for the Gemini region ($b > 5^\circ$), $T_s = 138.8$ K for the Galactic Plane ($|b| < 5^\circ$), and $T_s = 117.9$ K for the Taurus region ($b < -5^\circ$). The HI column density corrected by this method is denoted as $N(\text{HI})_{\text{uniform}}$, and its correspond-

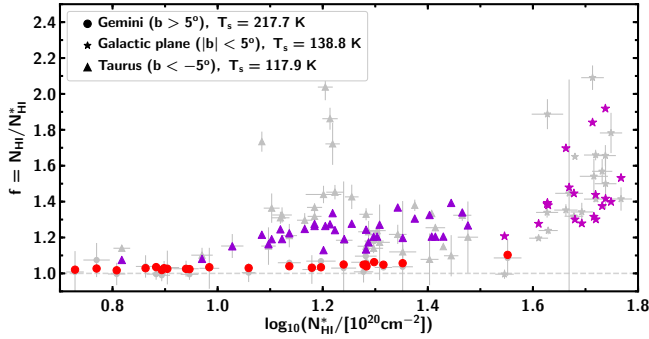


FIG. 16.— Ratio $f = N_{\text{HI}}/N_{\text{HI}}^*$ versus $\log_{10}(N_{\text{HI}}^*/10^{20})$. The gray data points are results from Gaussian fit (same as for Figures 12 and 15). The color markers show the ratios estimated from corrected N_{HI} using single values of T_s for different regions: stars for Galactic plane $|b| < 5^\circ$, triangles for Taurus region $b < -5^\circ$, and dots for Gemini area $b > 5^\circ$.

ing f ratios are shown in Figure 16. It can be seen that the isothermal approximation with uniform spin temperatures generally reproduces quite well the correction factors derived from the original Gaussian decomposition.

5.3. Comparing corrected N_{HI} maps

We apply the two methods described above to correct for opacity effects pixel-by-pixel in the GALFA-HI maps of the Gemini, Galactic plane and Taurus regions. In upper panel of Figure 17 we compare the corrected N_{HI} results from the *general* linear fit and uniform T_s maps by plotting the histograms of their relative differences in different regions, and Figure 18 projects these relative differences onto the corresponding maps. Although we see individual pixel-by-pixel differences of up to $\sim 25\%$, the N_{HI} corrected from the two methods are in general comparable with a median difference of 0.6%, a mean of 0.1%, and standard deviation of 7.9%. The difference between the two corrected column densities is largest in the Gemini region ($b > 5^\circ$) with (median, mean, standard deviation) of (6.1%, 6.5%, 10.0%). In the Taurus region, the two correction methods agree well, with (median, mean, standard deviation) of (1.4%, 1.1%, 5.0%). Within the Galactic plane, N_{HI} corrected with uniform T_s is slightly lower than from the linear fit, the values of (median, mean, standard deviation) are (0.2%, 1.2%, 11.5%). Generally, the largest differences (more than 10%) are found in regions assumed to have higher CNM fractions: near the Galactic plane and in close vicinity to GMCs (see Figure 13 and 18).

These differences may arise in part from the fact that the *general* linear fit is made to the whole map for all three areas, whereas the different uniform spin temperatures were applied to each region. It appears that the two types of opacity correction are not consistent in Gemini and Galactic plane, but agree much better for the Taurus region, probably because our *general* linear fit seems to reproduce well the correction factors for the Taurus area only (as seen in Figure 15). By contrast, when region-by-region linear fitting is applied, the two opacity correction methods agree very well for the Gemini region only, and depart further in the others, as seen in the lower panel of Figure 17. This means that a regional linear correlation could be a good choice for Gemini, but is not suitable for our sightline samples toward the Galactic plane and Taurus regions. In addition, our region of interest spreads

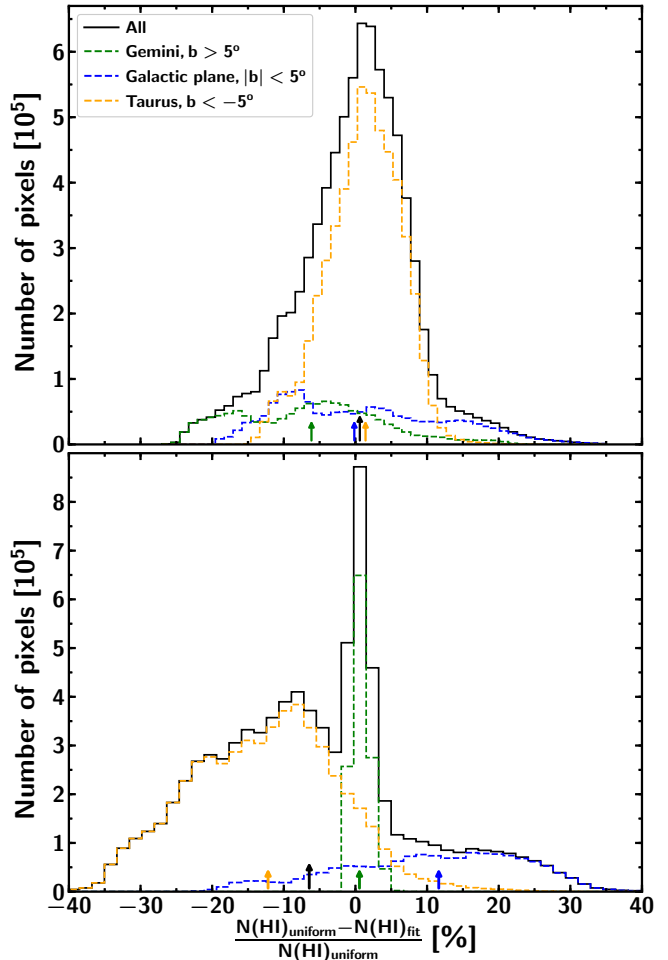


FIG. 17.— Comparisons of HI column densities obtained from two methods of opacity correction for GALFA-HI data toward the regions around Taurus and Gemini: (1) from the best fit of $f=N_{\text{HI}}/N_{\text{HI}}^*$ vs $\log_{10}(N_{\text{HI}}^*)$ (subscript “fit”) and (2) from uniform spin temperature maps (subscript “uniform”). Upper panel for the *general* best linear fit, lower panel for three region-dependent linear fits. The blue histogram shows the N_{HI} relative difference for Galactic plane area ($|b| < 5^\circ$), the green histogram for Gemini ($b > 5^\circ$), the yellow one for Taurus region ($b < -5^\circ$) and black line for all three areas. The arrows show the medians.

over a large sky area of different conditions, therefore, we prefer a region-based uniform spin temperature correction for HI opacity throughout the Galactic ISM.

6. SUMMARY AND FUTURE WORK

As a follow-up of the HI study in the Perseus molecular cloud (Stanimirović et al. 2014; Lee et al. 2015), we have presented a large-scale Arecibo survey of HI emission/absorption observations to investigate the physical properties of cold and warm gas in the vicinity of five GMCs (Taurus, California, Rosette, Mon OB1, NGC 2264). This study is also a part of the GNOMES (Galactic Neutral Opacity and Molecular Excitation Survey) collaboration, which aims to explore the properties of neutral and molecular gas in/around molecular clouds. We detected strong HI absorption in all directions toward 79 background radio continuum sources. By performing Gaussian decompositions (following the method of Heiles & Troland 2003a) for all pairs of absorption/emission spectra, we directly determined HI optical depths, tem-

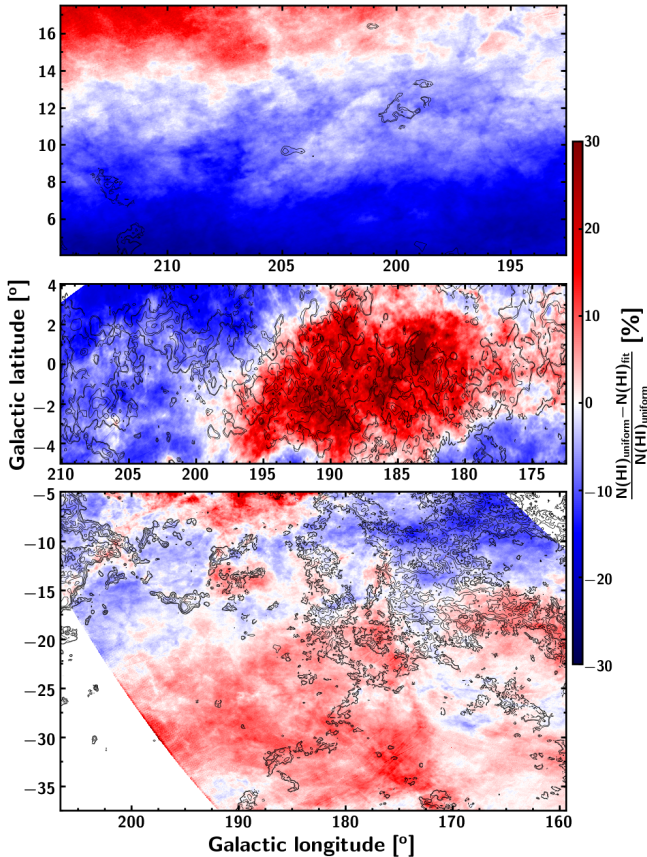


FIG. 18.— Relative difference of opacity-corrected GALFA-HI column densities obtained from the two methods discussed in the text (linear fit and region-dependent uniform spin temperature). The top panel shows the Gemini region ($b > 5^\circ$), the middle panel for the Galactic plane region ($|b| < 5^\circ$), and the bottom panel shows the Taurus region ($b < -5^\circ$). The colors indicate the relative difference $[N(\text{HI})_{\text{uniform}} - N(\text{HI})_{\text{fit}}]/N(\text{HI})_{\text{uniform}}$ (%). The contours are from $W_{\text{CO}(1-0)}$ map as described in Figure 1.

peratures and column densities for 349 CNM and 327 WNM Gaussian components. We used the distribution of CO integrated intensity $W_{\text{CO}(1-0)}$ (Dame et al. 2001) to separate our sample into three different interstellar environments – diffuse ($b > 5^\circ$), in-Plane ($|b| < 5^\circ$), and around giant molecular clouds ($b < -5^\circ$). Comparing the HI column density N_{HI} with that derived under the optically-thin assumption (N_{HI}^*) allows us to test two different methods for opacity-correction, which we apply to the GALFA-HI data. Our key conclusions are as follows:

1. The peak optical depth of individual Gaussian components ranges from ~ 0.01 – 16.2 , with a median value of 0.35. We measure CNM spin temperatures between ~ 10 – 480 K, finding that the distribution peaks at ~ 50 K. The typical sonic Mach number for CNM is ~ 4 , which is consistent with previous studies and suggests that the turbulent motion of cold gas in the ISM is strongly supersonic. The median values of column densities for individual CNM and WNM components are $1.4 \times 10^{20} \text{ cm}^{-2}$ and $2.3 \times 10^{20} \text{ cm}^{-2}$, respectively.

2. The properties of individual CNM components in our survey toward the three characteristic physical regions are consistent. More interestingly, they also agree well with those of previous observations along all-sky sightlines (HT03, M15, M18) and in/around the intermediate-mass Perseus molecular cloud (S14). This

suggests that the properties of cold HI gas in the Galactic ISM are fairly universal. The same conclusion was pointed out by S14.

3. The WNM constitutes $\sim 60\%$ of the total HI gas, about 40% of which is in thermally unstable regime with an upper limit on kinetic temperature of 500–5000 K. The implied fractions of cold, unstable and warm medium (by mass) are therefore 40%, 24% and 36%, respectively.

4. The fraction of cold gas along each sightline, F_{CNM} , increases with increasing N_{HI} to a maximum of 75%. This is consistent with previous observations (HT03, M15, M18, S14) and also close to the 40–70% F_{CNM} range found in the numerical simulations of Kim et al. (2014). The F_{CNM} around molecular clouds is higher than in diffuse regions. This may support a staged build-up scenario for GMCs: from WNM-rich gas to CNM-rich gas to molecular clouds, with a high fraction of cold gas required for molecules to form.

5. The HI opacity correction factor $f = N_{\text{HI}}/N_{\text{HI}}^*$ increases as total N_{HI} increases, with a median value of 1.21 for the full sample of 77 sightlines. However, the variation behaves differently in each individual region: while the ratio f for Gemini is almost flat, it scatters around a mean value of 1.3 in Taurus and rises very steeply within the Galactic plane. Therefore, a linear relationship between the correction factor f and $\log_{10}(N_{\text{HI}}^*)$ is not convincing for every region.

6. We tested two methods of opacity correction: A linear fit of $f = N_{\text{HI}}/N_{\text{HI}}^*$ vs $\log_{10}(N_{\text{HI}}^*)$ made to the full sample, and the use of region-dependent uniform spin temperatures. We applied both methods to GALFA-HI emission cubes, finding that the relative difference on a pixel-by-pixel basis is up to $\sim 25\%$, however the mean offset between the derived N_{HI} distributions is small ($\sim 1\%$). Because separate linear fits do not well describe the relation between f and N_{HI}^* for each region, we prefer the uniform T_s method.

Future work will analyse OH observations toward the same continuum source sample (A. Petzler in prep.), then combine these with CO data, and broad-band tracers of molecular hydrogen and total proton column density to begin constructing dark gas maps of the Taurus and Gemini regions.

ACKNOWLEDGMENTS

JRD is the recipient of an Australian Research Council (ARC) DECRA Fellowship (project number DE170101086). MYL was partially funded through the sub-project A6 of the Collaborative Research Council 956, funded by the Deutsche Forschungsgemeinschaft (DFG). CEM is supported by a National Science Foundation Astronomy and Astrophysics Postdoctoral Fellowship under award AST-1801471.

We are very grateful to Professor Isabelle Grenier and Professor Mark Wardle for a number of useful discussions. We are indebted to T. Dame for generously providing the CO survey data. We thank the anonymous referee for constructive comments and criticisms which allowed us to improve this work. This publication utilizes data from Galactic ALFA HI (GALFA HI) survey data set obtained with the Arecibo L-band Feed Array (ALFA) on the Arecibo 305m telescope. The Arecibo Observatory is operated by SRI International under a co-

operative agreement with the National Science Foundation (AST-1100968), and in alliance with Ana G. Méndez – Universidad Metropolitana, and the Universities Space Research Association. The GALFA HI surveys have been funded by the NSF through grants to Columbia University, the University of Wisconsin, and the University of California.

APPENDIX A: COMPARISON OF GAUSSIAN AND PSEUDO-VOIGT FITTINGS

In this section, we will carry out a detailed comparison of the parameters obtained from Gaussian and pseudo-Voigt decomposition fittings. The left panel of Figure 19 shows a histogram of $\eta_{Lorentz}$, the fraction of the Lorentzian function in the pseudo-Voigt profile, for all CNM and WNM components obtained from pseudo-Voigt absorption and emission fits. For 327 CNM components, 67% (217 out of 327) are pure Gaussian ($\eta_{Lorentz} = 0$), 25% (81/327) are a mixture of Gaussian and Lorentzian functions ($0 < \eta_{Lorentz} < 1$) (and basically in the mixture the components are more Gaussian than Lorentzian), and only 8% (26/303) are pure Lorentzian ($\eta_{Lorentz} = 1$). Of the 284 WNM components, 42% (119/284) are pure Gaussian, 40% (114/284) are mixed, and they in general distribute evenly in the range $0 < \eta_{Lorentz} < 1$, and 18% (51/284) are pure Lorentzian. Our results show that, compared to WNM, the CNM in general appears to have a smaller portion of Lorentzian components.

In the upper right panel of Figure 19 we compare the numbers of WNM and CNM components from Gaussian and pseudo-Voigt fits. In general, Gaussian fits require more components than pseudo-Voigt. For absorption, 44 out of 77 sightlines (57%) require the same numbers of Gaussian and pseudo-Voigt CNM components, 28 sightlines (36%) need more Gaussians (up to 3 components), 5 sightlines (7%) take more pseudo-Voigt components. In the case of emission, most of the sightlines (28/77, or 36%) demand one extra Gaussian component compared to pseudo-Voigt; the number of sightlines having the same number of Gaussian and pseudo-Voigt components is 31 (corresponding to 40%); 10 sightlines (13%) need more Gaussian than pseudo-Voigt from two to three extra components; 11% of the remaining 8 sightlines take at maximum two more pseudo-Voigt components than Gaussian ones. However, when the numbers of free parameters for the two line-shape functions are taken into consideration, pseudo-Voigt fits turn out to require more components than Gaussian in a major part of sightlines, namely 65% for emission and 86% for absorption (as shown in the lower right panel).

The first column of Figure 20 shows violin plots of the widths for both WNM and CNM components derived from Gaussian and pseudo-Voigt fits; the middle column displays violin plots of the FWHM/height ratios for each component. The medians of the widths and the FWHM/height ratios are almost identical, but compared to pseudo-Voigt, the Gaussian fitting needs slightly more wider WNM and CNM components; it also has more broad-but-weak components.

We plot the histograms of τ_{peak} , T_s , T_D and total N_{HI} derived from pseudo-Voigt and Gaussian decompositions in Figure 21. The fittings with the two different line-

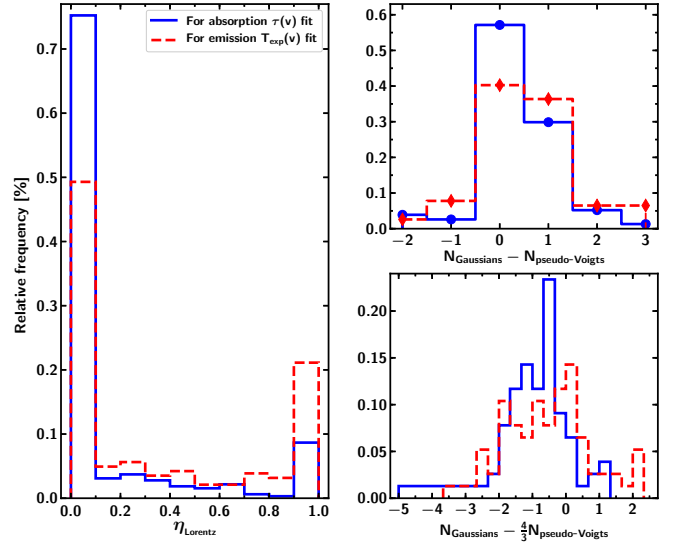


FIG. 19.— Left: Histograms of $\eta_{Lorentz}$, the fraction of Lorentzian in pseudo-Voigt function, for CNM and WNM components from absorption (blue) and emission (red) fits. Right: Comparison of the number of WNM/CNM components from Gaussian and pseudo-Voigt fittings without (top) and with (bottom) consideration of free parameter number for each mathematical function (3 for Gaussian and 4 for pseudo-Voigt).

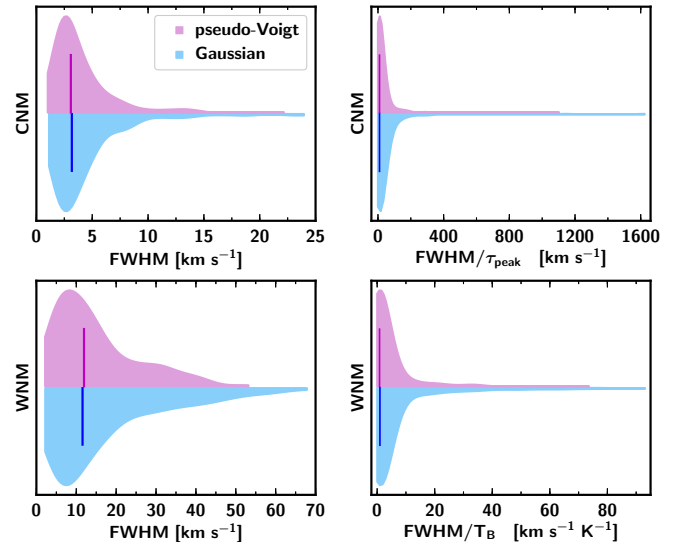


FIG. 20.— Left column: Violin plots for comparing the widths (FWHM) of Gaussian (pink) and pseudo-Voigt (blue) components for CNM (top) and WNM (bottom). Right column: Violin plots of FWHM/ τ_{peak} ratio for CNM and FWHM/ T_B for WNM. The vertical lines show the medians.

shapes appear to be consistent, since the distributions of their properties are almost equivalent. The mean and median values from each pair are close; namely the medians of the Gaussian and pseudo-Voigt fits are (0.35, 0.39) respectively for τ_{peak} , (54.6 K, 55.8 K) for T_s , (2926 K, 3116 K) for T_D and $(23.9, 25.6) \times 10^{20} \text{ cm}^{-2}$ for total N_{HI} . Figure 22 shows the relative difference between N_{HI} as derived from Gaussian and pseudo-Voigt fittings. The distribution is well fit by a Gaussian with a peak at -5.2% and a width of 6.1%. This means the N_{HI} from Gaussian fitting is $\sim 5\%$ slightly lower than that obtained from the pseudo-Voigt fits. This leads us to a conclusion

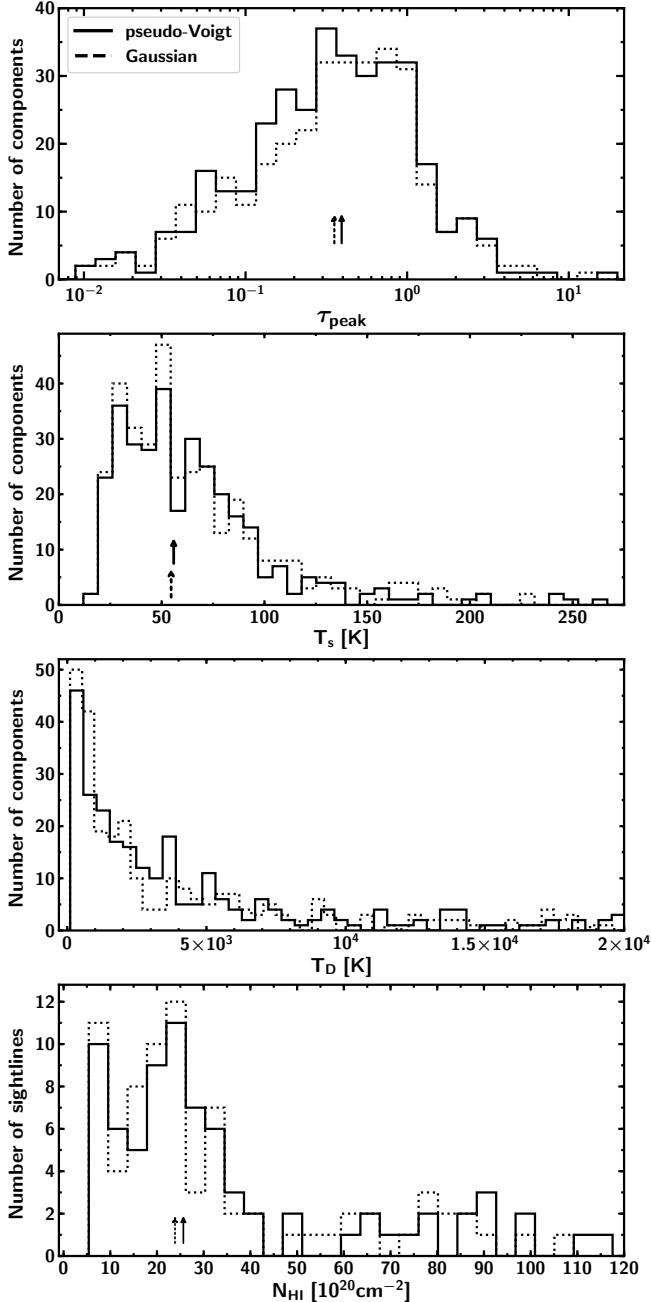


FIG. 21.— Histograms of peak optical depth τ_{peak} , spin temperature T_s , Doppler temperature T_D , and total column density N_{HI} derived from Gaussian (dotted) and pseudo-Voigt (solid) fits.

that the derived properties of Gaussian and pseudo-Voigt fits are compatible.

APPENDIX B: COMPARISON OF T_s AND N_{HI} ESTIMATED FROM OTHER METHODS

Given pairs of emission (off-source) and absorption (on-source) observations, our goal is to combine them to find the spin temperature and column density of interstellar HI. This is challenging because gas at different temperatures can be projected onto the same velocity channel along a line of sight. In a general sense, every sightline will contain a mixture of cold and warm gas: cold gas can be seen in the opacity spectrum; whereas

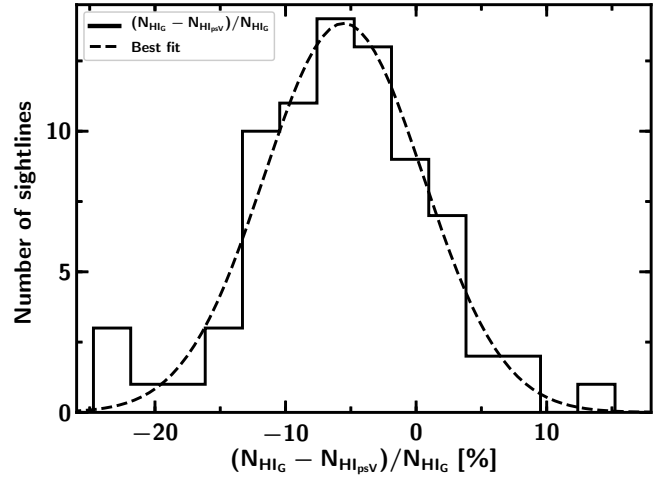


FIG. 22.— Comparison of N_{HI} derived from Gaussian (subscript G) and pseudo-Voigt (subscript psV) fits.

warm gas is almost invisible in the opacity spectrum but is easily detected from the off-source (emission) measurements. Then the question is how best to use on-source and off-source spectra to distinguish these two phases. Beside the multi-component decomposition used in this work, there exist several independent methods to estimate HI spin temperature and column density. In this Section, we will apply two alternative methods (one T_s per velocity channel and single harmonic-mean T_s along full sightline) to derive the spin temperature and column density, and compare their results with those from our spectral decompositions. Similar analyses have been performed by M15, they found that these alternative methods overestimate the spin temperature; and that the Gaussian fit method is the most successful in reproducing the T_s range predicted by theoretical models. We repeat the analyses here for our three regions for completeness.

B1: Isothermal assumption: One T_s per velocity channel

This method is established from the assumption that the gas in each velocity channel is isothermal with a single corresponding spin temperature (e.g. Dickey & Benson 1982; Chengalur et al. 2013; M18). In this case the spin temperature spectrum, $T_{s,\text{chan}}(v)$, can be computed as:

$$T_{s,\text{chan}}(v) = \frac{T_{\text{exp}}(v)}{1 - e^{-\tau(v)}} \quad (19)$$

where $T_{\text{exp}}(v)$ is expected emission profile, $\tau(v)$ is opacity profile, and the effect of the T_{bg} term (see Equation 2) is assumed to be negligible. Here we use this method to calculate spin temperature for each velocity channel above our 5σ detection limit in absorption, with a velocity resolution of 0.16 km s^{-1} . The total column density along the sightline is thus given by:

$$N_{\text{HI}} = C_0 \int \frac{\tau(v) T_{\text{exp}}(v)}{1 - e^{-\tau(v)}} dv \quad (20)$$

B2: Single harmonic-mean T_s along full sightline

This method assumes that there exists a uniform T_s along the full sightline, also known as harmonic-mean

spin temperature, $T_{s,\text{mean}}$, which is computed from the emission and absorption profiles as:

$$T_{s,\text{mean}} = \frac{\int T_{\text{exp}}(v)dv}{\int (1 - e^{-\tau(v)})dv} \quad (21)$$

where the quantities are the same as in Equation 19. Then we calculate N_{HI} as:

$$\begin{aligned} N_{\text{HI}} &= C_0 T_{s,\text{mean}} \int \tau(v)dv \\ &= -C_0 T_{s,\text{mean}} \int \ln \left[1 - \frac{T_{\text{exp}}(v)}{T_{s,\text{mean}}} \right] dv \end{aligned} \quad (22)$$

B3: Comparing T_s and N_{HI} from these methods

We apply both the isothermal channel approximation and the harmonic-mean method to our GNOMES HI data. We then compare the derived T_s and N_{HI} with those from our Gaussian decompositions. The upper panel of Figure 23 shows histograms of the spin temperatures. The $T_{s,\text{chan}}$ from the isothermal channel method spans a large range from 2 K to 4500 K with mean and median of (236 K, 186 K). Meanwhile, the harmonic-mean spin temperatures lie in a much narrower range, from 75 K to 467 K, with a mean and median of (173 K, 157 K). This is not surprising because these two methods both include warm and cold gas in their spin temperature estimates, thus their median temperatures are comparable. For the isothermal channel method, $T_{s,\text{chan}}(v)$ is the mean temperature of the various clouds that contribute to each velocity channel. For the harmonic-mean assumption, $T_{s,\text{mean}}$ is the column density weighted mean spin temperature of all warm and cold clouds along the line of sight. Thus, compared to spin temperatures from Gaussian decomposition fit, both $T_{s,\text{mean}}$ and $T_{s,\text{chan}}$ tend to be higher because the WNM accounts for a significant fraction of the emission along the sightline.

Compared to these methods, the advantage of the spectral decomposition approach is that it separates the two thermal phases within channels, and along the line of sight. As mentioned earlier, our CNM spin temperatures from Gaussian fitting range from 10 K to 465 K, peak at ~ 50 K and have a median of 54.6 K, which is much lower than the estimates from the two single-phase approximations (which include both CNM and WNM). Theoretical models of a thermally bistable ISM (Field et al. 1969; McKee & Ostriker 1977; Wolfire et al. 2003) predict that the neutral CNM has typical temperatures of $30 \lesssim T \lesssim 200$ K. So it is obvious that the spectral decomposition method in the current study successfully reproduces this T_s range. The isothermal channel method gives a large fraction of thermally unstable gas with $500 < T < 5000$ K; by contrast, the T_s distribution from the harmonic-mean method overlaps with the CNM spin temperatures from our Gaussian fits at the high T_s end, but cannot return colder temperatures (since the WNM always makes some contribution along a sightline).

In the bottom panel, we compare N_{HI} derived from the three methods. The column densities from the isothermal channel and harmonic-mean methods are relatively consistent, with differences mostly smaller than 8%. However both underestimate the total N_{HI} by between

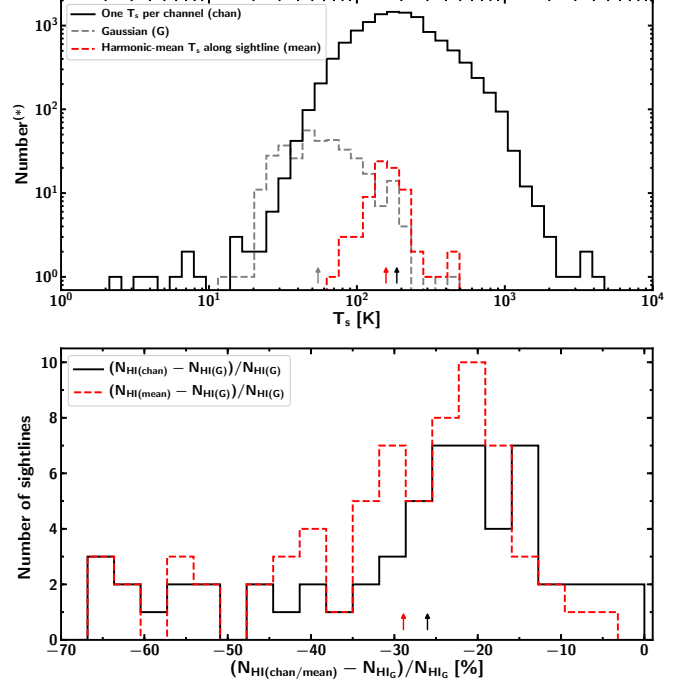


FIG. 23.— Comparison of T_s and N_{HI} derived from different methods: one-phase-per-channel (subscript “chan”) and single harmonic mean T_s along full sightline “mean”. Top panel: Histograms of spin temperatures; black solid line for (chan) and red dashed line for (mean). Spin temperature from HI Gaussian decomposition fit “(G)” is shown in gray for reference. Bottom panel: Relative difference of N_{HI} from isothermal channel (black) method and harmonic-mean assumption (red) compared with decomposition fit. The arrows show the medians.

(*)Note: For (chan): y-axis is the number of velocity channels; for (G): number of components; and for (mean): the number of sightlines.

~ 10 –70% (median $\sim 27\%$) when compared to the Gaussian fits. These differences arise from the fact that the HI gas in the ISM is a complex structure of multiple phases at different temperatures, where cold components contribute significantly to the total gas column density, but that both of the single-phase methods can only return a mean T_s from the mixture of CNM and WNM within a sightline or channel. Based on a Monte Carlo simulation of multi-phase gas, Chengalur et al. (2013) examined how well the per-channel method is able to recover the true column density for gas with a complex spatial and temperature distribution along the sightline. They find that for $N_{\text{HI}} > 10^{21} \text{ cm}^{-2}$, the ratio $[N_{\text{HI}}/N_{\text{HI,chan}}] = -112.88 + 10.144 \times \log_{10} N_{\text{HI}} - 0.2248 \times [\log_{10} N_{\text{HI}}]^2$. In our column density range $(5-120) \times 10^{20} \text{ cm}^{-2}$, this translates to a true N_{HI} that is 20–50% higher than $N_{\text{HI,chan}}$. Our findings are thus in excellent agreement with their predictions.

REFERENCES

- Allison, J. R., Sadler, E. M., & Whiting, M. T. 2012, *PASA*, 29, 221
- Audit, E., & Hennebelle, P. 2005, *A&A*, 433, 1
- Bihl, S., Beuther, H., Ott, J., et al. 2015, *A&A*, 580, A112
- Burkhart, B., Stanimirović, S., Lazarian, A., & Kowal, G. 2010, *ApJ*, 708, 1204
- Calabretta, M. R., Staveley-Smith, L., & Barnes, D. G. 2014, *PASA*, 31, e007
- Chengalur, J. N., Kanekar, N., & Roy, N. 2013, *MNRAS*, 432, 3074
- Condon, J. J., Cotton, W. D., Greisen, E. W., et al. 1998, *AJ*, 115, 1693
- Dame, T. M., Hartmann, D., & Thaddeus, P. 2001, *ApJ*, 547, 792
- Davies, R. D., & Cummings, E. R. 1975, *MNRAS*, 170, 95
- Deguchi, S., & Watson, W. D. 1985, *ApJ*, 290, 578
- Dénes, H., McClure-Griffiths, N. M., Dickey, J. M., Dawson, J. R., & Murray, C. E. 2018, *MNRAS*, 479, 1465
- Dickey, J. M., & Benson, J. M. 1982, *AJ*, 87, 278
- Dickey, J. M., McClure-Griffiths, N. M., Gaensler, B. M., & Green, A. J. 2003, *ApJ*, 585, 801
- Dickey, J. M., Mebold, U., Stanimirovic, S., & Staveley-Smith, L. 2000, *ApJ*, 536, 756
- Dickey, J. M., Salpeter, E. E., & Terzian, Y. 1977, *ApJ*, 211, L77
- Dickey, J. M., Strasser, S., Gaensler, B. M., et al. 2009, *ApJ*, 693, 1250
- Field, G. B. 1958, *Proceedings of the IRE*, 46, 240
- . 1959, *ApJ*, 129, 536
- Field, G. B., Goldsmith, D. W., & Habing, H. J. 1969, *ApJ*, 155, L149
- Fukui, Y., Hayakawa, T., Inoue, T., et al. 2018, *ApJ*, 860, 33
- Fukui, Y., Torii, K., Onishi, T., et al. 2015, *ApJ*, 798, 6
- Garwood, R. W., & Dickey, J. M. 1989, *ApJ*, 338, 841
- Gazol, A., Vázquez-Semadeni, E., Sánchez-Salcedo, F. J., & Scalo, J. 2001, *ApJ*, 557, L121
- Gordon, Y. A., Owers, M. S., Pimblett, K. A., et al. 2017, *MNRAS*, 465, 2671
- Grenier, I. A., Casandjian, J.-M., & Terrier, R. 2005, *Science*, 307, 1292
- Hartmann, D., & Burton, W. B. 1997, *Atlas of Galactic Neutral Hydrogen* (Cambridge University Press), 243
- Heiles, C., & Troland, T. H. 2003a, *ApJS*, 145, 329
- . 2003b, *ApJ*, 586, 1067
- Heitsch, F., Burkert, A., Hartmann, L. W., Slyz, A. D., & Devriendt, J. E. G. 2005, *ApJ*, 633, L113
- Hennebelle, P., & Audit, E. 2007, *A&A*, 465, 431
- Hennebelle, P., Audit, E., & Miville-Deschênes, M. A. 2007, *A&A*, 465, 445
- HI4PI Collaboration, Ben Bekhti, N., Flöer, L., et al. 2016, *A&A*, 594, A116
- Hill, A. S., Mac Low, M.-M., Gatto, A., & Ibáñez-Mejía, J. C. 2018, *ApJ*, 862, 55
- Kalberla, P. M. W., Burton, W. B., Hartmann, D., et al. 2005, *A&A*, 440, 775
- Kalberla, P. M. W., & Haud, U. 2018, *A&A*, 619, A58
- Kanekar, N., Subrahmanyan, R., Chengalur, J. N., & Safouris, V. 2003, *MNRAS*, 346, L57
- Kim, C.-G., Ostriker, E. C., & Kim, W.-T. 2013, *ApJ*, 776, 1
- . 2014, *ApJ*, 786, 64
- Knapp, G. R., & Verschuur, G. L. 1972, *AJ*, 77, 717
- Koyama, H., & Inutsuka, S.-i. 2002, *ApJ*, 564, L97
- Krumholz, M. R., McKee, C. F., & Tumlinson, J. 2009, *ApJ*, 693, 216
- Kulkarni, S. R., & Heiles, C. 1988, *Neutral hydrogen and the diffuse interstellar medium*, ed. K. I. Kellermann & G. L. Verschuur (Springer-Verlag), 95–153
- Lee, M.-Y., Stanimirović, S., Murray, C. E., Heiles, C., & Miller, J. 2015, *ApJ*, 809, 56
- Lee, M.-Y., Stanimirović, S., Douglas, K. A., et al. 2012, *ApJ*, 748, 75
- Leung, C.-M., & Liszt, H. S. 1976, *ApJ*, 208, 732
- Liszt, H. 2001, *A&A*, 371, 698
- . 2014a, *ApJ*, 783, 17
- . 2014b, *ApJ*, 780, 10
- Liszt, H. S., Braun, R., & Greisen, E. W. 1993, *AJ*, 106, 2349
- Lockman, F. J., & Savage, B. D. 1995, *ApJS*, 97, 1
- McKee, C. F., & Ostriker, J. P. 1977, *ApJ*, 218, 148
- Mebold, U., Winnberg, A., Kalberla, P. M. W., & Goss, W. M. 1982, *A&A*, 115, 223
- Meyer, D. M., Lauroesch, J. T., Heiles, C., Peek, J. E. G., & Engelhorn, K. 2006, *ApJ*, 650, L67
- Meyer, D. M., Lauroesch, J. T., Peek, J. E. G., & Heiles, C. 2012, *ApJ*, 752, 119
- Murray, C. E., Peek, J. E. G., Lee, M.-Y., & Stanimirović, S. 2018a, *ApJ*, 862, 131
- Murray, C. E., Stanimirović, S., Goss, W. M., et al. 2018b, *ApJS*, 238, 14
- Murray, C. E., Stanimirović, S., Kim, C.-G., et al. 2017, *ApJ*, 837, 55
- Murray, C. E., Lindner, R. R., Stanimirović, S., et al. 2014, *ApJ*, 781, L41
- Murray, C. E., Stanimirović, S., Goss, W. M., et al. 2015, *ApJ*, 804, 89
- Nguyen, H., Dawson, J. R., Miville-Deschênes, M.-A., et al. 2018, *ApJ*, 862, 49
- Payne, H. E., Terzian, Y., & Salpeter, E. E. 1982, *ApJS*, 48, 199
- Peek, J. E. G., Heiles, C., Douglas, K. A., et al. 2011, *ApJS*, 194, 20
- Peek, J. E. G., Babler, B. L., Zheng, Y., et al. 2018, *ApJS*, 234, 2
- Planck Collaboration, Fermi Collaboration, Ade, P. A. R., et al. 2015, *A&A*, 582, A31
- Radhakrishnan, V., Murray, J. D., Lockhart, P., & Whittle, R. P. J. 1972, *ApJS*, 24, 15
- Reich, P., Testori, J. C., & Reich, W. 2001, *A&A*, 376, 861
- Remy, Q., Grenier, I. A., Marshall, D. J., & Casandjian, J. M. 2017, *A&A*, 601, A78
- Roy, N., Kanekar, N., Braun, R., & Chengalur, J. N. 2013, *MNRAS*, 436, 2352
- Saury, E., Miville-Deschênes, M.-A., Hennebelle, P., Audit, E., & Schmidt, W. 2014, *A&A*, 567, A16
- Shaw, G., Ferland, G. J., & Hubeny, I. 2017, *ApJ*, 843, 149
- Silk, J. 1975, *ApJ*, 198, L77
- Silk, J., & Werner, M. W. 1969, *ApJ*, 158, 185
- Stanimirović, S., & Heiles, C. 2005, *ApJ*, 631, 371
- Stanimirović, S., Heiles, C., & Kanekar, N. 2007, in *Astronomical Society of the Pacific Conference Series*, Vol. 365, *SINS - Small Ionized and Neutral Structures in the Diffuse Interstellar Medium*, ed. M. Haverkorn & W. M. Goss, 22
- Stanimirović, S., Murray, C. E., Lee, M.-Y., Heiles, C., & Miller, J. 2014, *ApJ*, 793, 132
- Stanimirović, S., Putman, M., Heiles, C., et al. 2006, *ApJ*, 653, 1210
- Wakker, B. P., Lockman, F. J., & Brown, J. M. 2011, *ApJ*, 728, 159
- Wannier, P., Andersson, B.-G., Penprase, B. E., & Federman, S. R. 1999, *ApJ*, 510, 291
- Watson, W. D. 1972, *ApJ*, 176, 103
- Wertheim, G. K., Butler, M. A., West, K. W., & Buchanan, D. N. E. 1974, *Review of Scientific Instruments*, 45, 1369
- Wolfire, M. G., Hollenbach, D., & McKee, C. F. 2010, *ApJ*, 716, 1191
- Wolfire, M. G., Hollenbach, D., McKee, C. F., Tielens, A. G. G. M., & Bakes, E. L. O. 1995, *ApJ*, 443, 152
- Wolfire, M. G., McKee, C. F., Hollenbach, D., & Tielens, A. G. G. M. 2003, *ApJ*, 587, 278
- Wouthuysen, S. A. 1952, *AJ*, 57, 31

TABLE 3
PARAMETERS FOR PSEUDO-VOIGT AND GAUSSIAN FITS
(SEE SECTION 4 FOR DETAILED DESCRIPTIONS)

| l/b | (arcsec) | pseudo-Voigt | | | | | | | | | | Gaussian | | | | | | | | | |
|---------------|-------------------|--------------|-------------------------|-------------------------------------|--------------------------------------|--------------|--------------|--|-------------------|--------------|-------------------------|-------------------------------------|--------------------------------------|--------------|--|-------------------|--|--|--|--|--|
| | | T_B (K) | τ (10^{-2}) | V_{lsr} (km s^{-1}) | ΔV (km s^{-1}) | η | T_s (K) | N_{HI} (10^{20} cm^{-2}) | $F_{\text{or O}}$ | T_B (K) | τ (10^{-2}) | V_{lsr} (km s^{-1}) | ΔV (km s^{-1}) | T_s (K) | N_{HI} (10^{20} cm^{-2}) | $F_{\text{or O}}$ | | | | | |
| 188.07/0.04 | 24.81 | 1.84±0.1 | -2.29±0.03 | 1.53±0.06 | 0.0±0.0 | 29.49±2.21 | 1.61±0.16 | 2 | 29.13 | 1.87±0.01 | -2.29±0.0 | 1.5±0.01 | 34.44±0.74 | 1.87±0.04 | 2 | | | | | | |
| 188.07/0.04 | 37.12 | 0.63±0.02 | 0.98±0.32 | 5.99±0.37 | 0.0±0.0 | 79.42±17.9 | 5.86±1.39 | 1 | 37.11 | 0.63±0.0 | 1.02±0.04 | 6.14±0.05 | 58.0±3.46 | 4.37±0.26 | 4 | | | | | | |
| 188.07/0.04 | 59.76 | 1.1±0.13 | 4.42±0.13 | 1.99±0.28 | 0.0±0.0 | 89.58±9.69 | 3.8±0.8 | 3 | 33.89 | 1.1±0.01 | 4.47±0.01 | 2.06±0.02 | 50.8±2.77 | 2.23±0.13 | 3 | | | | | | |
| 188.07/0.04 | 48.47 | 1.08±0.11 | 7.32±0.18 | 2.75±0.61 | 0.0±0.0 | 73.39±7.99 | 4.23±1.13 | 3 | 30.27 | 0.78±0.02 | 7.28±0.01 | 2.44±0.04 | 48.45±3.4 | 2.25±0.17 | 0 | | | | | | |
| 188.07/0.04 | 16.08 | 0.55±0.04 | 10.78±0.43 | 3.51±1.16 | 0.0±0.0 | 38.01±12.07 | 1.44±0.67 | 4 | 34.67 | 0.56±0.0 | 10.69±0.05 | 4.95±0.15 | 80.86±6.19 | 4.35±0.36 | 5 | | | | | | |
| 188.07/0.04 | 11.44 | 0.64±0.04 | 15.61±0.2 | 3.98±0.36 | 0.0±0.0 | 24.2±2.93 | 1.19±0.19 | 5 | 13.23 | 0.67±0.0 | 15.88±0.02 | 3.28±0.02 | 27.1±2.65 | 1.16±0.11 | 1 | | | | | | |
| 188.07/0.04 | 49.37±2.93 | <0.035 | -2.86±0.32 | 9.38±0.49 | 1.0±0.0 | >1410.7 | 13.25±1.05 | 0.31±0.13 | 10.08±0.48 | <0.038 | 1.64±0.2 | 34.56±0.49 | >263.34 | 6.76±0.33 | 0.41±0.01 | | | | | | |
| 188.07/0.04 | 54.14±8.22 | <0.05 | 1.79±0.09 | 3.66±0.33 | 0.0±0.0 | >1076.34 | 3.85±0.68 | 0.53±0.16 | 110.31±3.23 | <0.068 | 4.14±0.22 | 14.69±0.26 | >1617.88 | 31.43±1.07 | 0.3±0.01 | | | | | | |
| 188.07/0.04 | 39.81±13.95 | <0.086 | 9.87±0.92 | 7.2±1.85 | 0.24±0.14 | >461.11 | 6.19±2.72 | 0.33±0.1 | - | - | - | - | - | - | - | | | | | | |
| 188.07/0.04 | 85.79±13.53 | <0.089 | 9.88±0.92 | 15.22±0.52 | 0.0±0.0 | >962.55 | 25.34±4.09 | 0.43±0.15 | - | - | - | - | - | - | - | | | | | | |
| 188.07/0.04 | 188.07/0.04 | - | - | - | - | - | - | - | - | - | - | - | - | - | - | | | | | | |
| 187.41/-11.34 | 5.79 | 0.04±0.0 | -21.53±0.11 | 2.61±0.32 | 0.19±0.27 | 147.78±9.17 | 0.3±0.06 | 0 | 35.13±3.66 | <0.062 | 14.68±0.46 | 11.45±0.39 | >569.53 | 7.8±0.85 | >0.17±0.01 | | | | | | |
| 187.41/-11.34 | 2.59 | 0.02±0.0 | -6.21±0.32 | 4.35±0.77 | 0.44±0.39 | 130.6±15.78 | 0.33±0.1 | 1 | 2.07 | 0.01±0.0 | -6.62±0.13 | 2.5±0.42 | 207.55±26.95 | 0.11±0.03 | 6 | | | | | | |
| 187.41/-11.34 | 18.86 | 0.25±0.01 | -0.48±0.07 | 3.19±0.11 | 0.07±0.17 | 85.24±22.27 | 1.37±0.14 | 3 | 13.65 | 0.25±0.0 | -0.4±0.04 | 2.96±0.06 | 61.69±2.19 | 0.89±0.04 | 5 | | | | | | |
| 187.41/-11.34 | 17.21 | 0.22±0.01 | 1.6±0.05 | 2.14±0.13 | 1.0±0.0 | 87.16±3.22 | 1.19±0.11 | 2 | 8.09 | 0.17±0.01 | 1.62±0.02 | 1.409±0.26 | 51.74±3.71 | 0.31±0.03 | 4 | | | | | | |
| 187.41/-11.34 | 16.49 | 1.06±0.01 | 6.43±0.02 | 2.35±0.03 | 0.0±0.0 | 25.23±2.72 | 1.22±0.13 | 4 | 31.18 | 0.06±0.0 | 2.37±0.17 | 14.09±0.26 | 479.28±12.24 | 7.26±0.35 | 2 | | | | | | |
| 187.41/-11.34 | 9.23 | 0.43±0.01 | 9.17±0.06 | 2.73±0.1 | 0.15±0.03 | 26.4±4.44 | 0.64±0.11 | 5 | 18.8 | 0.4±0.0 | 9.16±0.02 | 2.7±0.03 | 57.03±2.56 | 1.2±0.06 | 1 | | | | | | |
| 187.41/-11.34 | 3.71±0.31 | <0.012 | -18.22±2.47 | 51.07±2.58 | 0.0±0.0 | >305.44 | 3.68±0.36 | 0.47±0.3 | 2.9±0.12 | <0.004 | -29.83±1.63 | 37.84±2.17 | >828.55 | 2.13±0.15 | 0.51±0.02 | | | | | | |
| 187.41/-11.34 | 18.741/-11.34 | - | - | - | - | - | - | - | - | - | - | - | - | - | - | | | | | | |
| 187.41/-11.34 | 29.28±2.42 | <0.008 | 3.21±0.29 | 16.37±0.2 | 0.1±0.09 | >3507.26 | 9.76±0.91 | 0.32±0.25 | 7.99±0.45 | <0.009 | 2.16±0.57 | 29.75±1.03 | >884.8 | 4.61±0.3 | 0.47±0.02 | | | | | | |
| 187.41/-11.34 | 30.35±2.84 | <0.017 | 7.32±0.11 | 6.4±0.28 | 0.35±0.23 | >1778.38 | 4.4±0.62 | 0.41±0.28 | 18.5±0.63 | <0.01 | 6.95±0.14 | 9.68±0.38 | >1810.39 | 3.47±0.18 | 0.44±0.01 | | | | | | |
| 193.12/8.3 | 27.1 | 0.12±0.03 | -9.22±0.44 | 8.78±0.59 | 0.0±0.0 | 239.62±2.68 | 4.99±1.21 | 4 | - | - | - | - | - | - | - | | | | | | |
| 193.12/8.3 | 40.84 | 1.55±0.15 | -7.52±0.04 | 1.85±0.12 | 0.27±0.18 | 51.84±0.85 | 3.27±0.46 | 1 | 35.02 | 0.21±0.0 | -8.52±0.02 | 7.92±0.06 | 184.86±1.63 | 5.88±0.09 | 3 | | | | | | |
| 193.12/8.3 | 6.33 | 0.08±0.01 | 6.4±0.21 | 4.96±0.5 | 0.0±0.0 | 82.34±2.82 | 0.65±0.09 | 2 | 8.0 | 0.08±0.0 | -7.52±0.0 | 1.45±0.01 | 51.97±0.89 | 2.64±0.05 | 2 | | | | | | |
| 193.12/8.3 | 4.56 | 0.05±0.01 | 12.36±0.29 | 2.58±0.66 | 0.0±0.0 | 93.41±5.73 | 0.25±0.09 | 3 | 6.01 | 0.05±0.0 | 12.36±0.04 | 5.09±0.1 | 104.0±2.56 | 0.83±0.03 | 1 | | | | | | |
| 193.12/8.3 | 2.86 | 0.04±0.01 | 17.73±0.37 | 4.1±1.0 | 0.0±0.0 | 70.70±3.34 | 0.22±0.07 | 3 | 3.82 | 0.04±0.0 | 17.76±0.07 | 4.21±0.2 | 123.19±5.39 | 0.33±0.02 | 4 | | | | | | |
| 193.12/8.3 | 0.53 | 0.05±0.01 | 24.46±0.27 | 2.89±0.63 | 0.0±0.0 | 18.09±5.25 | 0.03±0.01 | 5 | 0.75 | 0.03±0.0 | 24.48±0.07 | 2.89±0.16 | 25.42±4.96 | 0.05±0.01 | 5 | | | | | | |
| 193.12/8.3 | 0.98±0.05 | <0.013 | -56.83±0.54 | 20.92±1.75 | 1.0±0.0 | >73.77 | 0.59±0.06 | 1.0±0.0 | 21.26±0.11 | <0.011 | -57.32±0.53 | 25.44±1.42 | >78.6 | 0.43±0.03 | 1.0±0.0 | | | | | | |
| 193.12/8.3 | 22.04±0.14 | <0.023 | 6.43±0.07 | 30.18±0.17 | 0.04±0.02 | >950.77 | 13.12±0.17 | 0.26±0.01 | - | - | - | - | - | - | - | | | | | | |
| 166.64/-33.6 | 1.41 | 0.02±0.0 | -8.99±0.08 | 2.43±0.21 | 0.0±0.0 | 71.38±8.83 | 0.07±0.01 | 0 | 1.66 | 0.02±0.0 | -8.92±0.08 | 2.75±0.18 | 83.72±12.21 | 0.08±0.01 | 0 | | | | | | |
| 166.64/-33.6 | 20.27 | 0.39±0.01 | -0.48±0.09 | 4.19±0.09 | 0.0±0.0 | 62.78±7.29 | 2.01±0.24 | 1 | 29.65 | 0.4±0.0 | -0.41±0.02 | 4.28±0.02 | 89.93±2.31 | 3.0±0.08 | 4 | | | | | | |
| 166.64/-33.6 | 7.9 | 0.21±0.02 | 1.22±0.03 | 1.74±0.13 | 0.0±0.0 | 41.69±5.66 | 0.29±0.05 | 1 | 8.38 | 0.19±0.0 | 1.23±0.01 | 1.63±0.04 | 48.41±2.54 | 0.3±0.02 | 3 | | | | | | |
| 166.64/-33.6 | 5.83 | 0.09±0.01 | 6.65±0.22 | 4.54±0.38 | 0.0±0.0 | 67.75±8.25 | 0.55±0.11 | 3 | 12.21 | 0.11±0.0 | 6.85±0.03 | 1.44±0.06 | 117.21±18.3 | 1.0±0.16 | 2 | | | | | | |
| 166.64/-33.6 | 7.07 | 0.04±0.01 | 7.68±0.21 | 1.84±0.62 | 0.0±0.0 | 180.35±24.08 | 0.27±0.14 | 2 | 4.76 | 0.03±0.0 | 7.91±0.04 | 1.22±0.12 | 161.12±40.51 | 0.11±0.03 | 1 | | | | | | |
| 166.64/-33.6 | 28.87±4.44 | <0.009 | -1.03±0.15 | 6.92±0.48 | 1.0±0.0 | >3289.69 | 5.72±0.97 | 0.51±0.09 | 4.22±0.37 | <0.01 | -0.78±0.43 | 24.9±0.78 | >439.01 | 2.04±0.19 | 0.47±0.08 | | | | | | |
| 166.64/-33.6 | 15.37±0.96 | <0.011 | 4.42±0.22 | 12.02±0.28 | 0.0±0.0 | >1459.71 | 3.58±0.24 | 0.45±0.08 | 25.56±2.29 | <0.01 | 0.05±0.43 | 9.08±0.42 | >2496.26 | 4.5±0.45 | 0.36±0.08 | | | | | | |
| 166.64/-33.6 | 3.31 | 0.18±0.02 | -11.92±0.05 | 1.4±0.14 | 0.02±0.33 | 20.07±1.5 | 0.1±0.02 | 0 | 7.3±2.43 | <0.019 | 8.35±1.74 | 8.92±1.6 | >389.75 | 1.26±0.48 | 0.4±0.07 | | | | | | |
| 201.53/0.51 | 85.13 | 2.91±0.36 | 4.63±0.06 | 4.37±0.2 | 0.17±0.06 | 90.03±2.94 | 24.08±3.36 | 4 | 65.65 | 3.51±0.05 | 4.66±0.01 | 1.35±0.04 | 23.41±1.66 | 0.11±0.01 | 0 | | | | | | |
| 201.53/0.51 | 18.26 | 0.41±0.02 | 13.18±1.27 | 20.48±1.36 | 0.0±0.0 | 54.28±11.54 | 8.9±2.02 | 2 | 33.07 | 0.48±0.0 | 12.72±0.12 | 23.0±0.2 | 67.67±5.44 | 18.04±0.96 | 6 | | | | | | |
| 201.53/0.51 | 26.11 | 0.33±0.06 | 20.59±0.18 | 1.76±0.55 | 1.0±0.0 | 92.91±3.85 | 1.55±0.57 | 1 | 17.39 | 0.25±0.01 | 20.43±0.03 | 1.54±0.07 | 86.76±5.92 | 18.4±4.31 | 7 | | | | | | |
| 201.53/0.51 | 24.11 | 0.71±0.08 | 23.37±0.13 | 2.52±0.3 | 0.0±0.0 | 47.42±2.02 | 1.64±0.28 | 1 | 21.36 | 0.74±0.01 | 23.39±0.02 | 3.09±0.05 | 40.85±3.1 | 1.82±0.14 | 5 | | | | | | |
| 201.53/0.51 | 25.46 | 0.51±0.03 | 31.41±0.37 | 10.77±0.57 | 0.0±0.0 | 63.72±2.78 | 6.83±0.64 | 5 | 27.86 | 0.55±0.01 | 31.0±0.06 | 6.55±0.13 | 65.89±2.04 | 4.63±0.18 | 2 | | | | | | |
| 201.53/0.51 | 20.74 | 1.94±0.32 | 33.74±0.05 | 1.34±0.12 | 0.0±0.0 | 24.22±1.0 | 1.23±0.24 | 3 | 8.49 | 1.91±0.03 | 33.8±0.01 | 1.47±0.02 | 25.66±0.94 | 1.39±0.06 | 3 | | | | | | |
| 201.53/0.51 | - | - | - | - | - | - | - | - | 29.4±5.46 | 0.13±0.0 | 39.0±0.12 | 5.35±0.21 | 69.67±5.03 | 0.97±0.08 | 4 | | | | | | |
| 201.53/0.51 | 59.64±2.73 | <0.148 | 5.69±0.24 | 14.94±0.31 | 0.41±0.03 | >401.98 | 20.66±1.06 | 0.0±0.0 | - | - | 3.3±0.76 | 16.44±0.72 | >282.22 | 9.37±1.79 | 0.5±0.0 | | | | | | |
| 201.53/0.51 | 63.39±2.08 | <0.061 | 24.84±0.39 | 20.76±0.32 | 0.0±0.0 | >1038.28 | 25.52±0.93 | 0.34±0.01 | 15.36±1.14 | <0.052 | 8.68±0.12 | 3.41±0.3 | >298.1 | 1.02±0.12 | 0.5±0.0 | | | | | | |
| 201.53/0.51 | 1.38 | 0.01±0.0 | -23.1±0.2 | 3.69±0.48 | 0.0±0.0 | 138.2±10.03 | 0.12±0.02 | 0 | 59.8±3.8 | <0.074 | 25.41±0.74 | 20.51±0.55 | >806.11 | 23.79±1.64 | 0.5±0.0 | | | | | | |
| 186.76/-7.11 | 29.84 | 0.5±0.02 | 1.77±0.02 | 2.15±0.07 | 0.19±0.12 | 75.84±2.89 | 1.73±0.15 | 1 | 11.29 | 0.48±0.0 | 1.76±0.0 | 2.08±0.01 | 29.62±10.55 | 0.58±0.21 | 3 | | | | | | |
| 186.76/-7.11 | 51.78 | 0.22±0.01 | 5.78±0.23 | 7.95±0.3 | 0.0±0.0 | 262.22±10.78 | 8.73±0.54 | 2 | 14.51 | 0.22±0.0 | 5.53±0.03 | 1.87±0.05 | 73.48±71.36 | 2.67±2.61 | 1 | | | | | | |
| 186.76/-7.11 | 10.65 | 0.16±0.01 | 1.99±0.11 | 1.99±0.11 | 0.0±0.0 | 72.04±6.56 | 0.44±0.05 | 3 | 12.8 | 0.17±0.0 | 9.59±0.01 | 1.88±0.03 | 81.88±6.57 | 0.49±0.05 | 2 | | | | | | |
| 186.76/-7.11 | 28.19±3.17 | <0.014 | -1.35±0.22 | 17.78±1.02 | 1.0±0.0 | >1972.23 | 14.33±1.81 | 0.42±0.16 | 15.23±2.99 | <0.018 | -1.14±1.47 | 10.43±1.41 | >763.65 | 2.8±0.7 | 0.4±0.16 | | | | | | |
| 186.76/-7.11 | - | - | - | - | - | - | - | - | 15.28±0.3 | <0.021 | 0.32±0.09 | 34.7±0.3 | >739.53 | 10.29±0.22 | 0.38±0.16 | | | | | | |
| 186.76/-7.11 | - | - | - | - | - | - | - | - | 25.11±2.7 | <0.021 | 1.69±0.07 | 4.46±0.4 | >1193.81 | 2.17±0.31 | 0.26±0.14 | | | | | | |
| 186.76/-7.11 | 10.44±2.75 | <0.014 | 9.74±2.51 | 17.15±2.11 | 0.0±0.0 | >760.84 | 3.47±1.01 | 0.51±0.17 | 45.66±13.25 | <0.011 | 7.38±0.66 | 9.31±0.28 | >3994.02 | 8.28±2.41 | 0.4±0.16 | | | | | | |
| 186.76/-7.11 | 12.41±0.81 | <0.015 | 10.48±0.11 | 4.86±0.19 | 0.0±0.0 | >842.07 | 1.17±0.09 | 0.5±0.17 | - | - | - | - | - | - | - | | | | | | |

Warm and cold HI gas in the Taurus and Gemini regions

TABLE 3 (CONT)

| l/b ($^{\circ}$) | Pseudo-Voigt | | | | | | | | | | Gaussian | | | | | | | | | |
|-----------------------|--------------|-------------------------|-------------------------------|--------------------------------|------------|--------------|------------------------------------|-------------|--------------|-------------------------|-------------------------------|--------------------------------|--------------|------------------------------------|-------------|--|--|--|--|--|
| | T_B (K) | τ (10^{-2}) | V_{str} ($km\ s^{-1}$) | ΔV ($km\ s^{-1}$) | η | T_s (K) | N_{HI} ($10^{20}\ cm^{-2}$) | $F_{or\ O}$ | T_B (K) | τ (10^{-2}) | V_{str} ($km\ s^{-1}$) | ΔV ($km\ s^{-1}$) | T_s (K) | N_{HI} ($10^{20}\ cm^{-2}$) | $F_{or\ O}$ | | | | | |
| 203.75/14.63 | 5.2 | 0.06±0.01 | -3.46±0.28 | 3.29±0.67 | 0.0±0.0 | 89.3±6.49 | 0.33±0.09 | 1 | 6.59 | 0.08±0.0 | -2.9±0.08 | 4.62±0.18 | 85.6±6.15 | 0.6±0.05 | 1 | | | | | |
| 203.75/14.63 | - | - | - | - | - | - | - | 0 | 8.66 | 0.13±0.0 | 0.67±0.03 | 2.24±0.08 | 71.0±3.89 | 0.39±0.03 | 1 | | | | | |
| 203.75/14.63 | 9.51 | 0.15±0.01 | 0.66±0.14 | 3.01±0.51 | 1.0±0.0 | 68.3±3.52 | 0.87±0.17 | 0 | 2.88 | 0.06±0.0 | 4.95±0.25 | 5.91±0.41 | 49.4±13.8 | 0.31±0.09 | 2 | | | | | |
| 203.75/14.63 | 3.89 | 0.12±0.01 | 6.51±0.11 | 2.23±0.32 | 0.49±0.38 | 34.36±3.1 | 0.23±0.06 | 2 | 2.19 | 0.09±0.0 | 6.66±0.03 | 1.76±0.09 | 25.4±4.59 | 0.08±0.01 | 0 | | | | | |
| 203.75/14.63 | - | <0.021 | 0.22±0.16 | - | - | >491.94 | - | 0.5±0.3 | - | - | - | - | - | - | - | | | | | |
| 203.75/14.63 | 5.56±0.32 | <0.025 | 6.56±0.28 | 30.17±0.92 | 0.33±0.07 | >218.61 | 3.77±0.27 | 1.0±0.3 | 2.51±0.43 | <0.022 | 6.66±0.05 | 4.1±2.42 | >98.6 | 0.2±0.07 | 0 | | | | | |
| 203.75/14.63 | 1.64±0.43 | <0.027 | 11.86±0.15 | 2.23±0.41 | 0.06±0.67 | >59.73 | 0.07±0.03 | 1.0±0.0 | 1.72±0.27 | 0.0025 | 11.68±0.15 | 2.23±0.4 | >78.3 | 0.07±0.32 | 0.5±0.08 | | | | | |
| 203.75/14.63 | - | - | - | - | - | - | - | - | 1.3±0.33 | <0.013 | 17.17±1.63 | 13.88±2.8 | >97.26 | 0.35±0.11 | 0.48±0.08 | | | | | |
| 196.84/-13.74 | 9.54 | 0.12±0.02 | -8.86±0.13 | 1.96±0.25 | 0.0±0.0 | 84.39±3.84 | 0.4±0.09 | 0 | 10.83 | 0.12±0.0 | -8.85±0.02 | 2.05±0.05 | 95.77±3.39 | 0.46±0.02 | 3 | | | | | |
| 196.84/-13.74 | - | - | - | - | - | - | - | - | 10.16 | 0.23±0.02 | 3.5±0.21 | 3.13±0.22 | 49.4±3.02 | 0.68±0.09 | 0 | | | | | |
| 196.84/-13.74 | 17.98 | 1.23±0.05 | 4.76±0.04 | 2.09±0.09 | 0.16±0.07 | 25.41±0.65 | 1.36±0.69 | 2 | 19.41 | 1.2±0.04 | 4.86±0.01 | 1.61±0.03 | 27.78±0.66 | 1.04±0.05 | 4 | | | | | |
| 196.84/-13.74 | - | - | - | - | - | - | - | - | 13.45 | 0.51±0.02 | 8.58±0.01 | 1.45±0.04 | 33.67±1.13 | 0.49±0.03 | 2 | | | | | |
| 196.84/-13.74 | 21.0 | 0.82±0.41 | 8.47±0.08 | 1.98±0.39 | 0.0±0.0 | 37.52±0.8 | 1.18±0.64 | 1 | 23.35 | 0.73±0.02 | 8.89±0.02 | 3.48±0.03 | 45.07±1.52 | 2.23±0.09 | 1 | | | | | |
| 196.84/-13.74 | 19.27 | 0.46±0.27 | 9.48±0.96 | 3.21±0.78 | 0.0±0.0 | 52.27±1.87 | 1.49±0.95 | 3 | - | - | - | - | - | - | - | | | | | |
| 196.84/-13.74 | 8.96±0.13 | <0.025 | -8.21±0.23 | 13.33±0.54 | 0.78±0.06 | >364.78 | 3.17±0.15 | 0.5±0.29 | 14.21±0.26 | <0.04 | 6.59±0.12 | 28.29±0.19 | >356.95 | 7.8±0.15 | 0.38±0.08 | | | | | |
| 196.84/-13.74 | 54.18±0.52 | <0.026 | 6.77±0.05 | 9.01±0.09 | 0.0±0.0 | >2073.91 | 9.47±0.13 | 0.28±0.18 | 41.27±0.66 | <0.029 | 7.25±0.04 | 8.13±0.08 | >1447.46 | 6.51±0.12 | 0.17±0.05 | | | | | |
| 196.84/-13.74 | 16.22±0.16 | <0.038 | 18.08±0.14 | 12.18±0.24 | 0.37±0.03 | >428.69 | 4.51±0.12 | 0.5±0.29 | - | - | - | - | - | - | - | | | | | |
| 196.84/-13.74 | 42.77 | 0.69±0.07 | 3.48±0.19 | 2.93±0.18 | 1.0±0.0 | 85.81±1.91 | 4.95±0.63 | 0 | 8.19±0.2 | <0.026 | 18.97±0.1 | 8.91±0.25 | >311.69 | 1.43±0.05 | 0.5±0.08 | | | | | |
| 196.64/0.17 | 39.49 | 0.64±0.07 | 6.05±0.14 | 2.4±0.42 | 0.0±0.0 | 83.53±2.42 | 2.47±0.51 | 1 | 53.86 | 0.73±0.01 | 4.41±0.06 | 4.96±0.07 | 103.95±1.01 | 7.27±0.15 | 5 | | | | | |
| 196.64/0.17 | - | - | - | - | - | - | - | - | 31.03 | 0.37±0.04 | 6.3±0.06 | 1.55±0.11 | 110.33±2.38 | 1.13±0.15 | 8 | | | | | |
| 196.64/0.17 | 64.56 | 1.05±0.09 | 10.49±0.13 | 4.48±0.43 | 0.0±0.0 | 99.33±1.13 | 9.04±1.17 | 5 | 52.15 | 0.63±0.05 | 8.68±0.23 | 2.58±0.53 | 111.57±1.49 | 3.52±0.77 | 4 | | | | | |
| 196.64/0.17 | - | - | - | - | - | - | - | - | 67.86 | 1.25±0.15 | 10.52±0.05 | 1.81±0.11 | 95.11±0.97 | 4.17±0.58 | 2 | | | | | |
| 196.64/0.17 | - | - | - | - | - | - | - | - | 55.02 | 0.91±0.03 | 12.69±0.03 | 1.95±0.08 | 92.09±1.3 | 3.16±0.17 | 9 | | | | | |
| 196.64/0.17 | - | - | - | - | - | - | - | - | 20.2 | 0.39±0.04 | 15.5±0.04 | 2.96±0.19 | 62.55±2.41 | 1.39±0.19 | 6 | | | | | |
| 196.64/0.17 | 40.43 | 0.67±0.04 | 18.12±0.53 | 12.01±1.61 | 0.0±0.0 | 82.79±3.46 | 12.91±1.98 | 6 | 46.15 | 0.6±0.02 | 19.24±0.03 | 2.77±0.09 | 102.28±1.33 | 8.29±0.14 | 7 | | | | | |
| 196.64/0.17 | 51.48 | 0.42±0.08 | 19.38±0.16 | 2.08±0.42 | 0.0±0.0 | 150.11±6.2 | 2.55±0.71 | 2 | 30.1 | 0.48±0.02 | 20.59±0.4 | 11.45±0.36 | 78.95±2.99 | 3.38±0.54 | 1 | | | | | |
| 196.64/0.17 | 28.32 | 0.55±0.17 | 26.44±0.12 | 1.14±0.34 | 0.0±0.0 | 66.94±1.82 | 0.82±0.35 | 3 | 37.03 | 0.78±0.03 | 26.48±0.02 | 1.37±0.04 | 68.37±1.22 | 1.41±0.08 | 4 | | | | | |
| 196.64/0.17 | 45.61 | 1.04±0.09 | 27.5±0.18 | 3.01±0.28 | 0.0±0.0 | 70.54±0.86 | 4.29±0.54 | 4 | 44.06 | 0.95±0.01 | 28.06±0.04 | 2.56±0.05 | 71.85±0.91 | 3.37±0.1 | 3 | | | | | |
| 196.64/0.17 | - | <0.054 | 6.4±0.12 | 11.37±0.29 | 1.0±0.0 | >1233.03 | 21.5±1.14 | 0.39±0.04 | 2.28±0.11 | <0.016 | -16.55±1.62 | 28.68±2.62 | >142.31 | 1.27±0.13 | 0.5±0.02 | | | | | |
| 196.64/0.17 | 66.04±3.08 | - | - | - | - | - | - | - | 100.82±1.88 | <0.063 | 18.38±0.07 | 24.85±0.17 | >1594.08 | 4.8±0.96 | 0.0±0.0 | | | | | |
| 196.64/0.17 | - | <0.073 | 18.96±0.19 | 21.24±0.14 | 0.0±0.0 | >1057.99 | 31.87±1.06 | 0.14±0.02 | - | - | - | - | - | - | - | | | | | |
| 196.64/0.17 | 26.25 | 0.32±0.16 | 1.54±0.89 | 2.53±0.74 | 0.48±0.39 | 95.85±1.84 | 1.83±1.09 | 0 | - | - | - | - | - | - | - | | | | | |
| 173.15/-33.29 | - | - | - | - | - | - | - | - | 30.12 | 0.54±0.04 | 3.17±0.19 | 4.36±0.15 | 72.18±4.38 | 3.33±0.32 | 1 | | | | | |
| 173.15/-33.29 | 43.37 | 1.03±0.19 | 3.49±0.15 | 1.9±0.63 | 0.0±0.0 | 67.45±0.64 | 2.55±0.96 | 3 | 17.99 | 0.58±0.04 | 3.48±0.02 | 1.47±0.05 | 40.87±2.71 | 0.68±0.07 | 4 | | | | | |
| 173.15/-33.29 | 39.11 | 1.1±0.12 | 5.37±0.17 | 1.65±0.33 | 0.0±0.0 | 58.63±1.05 | 2.06±0.48 | 1 | 23.35 | 0.93±0.05 | 5.36±0.01 | 1.68±0.04 | 38.57±3.12 | 1.17±0.12 | 3 | | | | | |
| 173.15/-33.29 | 12.96 | 0.34±0.19 | 8.55±0.3 | 1.14±0.73 | 0.0±0.0 | 44.95±3.77 | 0.34±0.29 | 4 | 33.35 | 0.35±0.02 | 8.57±0.03 | 1.27±0.09 | 112.92±21.12 | 0.98±0.21 | 2 | | | | | |
| 173.15/-33.29 | 42.25 | 2.06±0.1 | 9.35±0.08 | 4.24±0.13 | 0.0±0.02 | 48.42±4.54 | 8.23±0.91 | 2 | 24.15 | 2.06±0.02 | 9.39±0.02 | 4.15±0.02 | 27.68±7.82 | 4.58±1.3 | 0 | | | | | |
| 173.15/-33.29 | - | - | - | - | - | - | - | - | 0.93±0.13 | <0.021 | -1.19±1.12 | 42.63±2.9 | >43.64 | 0.77±0.12 | 0.5±0.04 | | | | | |
| 173.15/-33.29 | 25.56±0.83 | <0.04 | 5.39±0.08 | 13.15±0.2 | 0.28±0.02 | >637.29 | 7.38±0.27 | 0.28±0.03 | 18.27±1.84 | <0.043 | 5.47±0.14 | 14.87±0.42 | >423.54 | 5.27±0.55 | 0.29±0.03 | | | | | |
| 173.15/-33.29 | - | <0.038 | 9.28±0.03 | 6.28±0.22 | 0.0±0.0 | >1472.01 | 6.83±0.89 | 0.28±0.03 | 44.53±4.93 | <0.038 | 7.23±0.12 | 8.18±0.31 | >1183.81 | 7.07±0.83 | 0.14±0.02 | | | | | |
| 173.15/-33.29 | 56.11±7.01 | - | - | - | - | - | - | - | 53.01±10.41 | <0.044 | 10.06±0.12 | 4.52±0.18 | >1202.46 | 4.65±0.93 | 0.55±0.04 | | | | | |
| 197.15/-0.85 | 24.77 | 0.61±0.08 | -0.66±0.06 | 1.77±0.18 | 0.24±0.56 | 54.25±0.74 | 1.27±0.37 | 5 | 9.8 | 0.61±0.01 | -0.68±0.01 | 2.0±0.02 | 21.47±1.9 | 0.51±0.05 | 1 | | | | | |
| 197.15/-0.85 | 76.55 | 0.8±0.19 | 6.66±1.98 | 13.01±1.39 | 0.0±0.05 | 139.01±2.74 | 28.24±7.32 | 0 | 69.42 | 1.25±0.0 | 8.75±0.01 | 13.53±0.03 | 97.3±4.55 | 31.95±1.5 | 0 | | | | | |
| 197.15/-0.85 | 23.36 | 1.12±0.29 | 9.13±0.19 | 1.0±0.0 | 34.67±4.22 | 3.11±1.46 | 3.11±1.46 | 1 | 25.19 | 0.71±0.01 | 17.74±0.01 | 1.83±0.02 | 49.55±3.63 | 1.26±0.1 | 2 | | | | | |
| 197.15/-0.85 | 19.07 | 0.44±0.25 | 13.47±0.53 | 3.38±1.26 | 0.0±0.0 | 53.56±6.32 | 1.54±1.66 | 4 | 20.43 | 0.51±0.01 | 21.16±0.03 | 4.73±0.08 | 51.15±6.76 | 2.39±0.32 | 3 | | | | | |
| 197.15/-0.85 | 39.71 | 0.86±0.15 | 17.61±0.15 | 2.28±0.4 | 0.0±0.0 | 68.84±3.22 | 2.62±0.66 | 2 | - | - | - | - | - | - | - | | | | | |
| 197.15/-0.85 | 31.12 | 0.57±0.1 | 21.0±0.43 | 4.72±1.06 | 0.0±0.0 | 71.63±3.24 | 3.71±1.05 | 6 | 30.03 | 0.26±0.0 | 27.37±0.13 | 12.3±0.18 | 131.18±10.44 | 8.19±0.67 | 4 | | | | | |
| 197.15/-0.85 | 40.38 | 0.26±0.03 | 26.75±1.48 | 13.15±1.6 | 0.0±0.0 | 176.39±8.48 | 11.9±2.15 | 6 | 1.1±0.07 | <0.025 | -67.79±0.57 | 20.7±1.53 | >43.77 | 0.44±0.04 | 1.0±0.0 | | | | | |
| 197.15/-0.85 | - | <0.025 | -67.74±0.6 | 22.52±2.2 | 0.69±0.45 | >149.92 | 0.73±0.15 | 1.0±0.0 | 1.83±0.06 | <0.013 | -24.65±1.44 | 31.02±2.79 | >138.59 | 1.1±0.1 | 0.8±0.04 | | | | | |
| 197.15/-0.85 | 1.66±0.06 | <0.016 | -67.68±1.16 | 26.8±2.25 | 0.0±0.0 | >105.35 | 0.86±0.08 | 0.5±0.01 | 15.33±1.84 | <0.051 | 6.39±0.33 | 4.12±1.07 | >78.77 | 0.33±0.13 | 0.31±0.04 | | | | | |
| 197.15/-0.85 | - | - | - | - | - | - | - | - | 4.05±1.25 | <0.101 | 15.7±0.25 | 27.99±0.78 | >426.92 | 23.39±3.2 | 0.42±0.04 | | | | | |
| 197.15/-0.85 | 26.5±3.61 | <0.116 | 14.94±0.27 | 29.62±1.4 | 0.0±0.0 | >228.57 | 15.23±2.19 | 0.32±0.01 | 43.09±5.77 | <0.066 | 19.61±0.25 | 10.78±0.59 | >731.21 | 10.17±1.1 | 0.19±0.03 | | | | | |
| 197.15/-0.85 | 66.02±3.13 | <0.076 | 18.05±0.16 | 13.07±0.46 | 0.13±0.08 | >870.17 | 17.78±1.24 | 0.33±0.01 | 48.61±4.52 | <0.074 | 28.36±0.26 | 4.4±0.66 | >92.72 | 0.59±0.12 | 0.34±0.03 | | | | | |
| 197.15/-0.85 | - | - | - | - | - | - | - | - | 6.9±1.02 | - | - | - | - | - | - | | | | | |

TABLE 3 (CONT)

| l/b ($^{\circ}$) | pseudo-Voigt | | | | | | | | | | Gaussian | | | | | | | | | |
|-----------------------|--------------|-------------------------|-------------------------------------|--------------------------------------|-----------|--------------|---|------------|--------------|-------------------------|-------------------------------------|--------------------------------------|--------------|---|------------|--|--|--|--|--|
| | T_B (K) | τ (10^{-2}) | V_{lsr} (km s^{-1}) | ΔV (km s^{-1}) | η | T_s (K) | N_{HI} (10^{20} cm^{-2}) | F or O | T_B (K) | τ (10^{-2}) | V_{lsr} (km s^{-1}) | ΔV (km s^{-1}) | T_s (K) | N_{HI} (10^{20} cm^{-2}) | F or O | | | | | |
| 202.29/11.53 | 2.94 | 0.12±0.01 | -3.11±0.09 | 1.82±0.22 | 0.0±0.0 | 25.96±2.29 | 0.11±0.02 | 1 | 3.16 | 0.12±0.0 | -3.12±0.02 | 1.81±0.05 | 27.96±2.41 | 0.12±0.01 | 1 | | | | | |
| 202.29/11.53 | 2.49 | 0.04±0.01 | 0.03±0.68 | 7.67±1.33 | 1.0±0.0 | 63.41±19.62 | 0.61±0.25 | 0 | 4.9 | 0.04±0.0 | -0.28±0.14 | 8.31±0.24 | 124.92±7.0 | 0.80±0.06 | 0 | | | | | |
| 202.29/11.53 | 1.13±0.3 | <0.015 | -18.05±7.71 | 32.09±10.49 | 0.92±0.54 | >77.18 | 1.01±0.46 | 0.5±0.29 | - | - | -28.29±5.77 | 28.03±7.93 | >33.59 | 0.28±0.1 | 0.5±0.29 | | | | | |
| 202.29/11.53 | 6.39±2.86 | <0.028 | -3.6±1.21 | 14.8±2.56 | 0.0±0.0 | >230.9 | 1.83±0.88 | 0.5±0.29 | - | - | -7.41±0.26 | 7.97±0.81 | >145.73 | 0.39±0.06 | 0.5±0.29 | | | | | |
| 202.29/11.53 | 3.59±0.64 | <0.024 | 3.84±0.14 | 4.28±0.84 | 1.0±0.0 | >147.57 | 0.44±0.12 | 0.5±0.29 | - | - | 4.1±0.15 | 3.93±0.38 | >84.68 | 0.19±0.02 | 0.5±0.29 | | | | | |
| 202.29/11.53 | 5.97±0.79 | <0.018 | 9.83±3.42 | 25.34±5.03 | 0.0±0.0 | >339.71 | 2.94±0.7 | 0.5±0.29 | - | - | 4.84±0.57 | 29.31±1.16 | >265.54 | 4.72±0.21 | 0.5±0.29 | | | | | |
| 202.29/11.53 | 2.95±0.18 | <0.015 | 36.55±0.61 | 19.29±0.98 | 0.83±0.13 | >201.65 | 1.54±0.14 | 1.0±0.0 | - | - | 36.32±0.5 | 22.38±0.82 | >157.31 | 1.16±0.06 | 1.0±0.0 | | | | | |
| 170.59/-36.24 | 17.43 | 0.55±0.02 | 1.01±0.09 | 2.64±0.15 | 0.0±0.0 | 41.2±1.37 | 1.71±0.13 | 3 | 7.3 | 0.16±0.01 | -0.59±0.31 | 4.63±0.36 | 49.36±15.1 | 0.71±0.23 | 3 | | | | | |
| 170.59/-36.24 | 25.89 | 0.57±0.09 | 4.1±0.19 | 2.32±0.34 | 0.0±0.0 | 59.58±1.51 | 1.53±0.33 | 3 | 15.62 | 0.41±0.02 | 1.03±0.02 | 1.8±0.06 | 46.45±1.63 | 0.67±0.05 | 1 | | | | | |
| 170.59/-36.24 | 42.14 | 2.08±0.49 | 7.98±0.09 | 3.67±0.23 | 0.0±0.0 | 48.16±0.88 | 7.14±1.75 | 2 | 26.98 | 0.7±0.01 | 4.19±0.04 | 2.96±0.1 | 53.59±2.79 | 2.14±0.14 | 4 | | | | | |
| 170.59/-36.24 | 32.82 | 2.08±0.17 | 10.85±0.13 | 1.19±0.49 | 0.0±0.0 | 37.51±0.84 | 1.81±0.64 | 4 | 56.84 | 2.15±0.02 | 7.88±0.02 | 3.2±0.06 | 64.33±0.98 | 8.59±0.23 | 2 | | | | | |
| 170.59/-36.24 | 30.79 | 1.74±0.11 | 12.6±0.27 | 3.95±0.31 | 0.0±0.0 | 37.34±2.91 | 4.99±0.76 | 0 | 23.02 | 2.08±0.08 | 10.81±0.01 | 1.18±0.04 | 26.31±1.4 | 1.25±0.09 | 5 | | | | | |
| 170.59/-36.24 | 24.33±0.62 | <0.048 | 4.39±0.06 | 14.53±0.14 | 0.16±0.01 | >503.85 | 7.38±0.21 | 0.7±0.03 | - | - | 3.72±0.07 | 17.99±0.21 | >299.59 | 4.95±0.22 | 0.28±0.01 | | | | | |
| 170.59/-36.24 | 110.8±5.7 | <0.045 | 11.13±0.13 | 3.31±0.24 | 0.0±0.0 | >2465.63 | 7.1±0.64 | 0.03±0.02 | - | - | 5.03±0.35 | 7.4±1.44 | >878.28 | 5.13±1.05 | 0.1±0.01 | | | | | |
| 203.42/15.42 | 3.91 | 0.05±0.01 | 1.37±0.22 | 1.91±0.66 | 0.21±0.06 | 80.1±5.33 | 0.15±0.09 | 0 | 2.19 | 0.05±0.0 | 1.35±0.05 | 1.99±0.11 | 44.93±12.16 | 0.08±0.02 | 0 | | | | | |
| 203.42/15.42 | - | - | - | - | - | - | - | - | 2.96±0.94 | <0.027 | -5.70±1.29 | 7.82±1.24 | >109.24 | 0.45±0.16 | 0.47±0.42 | | | | | |
| 203.42/15.42 | 11.88±0.48 | <0.027 | 1.25±0.05 | 12.49±0.35 | 0.73±0.08 | >445.99 | 3.87±0.22 | 0.5±0.43 | - | - | 0.21±0.21 | 4.33±0.73 | >165.63 | 0.37±0.19 | 0.48±0.4 | | | | | |
| 203.42/15.42 | 2.88±0.36 | <0.022 | 8.22±0.97 | 30.73±0.94 | 0.0±0.0 | >129.81 | 1.72±0.22 | 0.5±0.43 | - | - | 7.2±1.53 | 9.09±1.43 | >293.08 | 1.27±0.34 | 0.54±0.42 | | | | | |
| 207.31/1.15 | 17.35 | 0.11±0.02 | 6.81±0.98 | 10.04±1.83 | 0.0±0.0 | 166.53±3.51 | 3.57±0.9 | 3 | 4.54±0.32 | <0.027 | 5.58±0.4 | 27.47±1.51 | >170.13 | 0.55±0.22 | 0.55±0.43 | | | | | |
| 207.31/1.15 | 11.77 | 0.4±0.07 | 17.32±0.16 | 2.46±0.44 | 0.28±0.08 | 35.7±1.16 | 0.77±0.34 | 0 | 0.77±0.36 | <0.021 | 8.43±1.76 | 54.41±8.92 | >36.16 | 0.81±0.4 | 0.59±0.39 | | | | | |
| 207.31/1.15 | 30.91 | 0.44±0.03 | 23.26±0.41 | 7.67±0.93 | 0.0±0.0 | 86.84±1.1 | 5.66±0.8 | 4 | 14.54 | 0.14±0.0 | 6.66±0.06 | 7.89±0.14 | 111.3±18.8 | 2.35±0.4 | 0 | | | | | |
| 207.31/1.15 | 49.47 | 1.62±0.21 | 39.35±2.42 | 9.0±2.59 | 0.06±0.13 | 104.65±6.6 | 12.0±5.35 | 1 | 8.68 | 0.34±0.01 | 17.27±0.02 | 2.28±0.05 | 30.11±1.48 | 0.45±0.03 | 5 | | | | | |
| 207.31/1.15 | 36.58 | 1.32±0.43 | 43.09±0.21 | 4.11±1.04 | 0.0±0.0 | 49.92±4.67 | 5.25±2.23 | 2 | 29.71 | 0.41±0.0 | 22.97±0.04 | 9.22±0.1 | 88.33±1.08 | 6.52±0.11 | 1 | | | | | |
| 207.31/1.15 | 15.83 | 0.36±0.1 | 49.09±0.24 | 2.22±0.7 | 0.28±0.54 | 52.35±2.55 | 0.91±0.44 | 5 | 56.59 | 0.73±0.01 | 39.64±0.13 | 8.52±0.15 | 109.22±15.59 | 13.25±1.93 | 3 | | | | | |
| 207.31/1.15 | - | - | - | - | - | - | - | - | 39.32 | 1.36±0.03 | 43.35±0.01 | 3.58±0.06 | 52.9±3.7 | 5.01±0.38 | 4 | | | | | |
| 207.31/1.15 | - | - | - | - | - | - | - | - | 13.21 | 0.35±0.01 | 49.1±0.02 | 2.35±0.05 | 44.73±2.51 | 0.72±0.05 | 22 | | | | | |
| 207.31/1.15 | - | - | - | - | - | - | - | - | 4.57±0.56 | <0.046 | 0.66±0.43 | 6.02±0.56 | >99.41 | 0.53±0.08 | 0.5±0.02 | | | | | |
| 207.31/1.15 | 9.01±0.37 | <0.091 | 11.24±0.14 | 6.52±0.38 | 0.0±0.0 | >98.73 | 1.14±0.08 | 0.5±0.02 | - | - | 10.72±0.35 | 7.12±0.56 | >126.01 | 1.98±0.23 | 0.53±0.02 | | | | | |
| 207.31/1.15 | 45.45±0.42 | <0.08 | 26.06±0.18 | 34.97±0.2 | 0.0±0.0 | >564.64 | 30.84±0.33 | 0.0±0.0 | - | - | - | - | - | - | - | | | | | |
| 207.31/1.15 | 36.72±2.44 | <0.138 | 42.28±0.35 | 8.25±0.5 | 0.15±0.09 | >266.18 | 6.28±0.62 | 0.13±0.01 | - | - | 26.63±0.07 | 35.24±0.09 | >516.61 | 30.69±0.25 | 0.01±0.0 | | | | | |
| 207.31/1.15 | - | - | - | - | - | - | - | - | - | - | - | - | - | - | - | | | | | |
| 207.31/1.15 | - | - | - | - | - | - | - | - | 25.33±7.58 | <0.16 | 42.94±1.34 | 9.56±0.92 | >158.71 | 4.7±1.48 | 0.19±0.01 | | | | | |
| 189.21/-6.93 | - | - | - | - | - | - | - | - | 7.03 | 0.14±0.04 | -2.34±1.38 | 4.61±1.85 | 53.83±7.58 | 0.67±0.35 | 0 | | | | | |
| 189.21/-6.93 | - | - | - | - | - | - | - | - | 13.65 | 0.27±0.04 | 2.24±0.49 | 4.0±2.07 | 57.69±6.31 | 1.19±0.66 | 1 | | | | | |
| 189.21/-6.93 | 36.43 | 0.27±0.02 | 2.98±0.91 | 9.73±1.16 | 0.0±0.0 | 153.94±12.11 | 7.72±1.31 | 3 | - | - | - | - | - | - | - | | | | | |
| 189.21/-6.93 | 13.34 | 0.37±0.07 | 6.5±0.15 | 2.69±0.52 | 0.0±0.0 | 43.15±2.62 | 0.83±0.23 | 2 | 13.54 | 0.53±0.05 | 6.42±0.27 | 3.35±0.63 | 32.92±2.63 | 1.13±0.26 | 2 | | | | | |
| 189.21/-6.93 | 9.66 | 0.47±0.06 | 10.52±0.1 | 1.98±0.29 | 0.0±0.0 | 25.77±1.66 | 0.47±0.1 | 1 | 8.64 | 0.51±0.05 | 10.5±0.11 | 2.07±0.34 | 21.62±2.17 | 0.44±0.1 | 3 | | | | | |
| 189.21/-6.93 | 2.69 | 0.05±0.03 | 12.83±0.52 | 1.36±1.21 | 0.0±0.0 | 55.11±8.3 | 0.08±0.08 | 0 | 2.86 | 0.06±0.03 | 12.87±0.6 | 1.64±0.66 | 49.1±8.29 | 0.1±0.06 | 0 | | | | | |
| 189.21/-6.93 | 1.0 | 0.02±0.01 | 23.8±0.8 | 4.91±2.19 | 1.0±0.0 | 50.58±8.03 | 0.16±0.1 | 4 | 1.1 | 0.02±0.01 | 23.59±0.96 | 7.53±2.24 | 55.51±17.66 | 0.14±0.08 | 5 | | | | | |
| 189.21/-6.93 | - | - | - | - | - | - | - | - | 0.65±0.26 | <0.026 | -13.85±22.9 | 50.58±14.93 | >24.84 | 0.63±0.31 | 1.0±0.0 | | | | | |
| 189.21/-6.93 | 13.65±1.01 | <0.099 | -2.97±0.46 | 14.54±0.51 | 1.0±0.0 | >137.57 | 5.68±0.47 | 0.45±0.08 | - | - | - | - | - | - | - | | | | | |
| 189.21/-6.93 | - | - | - | - | - | - | - | - | 25.08±7.66 | <0.067 | 2.19±1.72 | 14.58±1.7 | >373.71 | 7.09±2.32 | 0.54±0.43 | | | | | |
| 189.21/-6.93 | - | - | - | - | - | - | - | - | 15.82±1.55 | <0.074 | 4.25±0.33 | 31.54±1.85 | >212.64 | 9.68±1.11 | 0.46±0.43 | | | | | |
| 189.21/-6.93 | 14.07±0.44 | <0.08 | 5.87±0.26 | 29.13±0.33 | 0.0±0.0 | >176.71 | 7.95±0.27 | 0.36±0.08 | - | - | - | - | - | - | - | | | | | |
| 189.21/-6.93 | - | - | - | - | - | - | - | - | 50.61±8.72 | <0.046 | 7.15±0.13 | 9.66±0.45 | >1104.92 | 9.48±1.69 | 0.58±0.27 | | | | | |
| 189.21/-6.93 | 49.22±1.64 | <0.06 | 7.73±0.18 | 9.51±0.18 | 0.0±0.0 | >818.81 | 9.08±0.35 | 0.27±0.05 | - | - | - | - | - | - | - | | | | | |

TABLE 3 (CONT)

| l/b ($^{\circ}$) | Pseudo-Voigt | | | | | | | | | | Gaussian | | | | | | | | | |
|-------------------------|--------------|-------------------------|--|--------------------------------------|-----------|--------------|--|-------------------|--------------|-------------------------|--|--------------------------------------|--------------|--|-------------------|--|--|--|--|--|
| | T_B (K) | τ (10^{-2}) | V_{par} (km s^{-1}) | ΔV (km s^{-1}) | η | T_s (K) | NH (10^{20} cm^{-2}) | $F_{\text{or O}}$ | T_B (K) | τ (10^{-2}) | V_{par} (km s^{-1}) | ΔV (km s^{-1}) | T_s (K) | NH (10^{20} cm^{-2}) | $F_{\text{or O}}$ | | | | | |
| 207.31/12.37 | 5.04 | 0.04±0.01 | -0.84±0.62 | 5.19±1.42 | 0.0±0.0 | 128.59±39.6 | 0.54±0.26 | 0 | 5.05 | 0.04±0.01 | -0.81±0.18 | 5.43±0.45 | 128.67±5.07 | 0.55±0.06 | 1 | | | | | |
| 207.31/12.37 | - | - | - | - | - | - | - | - | 10.6 | 0.1±0.01 | 6.5±0.59 | 4.29±0.81 | 111.35±2.81 | 0.95±0.22 | 0 | | | | | |
| 207.31/12.37 | 11.37 | 0.12±0.02 | 7.02±0.33 | 4.72±0.65 | 0.0±0.0 | 100.52±22.82 | 1.1±0.34 | 1 | 5.37 | 0.06±0.02 | 8.89±0.25 | 2.6±0.64 | 92.25±1.74 | 0.26±0.12 | 2 | | | | | |
| 207.31/12.37 | - | - | - | - | - | - | - | - | 0.89 | 0.04±0.0 | 21.04±0.08 | 2.13±0.19 | 22.75±1.75 | 0.04±0.01 | 3 | | | | | |
| 207.31/12.37 | 6.88±1.13 | <0.031 | -4.04±1.18 | 12.18±1.28 | 0.87±0.19 | >221.52 | 2.3±0.47 | 0.99±0.08 | - | - | - | - | - | - | - | | | | | |
| 207.31/12.37 | - | - | - | - | - | - | - | - | 4.55±0.12 | <0.032 | -3.49±0.24 | 10.95±0.28 | >142.11 | 0.97±0.04 | 0.5±0.17 | | | | | |
| 207.31/12.37 | 4.31±2.05 | <0.031 | 2.22±0.31 | 4.07±0.77 | 0.0±0.0 | >138.54 | 0.34±0.17 | 0.49±0.06 | 4.16±0.18 | <0.031 | 2.26±0.03 | 3.82±0.06 | >133.77 | 0.31±0.01 | 0.52±0.16 | | | | | |
| 207.31/12.37 | 7.86±1.23 | <0.055 | 10.09±2.02 | 12.79±3.45 | 0.44±0.61 | >142.04 | 2.36±0.93 | 0.13±0.25 | - | - | - | - | - | - | - | | | | | |
| 207.31/12.37 | - | - | - | - | - | - | - | - | 4.68±0.05 | <0.039 | 11.03±0.17 | 8.87±0.43 | >119.75 | 0.81±0.04 | 0.52±0.17 | | | | | |
| 207.31/12.37 | - | - | - | - | - | - | - | - | 5.18±0.03 | <0.023 | 14.44±0.07 | 4.32±0.14 | >225.24 | 4.35±0.03 | 0.5±0.17 | | | | | |
| 207.31/12.37 | - | - | - | - | - | - | - | - | 4.55±0.05 | <0.045 | 20.16±0.04 | 5.38±0.08 | >100.44 | 0.48±0.01 | 0.49±0.17 | | | | | |
| 207.31/12.37 | 6.36±0.69 | <0.055 | 20.35±0.1 | 5.74±0.61 | 1.0±0.0 | >115.84 | 1.05±0.16 | 1.0±0.0 | - | - | - | - | - | - | - | | | | | |
| 207.31/12.37 | 2.6±0.44 | <0.021 | 28.98±2.45 | 27.8±4.29 | 0.0±0.0 | >121.88 | 1.4±0.32 | 0.38±0.44 | - | - | - | - | - | - | - | | | | | |
| 207.31/12.37 | 0.48±0.07 | <0.022 | 58.55±1.49 | 16.43±2.83 | 0.0±0.0 | >21.25 | 0.15±0.03 | 1.0±0.0 | - | - | - | - | - | - | - | | | | | |
| 207.31/12.37 | - | - | - | - | - | - | - | - | 0.36±0.01 | <0.024 | 59.53±0.22 | 13.81±0.55 | >15.22 | 0.1±0.0 | 1.0±0.0 | | | | | |
| 175.7/-18.36 | 15.16 | 0.27±0.04 | 2.45±0.21 | 2.49±0.44 | 1.0±0.0 | 64.05±5.04 | 1.23±0.3 | 3 | 6.09 | 0.24±0.0 | 2.43±0.02 | 2.75±0.05 | 28.52±4.52 | 0.37±0.06 | 0 | | | | | |
| 175.7/-18.36 | 35.91 | 1.04±0.11 | 8.42±0.3 | 5.18±0.36 | 0.0±0.0 | 56.81±1.37 | 0.69±0.78 | 1 | 48.73 | 1.01±0.01 | 8.45±0.04 | 5.4±0.05 | 78.6±1.52 | 8.1±0.21 | 3 | | | | | |
| 175.7/-18.36 | 17.85 | 0.62±0.16 | 9.47±0.15 | 1.59±0.4 | 0.0±0.0 | 38.64±2.85 | 0.74±0.27 | 0 | 20.87 | 0.6±0.02 | 9.47±0.02 | 1.61±0.05 | 46.26±1.44 | 0.87±0.05 | 2 | | | | | |
| 175.7/-18.36 | 24.17 | 0.51±0.11 | 11.87±0.18 | 2.09±0.45 | 0.0±0.0 | 60.49±1.09 | 1.25±0.38 | 2 | 17.98 | 0.48±0.02 | 11.89±0.02 | 1.98±0.06 | 47.16±2.72 | 0.86±0.06 | 1 | | | | | |
| 175.7/-18.36 | 3.64±0.08 | <0.025 | -20.07±0.64 | 33.25±1.01 | 0.0±0.0 | >143.27 | 2.35±0.09 | 0.5±0.08 | - | - | - | - | - | - | - | | | | | |
| 175.7/-18.36 | 26.38±1.48 | <0.062 | 0.97±0.23 | 8.92±0.18 | 0.97±0.07 | >424.56 | 6.66±0.43 | 0.24±0.08 | 5.03±0.07 | <0.023 | -13.9±0.45 | 39.71±0.61 | >217.83 | 3.88±0.08 | 0.51±0.17 | | | | | |
| 175.7/-18.36 | - | - | - | - | - | - | - | - | 23.87±1.39 | <0.072 | 2.81±0.08 | 6.5±0.33 | >329.68 | 3.01±0.23 | 0.41±0.16 | | | | | |
| 175.7/-18.36 | 52.43±1.65 | <0.055 | 7.5±0.14 | 9.02±0.2 | 0.0±0.0 | >95.6 | 9.17±0.36 | 0.16±0.05 | 26.04±1.8 | <0.068 | 4.21±0.07 | 14.66±0.31 | >380.23 | 7.4±0.54 | 0.31±0.15 | | | | | |
| 203.54/-0.27 | 2.67 | 0.07±0.04 | -3.61±0.57 | 2.35±1.35 | 0.12±1.29 | 39.45±5.57 | 0.14±0.14 | 0 | 13.28±1.36 | <0.068 | 11.87±0.1 | 3.84±0.22 | >194.24 | 0.99±0.12 | 0.45±0.16 | | | | | |
| 203.54/-0.27 | 20.42 | 0.39±0.04 | 5.41±0.33 | 5.2±0.63 | 0.0±0.0 | 5.22±1.55 | 2.46±0.18 | 5 | 3.17 | 0.07±0.0 | -3.57±0.05 | 2.35±0.12 | 46.84±5.47 | 0.16±0.02 | 1 | | | | | |
| 203.54/-0.27 | 6.5 | 0.3±0.06 | 10.84±0.35 | 3.24±0.86 | 0.0±0.0 | 25.06±116.04 | 0.47±2.18 | 3 | 26.51 | 0.38±0.0 | 5.56±0.03 | 5.69±0.06 | 83.85±1.77 | 3.55±0.09 | 1 | | | | | |
| 203.54/-0.27 | 39.67 | 0.96±0.21 | 16.58±0.31 | 2.99±0.51 | 0.0±0.0 | 64.29±1.38 | 3.58±1.01 | 4 | 17.14 | 0.3±0.0 | 11.03±0.02 | 2.89±0.05 | 66.12±1.6 | 1.12±0.37 | 2 | | | | | |
| 203.54/-0.27 | 77.81 | 1.76±0.17 | 21.74±0.3 | 5.93±0.88 | 0.07±0.15 | 93.98±0.9 | 19.72±3.72 | 1 | 50.0 | 1.07±0.01 | 16.72±0.02 | 3.29±0.04 | 76.1±1.35 | 5.18±0.13 | 3 | | | | | |
| 203.54/-0.27 | - | - | - | - | - | - | - | - | 28.55 | 1.85±0.01 | 21.92±0.02 | 5.43±0.07 | 33.88±9.64 | 6.61±1.89 | 5 | | | | | |
| 203.54/-0.27 | 72.06 | 1.12±0.14 | 30.79±0.3 | 6.78±0.66 | 0.0±0.0 | 106.96±0.82 | 15.75±2.46 | 2 | 34.94 | 0.77±0.01 | 27.6±0.02 | 2.89±0.02 | 65.07±6.38 | 2.8±0.29 | 6 | | | | | |
| 203.54/-0.27 | 47.66 | 4.31±3.48 | 31.08±0.1 | 1.28±0.32 | 0.0±0.0 | 48.31±2.67 | 5.18±4.4 | 6 | 49.03 | 3.41±0.06 | 30.98±0.01 | 2.03±0.02 | 50.71±4.78 | 6.8±0.66 | 7 | | | | | |
| 203.54/-0.27 | - | - | - | - | - | - | - | - | 18.92 | 0.66±0.01 | 33.78±0.05 | 3.5±0.07 | 39.15±6.55 | 1.77±0.0 | 4 | | | | | |
| 203.54/-0.27 | 3.31 | 0.11±0.03 | 41.78±0.49 | 3.59±1.1 | 0.0±0.0 | 31.76±3.39 | 0.25±0.11 | 7 | 2.63 | 0.11±0.0 | 41.52±0.05 | 4.33±0.11 | 25.25±6.08 | 0.24±0.06 | 8 | | | | | |
| 203.54/-0.27 | 14.19±28.63 | <0.139 | 9.75±2.74 | 3.44±1.98 | 0.0±0.0 | >102.3 | 0.95±1.98 | 0.47±0.02 | 9.85±2.57 | <0.121 | 9.3±0.81 | 3.74±1.09 | >81.71 | 0.71±0.28 | 0.5±0.02 | | | | | |
| 203.54/-0.27 | 47.12±1.05 | <0.144 | 10.83±0.31 | 22.87±0.3 | 0.08±0.01 | >327.08 | 21.69±0.57 | 0.12±0.01 | - | - | - | - | - | - | - | | | | | |
| 203.54/-0.27 | - | - | - | - | - | - | - | - | 106.05±14.1 | <0.154 | 11.58±0.53 | 24.14±0.39 | >307.89 | 22.17±1.0 | 0.0±0.0 | | | | | |
| 203.54/-0.27 | - | - | - | - | - | - | - | - | 41.83±4.79 | <0.211 | 30.78±0.28 | 7.96±0.61 | >262.22 | 12.02±1.62 | 0.5±0.0 | | | | | |
| 203.54/-0.27 | - | - | - | - | - | - | - | - | 35.92±5.02 | <0.115 | 33.08±1.34 | 21.51±0.85 | >312.05 | 6.46±0.89 | 1.0±0.0 | | | | | |
| 203.54/-0.27 | 38.94±1.19 | <0.129 | 31.7±0.43 | 22.47±0.36 | 0.0±0.0 | >301.57 | 16.98±0.59 | 0.29±0.01 | - | - | - | - | - | - | - | | | | | |
| 203.54/-0.27 | - | - | - | - | - | - | - | - | 14.9 | 0.19±0.0 | -7.08±0.04 | 2.85±0.09 | 86.1±2.55 | 0.92±0.05 | 0 | | | | | |
| 203.54/-0.27 | 6.66 | 0.05±0.01 | -10.53±1.8 | 13.49±3.51 | 0.0±0.0 | 136.46±16.66 | 1.66±0.67 | 3 | 7.63 | 0.12±0.0 | 0.86±0.16 | 4.53±0.37 | 67.45±6.98 | 0.73±0.1 | 1 | | | | | |
| 164.76/-10.24 | 9.59 | 0.15±0.05 | -7.04±0.29 | 1.94±0.69 | 0.0±0.0 | 68.82±7.35 | 0.38±0.19 | 2 | 14.9 | 0.19±0.0 | -0.86±0.16 | 4.53±0.37 | 67.45±6.98 | 0.73±0.1 | 1 | | | | | |
| 164.76/-10.24 | - | - | - | - | - | - | - | - | 7.63 | 0.12±0.0 | 0.86±0.16 | 4.53±0.37 | 67.45±6.98 | 0.73±0.1 | 1 | | | | | |
| 164.76/-10.24 | 32.3 | 0.94±0.06 | 4.05±0.09 | 3.29±0.34 | 0.97±0.24 | 53.01±0.52 | 4.65±0.68 | 1 | 21.64 | 0.86±0.01 | 4.06±0.02 | 3.72±0.03 | 37.51±1.55 | 2.33±0.1 | 2 | | | | | |
| 164.76/-10.24 | 28.11 | 0.74±0.05 | 10.05±0.27 | 2.8±0.17 | 0.0±0.0 | 53.75±0.49 | 2.17±0.19 | 1 | 16.93 | 0.77±0.01 | 9.93±0.01 | 3.18±0.05 | 31.53±4.62 | 1.49±0.22 | 3 | | | | | |
| 164.76/-10.24 | 2.65±0.16 | <0.026 | -59.89±0.79 | 32.2±1.38 | 0.0±0.0 | >102.06 | 1.65±0.28 | 1.0±0.0 | 2.58±0.04 | <0.026 | -69.93±0.46 | 31.54±0.97 | >99.59 | 1.58±0.05 | 1.0±0.0 | | | | | |
| 164.76/-10.24 | 4.55±0.15 | <0.042 | -22.08±1.22 | 29.81±2.95 | 0.0±0.0 | >108.74 | 2.62±0.27 | 0.5±0.08 | 6.92±0.13 | <0.065 | -13.63±0.48 | 37.8±0.7 | >106.04 | 5.07±0.17 | 0.47±0.4 | | | | | |
| 164.76/-10.24 | 16.7±0.67 | <0.11 | -7.41±0.07 | 6.29±0.52 | 1.0±0.0 | >151.21 | 3.01±0.27 | 0.5±0.08 | 11.97±0.39 | <0.011 | -7.74±0.32 | 11.46±0.36 | >107.21 | 2.66±0.41 | 0.38±0.41 | | | | | |
| 164.76/-10.24 | 38.42±0.48 | <0.07 | 4.73±0.04 | 11.48±0.09 | 0.0±0.0 | >546.16 | 8.56±0.13 | 0.24±0.05 | 33.37±1.38 | <0.069 | 5.09±0.18 | 9.93±0.44 | >107.11 | 6.43±0.39 | 0.39±0.36 | | | | | |
| 164.76/-10.24 | - | - | - | - | - | - | - | - | 8.43±2.58 | <0.06 | 10.82±0.47 | 5.1±0.44 | >139.57 | 0.83±0.27 | 0.47±0.4 | | | | | |
| 206.09/13.67 | 4.77 | 0.06±0.02 | 0.27±0.43 | 3.4±1.45 | 0.6±0.91 | 81.87±8.96 | 0.39±0.25 | 0 | 3.31 | 0.05±0.0 | 0.15±0.12 | 3.79±0.38 | 67.81±4.1 | 0.26±0.03 | 0 | | | | | |
| 206.09/13.67 | 5.33±1.28 | <0.036 | -3.29±0.38 | 13.3±1.16 | 1.0±0.0 | >148.94 | 2.03±0.52 | 0.5±0.42 | 7.96±0.32 | <0.032 | 2.11±0.32 | 16.52±0.66 | >248.99 | 2.55±0.15 | 0.5±0.42 | | | | | |
| 206.09/13.67 | - | - | - | - | - | - | - | - | 2.19±0.31 | <0.035 | 11.39±1.86 | 48.79±4.32 | >63.4 | 2.08±0.35 | 0.5±0.42 | | | | | |
| 206.09/13.67 | 5.91±1.68 | <0.037 | 4.4±0.47 | 12.1±2.56 | 0.26±0.55 | >158.25 | 1.56±0.66 | 0.5±0.42 | - | - | - | - | - | - | - | | | | | |
| 206.09/13.67 | 6.5±0.85 | <0.034 | 16.71±1.17 | 17.85±1.72 | 0.0±0.0 | >190.69 | 2.25±0.37 | 0.5±0.42 | 4.75±0.26 | <0.032 | 17.75±0.45 | 15.36±0.87 | >150.15 | 1.41±0.11 | 0.5±0.42 | | | | | |
| 206.09/13.67 | 0.86±0.07 | <0.019 | 39.53±2.82 | 30.55±4.35 | 0.0±0.0 | >45.65 | 0.51±0.08 | 1.0±0.0 | - | - | - | - | - | - | - | | | | | |
| 206.09/13.67 | - | - | - | - | - | - | - | - | 0.3±0.13 | <0.015 | 49.45±2.26 | 17.63±6.32 | >20.24 | 0.1±0.06 | 1.0±0.0 | | | | | |

TABLE 3 (CONT)

| <i>l/b</i> ($^{\circ}$) | pseudo-Voigt | | | | | | | | | | Gaussian | | | | | <i>F</i> <i>err</i> <i>O</i> | <i>N</i> HI (10^{20} cm^{-2}) | <i>F</i> <i>err</i> <i>O</i> |
|------------------------------|------------------------------|-------------------------|---|--------------------------------------|-----------|------------------------------|--|------------------------------|------------------------------|-------------------------|---|--------------------------------------|------------------------------|--|------------------------------|------------------------------|--|------------------------------|
| | <i>T</i> _B (K) | τ (10^{-2}) | <i>V</i> _{lsr} (km s^{-1}) | ΔV (km s^{-1}) | η | <i>T</i> _s (K) | <i>N</i> HI (10^{20} cm^{-2}) | <i>F</i> <i>err</i> <i>O</i> | <i>T</i> _B (K) | τ (10^{-2}) | <i>V</i> _{lsr} (km s^{-1}) | ΔV (km s^{-1}) | <i>T</i> _s (K) | <i>N</i> HI (10^{20} cm^{-2}) | <i>F</i> <i>err</i> <i>O</i> | | | |
| 171.98/-35.48 | 13.89 | 0.23±0.03 | -3.5±0.53 | 4.32±0.9 | 0.0±0.0 | 67.58±2.24 | 1.29±0.33 | 2 | 7.75 | 0.26±0.01 | -3.51±0.11 | 4.76±0.17 | 33.85±2.56 | 0.82±0.07 | 5 | | | |
| 171.98/-35.48 | 16.26 | 0.56±0.06 | 1.44±0.28 | 3.93±0.91 | 0.64±0.34 | 37.92±3.92 | 2.1±0.63 | 1 | 14.69 | 0.56±0.01 | 1.73±0.04 | 4.36±0.18 | 34.26±2.37 | 1.64±0.13 | 1 | | | |
| 171.98/-35.48 | 6.9 | 0.3±0.12 | 6.69±0.2 | 1.06±0.51 | 0.0±0.0 | 26.61±2.14 | 0.16±0.1 | 3 | 15.42 | 0.33±0.03 | 4.91±0.08 | 1.75±0.19 | 54.86±3.61 | 0.61±0.09 | 2 | | | |
| 171.98/-35.48 | 14.43 | 0.65±0.07 | 7.57±0.34 | 5.88±1.18 | 0.0±0.0 | 30.19±3.95 | 2.22±0.58 | 4 | 18.32 | 0.61±0.12 | 6.56±0.04 | 1.44±0.14 | 40.11±1.23 | 0.68±0.15 | 3 | | | |
| 171.98/-35.48 | - | - | - | - | - | - | - | - | 30.67 | 0.61±0.04 | 8.11±0.15 | 2.91±0.46 | 67.17±1.45 | 2.31±0.41 | 0 | | | |
| 171.98/-35.48 | 7.65 | 0.15±0.1 | 11.97±0.36 | 2.23±1.04 | 0.08±0.69 | 54.89±3.85 | 0.38±0.32 | 0 | 24.18 | 0.33±0.03 | 11.21±0.21 | 3.46±0.23 | 86.01±1.57 | 1.93±0.2 | 4 | | | |
| 171.98/-35.48 | 38.58±2.06 | <0.1 | -0.03±0.12 | 4.82±0.1 | 1.0±0.0 | >385.88 | 5.32±0.31 | 0.0±0.0 | 1.26±0.08 | <0.025 | -15.71±0.26 | 7.58±0.66 | >50.31 | 0.19±0.02 | 1 | | | |
| 171.98/-35.48 | 81.76±3.18 | <0.081 | 7.45±0.04 | 8.7±0.12 | 0.09±0.01 | >1014.14 | 14.39±0.6 | 0.0±0.0 | 62.59±1.64 | <0.074 | 4.49±0.05 | 13.27±0.08 | >851.41 | 16.11±0.43 | 0 | | | |
| 203.64/13.91 | 6.57 | 0.1±0.03 | -2.36±0.89 | 5.2±1.75 | 0.28±0.55 | 69.03±19.65 | 0.79±0.44 | 0 | 21.59 | 0.15±0.0 | 0.11±0.08 | 9.4±0.16 | 154.98±5.59 | 4.18±0.19 | 1 | | | |
| 203.64/13.91 | 16.06 | 0.22±0.04 | 2.06±0.35 | 3.47±0.7 | 1.0±0.0 | 81.34±3.82 | 1.8±0.49 | 1 | 6.78 | 0.13±0.01 | 2.03±0.03 | 1.51±0.09 | 55.6±2.67 | 0.21±0.02 | 0 | | | |
| 203.64/13.91 | 10.59±2.34 | <0.062 | -2.1±0.26 | 9.75±0.76 | 0.49±0.23 | >170.95 | 2.48±0.62 | 0.49±0.29 | 4.05±0.31 | <0.037 | -6.37±1.0 | 15.09±1.14 | >109.46 | 1.18±0.13 | 0 | | | |
| 203.64/13.91 | 6.25±1.02 | <0.077 | -0.63±0.16 | 3.39±0.88 | 1.0±0.0 | >80.91 | 0.61±0.19 | 0.5±0.29 | - | - | - | - | - | - | 0 | | | |
| 203.64/13.91 | 3.13±0.55 | <0.061 | 8.71±2.05 | 30.82±2.08 | 0.0±0.0 | >51.66 | 1.87±0.35 | 0.5±0.29 | - | - | - | - | - | - | 0 | | | |
| 203.64/13.91 | 1.58±0.43 | 0.03 | 14.82±1.04 | 21.07±3.73 | 1.0±0.0 | >53.27 | 0.95±0.31 | 0.5±0.29 | - | - | - | - | - | - | 0 | | | |
| 176.27/-28.26 | 19.0 | 0.13±0.03 | -0.59±0.25 | 3.57±0.54 | 0.0±0.0 | 155.87±2.31 | 1.45±0.35 | 0 | 2.85 | 0.14±0.0 | -0.55±0.03 | 3.77±0.07 | >144.56 | 2.03±0.06 | 0 | | | |
| 176.27/-28.26 | 36.67 | 0.72±0.16 | 6.68±0.12 | 1.39±0.26 | 0.0±0.0 | 71.45±0.64 | 1.38±0.4 | 1 | 31.48 | 1.05±0.02 | 6.82±0.02 | 1.68±0.03 | 48.42±0.74 | 1.65±0.05 | 2 | | | |
| 176.27/-28.26 | 69.19 | 1.45±0.09 | 8.75±0.14 | 3.61±0.21 | 0.09±0.05 | 90.39±0.32 | 9.59±0.84 | 2 | 48.65 | 1.16±0.03 | 8.99±0.02 | 2.31±0.05 | 70.86±0.5 | 3.68±0.12 | 3 | | | |
| 176.27/-28.26 | 2.24±0.05 | <0.022 | -21.57±0.23 | 19.9±0.69 | 0.55±0.13 | >100.76 | 1.09±0.07 | 0.5±0.3 | 33.91 | 0.4±0.02 | 9.3±0.05 | 4.97±0.09 | 102.85±1.65 | 3.96±0.27 | 1 | | | |
| 176.27/-28.26 | 176.27/-28.26 | - | - | - | - | - | - | - | 2.13±0.04 | <0.023 | -20.73±0.26 | 22.15±0.67 | >91.5 | 0.91±0.03 | 0 | | | |
| 176.27/-28.26 | 34.53±0.17 | <0.043 | 4.78±0.03 | 13.03±0.05 | 0.01±0.01 | >806.55 | 8.76±0.07 | 0.32±0.26 | 16.73±8.62 | <0.087 | -0.87±0.18 | 4.13±0.19 | >192.41 | 1.34±0.69 | 0 | | | |
| 190.16/3.91 | 0.85 | 0.03±0.01 | -72.64±0.77 | 5.24±1.67 | 0.0±0.0 | 28.76±6.38 | 0.1±0.05 | 0 | 34.03±0.22 | <0.043 | 4.82±0.05 | 12.7±0.06 | >795.04 | 8.38±0.07 | 0 | | | |
| 190.16/3.91 | 17.98 | 0.3±0.03 | -8.63±0.39 | 5.22±0.89 | 0.0±0.0 | 69.36±5.44 | 2.09±0.45 | 3 | 0.37 | 0.03±0.0 | -72.66±0.21 | 5.29±0.49 | 19.12±1.22 | 0.06±0.01 | 0 | | | |
| 190.16/3.91 | 77.53 | 1.79±0.14 | -1.16±0.14 | 4.83±0.4 | 0.0±0.0 | 93.07±0.4 | 15.65±1.8 | 1 | 12.66 | 0.3±0.0 | -8.68±0.04 | 5.19±0.09 | 48.85±2.14 | 1.46±0.07 | 1 | | | |
| 190.16/3.91 | 56.2 | 0.99±0.09 | 3.98±0.16 | 2.67±0.4 | 0.0±0.0 | 89.43±1.11 | 4.61±0.81 | 2 | 50.93 | 1.8±0.01 | -1.15±0.01 | 4.86±0.04 | 61.02±0.16 | 10.32±0.12 | 2 | | | |
| 190.16/3.91 | 56.82 | 1.16±0.09 | 9.16±0.14 | 4.2±0.35 | 0.0±0.0 | 82.77±7.03 | 7.81±1.13 | 4 | 31.24 | 0.91±0.01 | 3.81±0.02 | 2.37±0.04 | 52.28±0.13 | 2.19±0.05 | 3 | | | |
| 190.16/3.91 | 5.0 | 0.19±0.05 | 20.37±0.33 | 3.05±0.69 | 0.0±0.0 | 28.9±7.87 | 0.33±0.15 | 5 | 34.79 | 0.7±0.02 | 8.9±0.03 | 6.04±0.1 | 69.11±0.41 | 5.67±0.16 | 5 | | | |
| 190.16/3.91 | 2.08±0.17 | <0.043 | -73.69±0.23 | 17.65±1.49 | 0.75±0.16 | >48.61 | 0.96±0.13 | 0 | 22.49 | 0.73±0.02 | 9.24±0.02 | 1.86±0.05 | 43.41±0.46 | 1.14±0.05 | 6 | | | |
| 190.16/3.91 | 13.63±1.96 | <0.116 | -6.23±0.19 | 4.65±0.68 | 0.46±0.37 | >117.55 | 1.5±0.38 | 0.55±0.09 | 4.69 | 0.2±0.0 | 20.29±0.03 | 2.92±0.06 | 25.9±0.41 | 0.29±0.01 | 6 | | | |
| 190.16/3.91 | 88.35±1.87 | <0.151 | 6.55±0.14 | 22.57±0.16 | 0.13±0.01 | >585.63 | 41.1±0.93 | 0.14±0.05 | - | - | - | - | - | - | 0 | | | |
| 190.16/3.91 | 35.76±7.11 | <0.136 | 8.42±0.15 | 3.91±0.2 | 0.29±0.24 | >262.0 | 3.09±0.7 | 0.63±0.08 | 13.64±0.16 | <0.132 | 7.84±0.02 | 3.97±0.02 | >103.04 | 1.09±0.01 | 0 | | | |
| 190.16/3.91 | 10.97±1.02 | <0.134 | 18.82±0.22 | 5.25±0.31 | 0.0±0.0 | >81.93 | 1.12±0.12 | 0.43±0.09 | 10.22±0.06 | <0.135 | 18.14±0.01 | 5.65±0.03 | >75.56 | 1.12±0.01 | 0 | | | |
| 205.41/-4.43 | 53.13 | 0.65±0.05 | 5.81±0.21 | 5.5±0.41 | 0.0±0.0 | 111.16±1.3 | 7.75±0.84 | 0 | 51.67 | 0.66±0.0 | 5.82±0.02 | 5.5±0.04 | 106.94±1.36 | 7.48±0.12 | 0 | | | |
| 205.41/-4.43 | 30.69 | 0.74±0.09 | 12.27±0.16 | 3.43±0.34 | 0.0±0.0 | 58.7±1.16 | 2.88±0.45 | 1 | 36.12 | 0.72±0.01 | 12.3±0.01 | 3.5±0.03 | 70.37±1.19 | 3.46±0.07 | 0 | | | |
| 205.41/-4.43 | 9.15 | 0.19±0.05 | 22.58±0.29 | 2.49±1.12 | 0.94±0.93 | 52.87±3.18 | 0.71±0.43 | 2 | 6.8 | 0.16±0.0 | 22.42±0.03 | 2.25±0.08 | 46.02±2.72 | 0.32±0.02 | 5 | | | |
| 205.41/-4.43 | 25.06 | 0.31±0.07 | 32.43±0.34 | 4.25±1.16 | 1.0±0.0 | 94.02±2.88 | 3.59±1.24 | 3 | 10.43 | 0.26±0.01 | 32.48±0.02 | 1.85±0.05 | 45.54±8.31 | 0.42±0.08 | 4 | | | |
| 205.41/-4.43 | 10.94 | 0.15±0.02 | 41.61±0.57 | 8.06±1.29 | 0.0±0.0 | 78.56±6.38 | 1.86±0.43 | 4 | 25.44 | 0.15±0.0 | 34.79±0.12 | 18.4±0.26 | 182.61±2.01 | 9.56±0.22 | 2 | | | |
| 205.41/-4.43 | - | - | - | - | - | - | - | - | 9.07 | 0.15±0.0 | 42.11±0.03 | 2.31±0.09 | 65.09±2.69 | 0.44±0.03 | 3 | | | |
| 205.41/-4.43 | 66.54±0.57 | <0.114 | 9.7±0.05 | 11.98±0.07 | 0.5±0.01 | >585.02 | 19.13±0.22 | 0.51±0.4 | 55.31±0.65 | <0.1 | 8.91±0.04 | 10.35±0.06 | >532.23 | 1.11±0.15 | 0.49±0.08 | | | |
| 205.41/-4.43 | 25.97±1.84 | <0.17 | 29.79±0.49 | 15.38±0.53 | 0.0±0.0 | >152.57 | 7.75±0.61 | 0.51±0.42 | 18.58±0.26 | <0.099 | 23.69±0.08 | 40.99±0.18 | >186.82 | 14.77±0.22 | 0.43±0.08 | | | |
| 205.41/-4.43 | - | - | - | - | - | - | - | - | 18.22±1.78 | <0.177 | 32.03±0.07 | 3.59±0.19 | >102.7 | 1.27±0.14 | 0.43±0.08 | | | |
| 205.41/-4.43 | 12.78±1.65 | <0.086 | 43.56±1.4 | 18.04±1.13 | 0.0±0.0 | >147.85 | 4.47±0.64 | 0.5±0.42 | - | - | - | - | - | - | - | | | |

TABLE 3 (CONT)

| l/b | pseudo-Voigt | | | | | | | | | | Gaussian | | | | | | | | | |
|---------------|--------------|-------------------------|-------------------------------------|--------------------------------------|-----------|--------------|---|----------------|--------------|-------------------------|-------------------------------------|--------------------------------------|--------------|---|----------------|--|--|--|--|--|
| | T_B (K) | τ (10^{-2}) | V_{str} (km s^{-1}) | ΔV (km s^{-1}) | η | T_s (K) | N_{HI} (10^{20} cm^{-2}) | $F_{\sigma O}$ | T_B (K) | τ (10^{-2}) | V_{str} (km s^{-1}) | ΔV (km s^{-1}) | T_s | N_{HI} (10^{20} cm^{-2}) | $F_{\sigma O}$ | | | | | |
| 199.52/6.04 | 8.29 | 0.25±0.08 | 0.24±0.19 | 2.35±0.73 | 0.63±0.51 | 37.48±2.73 | 0.56±0.27 | 0 | 6.41 | 0.25±0.0 | 0.45±0.02 | 2.59±0.05 | 28.99±2.17 | 0.36±0.03 | 0 | | | | | |
| 199.52/6.04 | 15.73 | 0.38±0.05 | 0.38±0.39 | 3.07±0.60 | 0.0±0.0 | 49.77±2.39 | 1.12±0.29 | 1 | 23.44 | 0.33±0.01 | 8.43±0.07 | 3.41±1.12 | 1.93±0.08 | 1 | 1.93±0.08 | | | | | |
| 199.52/6.04 | 17.67 | 0.53±0.06 | 1.81±0.25 | 2.57±0.44 | 0.06±0.27 | 42.96±1.55 | 1.16±0.28 | 1 | 21.16 | 0.5±0.0 | 11.42±0.04 | 2.49±0.06 | 5.3±0.11 | 2 | 1.3±0.0 | | | | | |
| 199.52/6.04 | 9.72 | 0.49±0.13 | 32.32±0.23 | 2.15±0.46 | 1.0±0.0 | 25.1±2.29 | 0.76±0.27 | 3 | 15.27 | 0.61±0.01 | 32.54±0.01 | 1.86±0.02 | 33.43±1.63 | 0.73±0.04 | 3 | | | | | |
| 199.52/6.04 | 0.88±0.04 | <0.033 | -66.64±0.84 | 36.24±3.59 | 1.0±0.0 | >26.53 | 0.91±0.1 | 1.0±0.0 | | | | | | | | | | | | |
| 199.52/6.04 | 1.24±0.11 | <0.038 | -19.87±0.46 | 9.97±1.39 | 0.8±0.4 | >32.53 | 0.33±0.07 | 1.0±0.0 | | | | | | | | | | | | |
| 199.52/6.04 | 199.52/6.04 | <0.067 | -7.82±0.07 | 6.22±0.27 | 0.83±0.2 | >99.95 | 1.13±0.1 | 0.5±0.29 | 3.57±0.37 | <0.055 | -10.09±2.83 | 28.33±3.64 | >64.8 | 1.96±0.32 | 0.5±0.29 | | | | | |
| 199.52/6.04 | 24.89±0.99 | <0.084 | 8.13±0.16 | 12.94±0.57 | 1.0±0.0 | >276.45 | 9.22±0.55 | 0.19±0.17 | 5.44±0.23 | <0.067 | -7.99±0.08 | 5.25±0.24 | >80.94 | 0.55±0.03 | 1.0±0.0 | | | | | |
| 199.52/6.04 | 19.27±0.69 | <0.084 | 18.78±0.07 | 8.22±0.36 | 0.83±0.2 | >228.76 | 4.28±0.38 | 0.37±0.27 | 21.13±0.89 | <0.086 | 8.73±0.32 | 16.91±0.74 | >246.39 | 6.93±0.42 | 0.0±0.0 | | | | | |
| 199.52/6.04 | 13.06±0.54 | <0.242 | 33.27±0.21 | 12.67±0.36 | 0.05±0.05 | >53.89 | 3.28±0.18 | 0.16±0.17 | 15.39±0.2 | <0.084 | 18.84±0.1 | 7.66±0.3 | >182.76 | 2.11±0.17 | 0.45±0.29 | | | | | |
| 190.09/-2.17 | 49.35 | 0.2±0.21 | 0.22±0.21 | 1.19±0.47 | 0.0±0.0 | 68.36±1.17 | 2.02±1.17 | 0 | 62.23 | 1.35±0.03 | 0.2±0.01 | 1.14±0.02 | 84.01±7.95 | 2.51±0.25 | 5 | | | | | |
| 190.09/-2.17 | 18.27 | 0.54±0.25 | 1.92±4.11 | 13.61±3.45 | 0.05±0.08 | 43.78±3.4 | 6.45±3.44 | 0 | 13.76 | 0.54±0.01 | 2.04±0.27 | 13.87±0.27 | 32.97±15.08 | 4.79±2.21 | 1 | | | | | |
| 190.09/-2.17 | 44.42 | 0.66±0.3 | 2.84±0.58 | 2.3±1.52 | 0.0±0.0 | 91.94±1.14 | 2.71±2.18 | 2 | 67.38 | 0.67±0.02 | 2.48±0.11 | 2.46±0.11 | 138.0±20.38 | 4.39±0.69 | 2 | | | | | |
| 190.09/-2.17 | 60.33 | 0.66±0.41 | 5.44±0.6 | 2.12±1.68 | 0.0±0.0 | 124.87±1.73 | 3.38±3.42 | 6 | 68.55 | 0.65±0.02 | 5.47±0.04 | 1.92±0.09 | 143.42±16.26 | 3.47±0.45 | 0 | | | | | |
| 190.09/-2.17 | 80.57 | 0.92±0.48 | 9.23±0.3 | 1.63±0.89 | 0.0±0.0 | 133.96±3.39 | 3.91±2.94 | 4 | 103.3 | 0.89±0.02 | 13.46±0.02 | 7.41±0.09 | 108.19±1.8 | 20.08±0.49 | 6 | | | | | |
| 190.09/-2.17 | 74.44 | 1.3±0.26 | 13.53±0.96 | 7.19±1.4 | 0.0±0.0 | 102.33±2.1 | 18.59±1.8 | 5 | 78.41 | 1.29±0.02 | 16.11±0.01 | 1.7±0.03 | 50.71±3.52 | 4.65±0.36 | 4 | | | | | |
| 190.09/-2.17 | 81.01 | 2.65±1.8 | 16.13±0.25 | 1.72±0.55 | 0.0±0.0 | 87.17±0.88 | 7.7±5.8 | 5 | 47.56 | 2.78±0.09 | 2.1±0.29 | 5.29±0.61 | >188.29 | 1.81±0.4 | 0.68±0.01 | | | | | |
| 190.09/-2.17 | - | - | - | - | - | - | - | - | 17.61±3.33 | <0.094 | 3.49±0.27 | 39.14±0.93 | >57.97 | 5.4±0.48 | 0.53±0.01 | | | | | |
| 190.09/-2.17 | - | - | - | - | - | - | - | - | 7.12±0.61 | <0.123 | 5.08±0.35 | 7.34±1.08 | >32.16 | 3.5±0.01 | 0.3±0.01 | | | | | |
| 190.09/-2.17 | 174.49±3.1 | <0.199 | 7.77±0.04 | 18.14±0.05 | 0.12±0.0 | >875.25 | 64.83±1.17 | 0.0±0.0 | 133.94±6.25 | <0.221 | 8.26±0.32 | 18.53±0.19 | >605.62 | 48.13±1.95 | 0.08±0.01 | | | | | |
| 190.09/-2.17 | 50.84±3.84 | <0.143 | 11.58±0.16 | 3.74±0.35 | 0.0±0.0 | >366.27 | 3.69±0.45 | 0.0±0.0 | 52.48±3.91 | <0.209 | 10.42±0.22 | 3.81±0.41 | >251.49 | 3.88±0.51 | 0.21±0.01 | | | | | |
| 177.3/-22.24 | 13.89 | 0.4±0.09 | -0.39±0.25 | 2.3±0.47 | 0.34±0.28 | 42.01±2.11 | 0.88±0.29 | 2 | 11.1 | 0.28±0.01 | -0.48±0.01 | 1.74±0.04 | 45.47±2.68 | 0.43±0.03 | 0 | | | | | |
| 177.3/-22.24 | 27.45 | 0.76±0.05 | 4.0±0.21 | 4.81±0.89 | 0.0±0.0 | 51.56±4.09 | 3.67±0.78 | 0 | 49.69 | 0.76±0.0 | 4.59±0.05 | 7.37±0.09 | 93.34±4.68 | 10.15±0.53 | 2 | | | | | |
| 177.3/-22.24 | - | - | - | - | - | - | - | - | 37.76 | 1.66±0.09 | 8.08±0.03 | 1.27±0.05 | 46.62±1.28 | 3.191±0.14 | 1 | | | | | |
| 177.3/-22.24 | - | - | - | - | - | - | - | - | 44.68 | 3.41±0.17 | 9.91±0.03 | 1.71±0.05 | 46.21±0.88 | 5.23±0.33 | 1 | | | | | |
| 177.3/-22.24 | 34.57 | 3.4±0.31 | 9.56±0.09 | 3.43±0.17 | 0.04±0.02 | 35.76±1.21 | 8.27±0.91 | 1 | 42.15 | 1.13±0.11 | 10.47±0.16 | 3.45±0.11 | 62.27±2.33 | 4.72±0.52 | 4 | | | | | |
| 177.3/-22.24 | - | <0.093 | -22.83±0.16 | 9.91±0.56 | 1.0±0.0 | >35.66 | 0.95±0.07 | 1.0±0.0 | 2.1 | 0.093 | -22.94±0.13 | 5.17±0.29 | >32.67 | 0.31±0.03 | 1.0±0.0 | | | | | |
| 177.3/-22.24 | 4.99±0.58 | <0.109 | -1.47±0.75 | 13.98±1.22 | 1.0±0.0 | >45.82 | 2.0±0.29 | 0.5±0.18 | 2.1±0.09 | <0.03 | -8.57±0.64 | 47.69±1.07 | >70.76 | 1.94±0.1 | 0.51±0.04 | | | | | |
| 177.3/-22.24 | 51.41±2.48 | <0.071 | 5.34±0.22 | 8.07±0.38 | 0.0±0.0 | >726.96 | 8.05±0.54 | 0.44±0.1 | 6.76±1.73 | <0.086 | 4.17±0.15 | 3.38±0.67 | >78.34 | 0.44±0.14 | 0.61±0.03 | | | | | |
| 177.3/-22.24 | 20.37±0.98 | <0.065 | 12.06±0.06 | 3.5±0.14 | 0.96±0.07 | >311.64 | 2.02±0.13 | 0.7±0.15 | 8.44±1.07 | <0.09 | 5.55±0.19 | 15.87±0.72 | >93.34 | 2.64±0.35 | 0.36±0.03 | | | | | |
| 206.72/8.44 | 8.06 | 0.18±0.02 | -18.29±0.46 | 9.64±1.02 | 0.08±0.2 | 48.91±3.65 | 1.74±0.35 | 0 | 23.59±2.95 | <0.07 | 9.52±0.23 | 5.97±0.42 | >336.31 | 2.73±0.39 | 0.27±0.04 | | | | | |
| 206.72/8.44 | 5.44 | 0.07±0.01 | 5.22±0.71 | 11.8±1.59 | 0.0±0.0 | 80.46±32.83 | 1.3±0.59 | 1 | 8.98 | 0.22±0.0 | -17.08±0.03 | 8.2±0.07 | 45.46±4.29 | 1.56±0.15 | 0 | | | | | |
| 206.72/8.44 | 1.85 | 0.05±0.01 | 39.86±0.53 | 5.56±1.21 | 0.0±0.0 | 37.99±8.62 | 0.19±0.07 | 2 | 13.88 | 0.07±0.0 | 39.84±0.11 | 5.64±0.26 | 46.0±4.52 | 3.4±0.49 | 1 | | | | | |
| 206.72/8.44 | 3.13±0.54 | <0.127 | -16.08±0.31 | 4.14±0.74 | 0.0±0.0 | >24.74 | 0.25±0.06 | 0.54±0.42 | 3.7±0.89 | <0.107 | -16.85±2.05 | 18.92±1.68 | >34.54 | 1.36±0.35 | 0.5±0.41 | | | | | |
| 206.72/8.44 | 3.06±1.31 | <0.058 | -0.09±34.87 | 32.16±16.07 | 0.0±0.0 | >52.42 | 1.91±1.26 | 0.46±0.39 | 6.23±3.41 | <0.038 | -5.26±1.88 | 8.03±2.89 | >162.18 | 0.97±0.64 | 1.0±0.0 | | | | | |
| 206.72/8.44 | 20.46±4.82 | <0.077 | 1.09±0.24 | 10.87±0.97 | 0.71±0.14 | >266.77 | 5.76±1.48 | 0.0±0.0 | 14.54±3.78 | <0.072 | 0.76±0.73 | 7.63±0.92 | >201.28 | 2.15±0.62 | 0.5±0.41 | | | | | |
| 206.72/8.44 | 3.36±1.82 | <0.041 | 13.88±1.71 | 11.96±5.05 | 0.0±0.0 | >81.94 | 0.78±0.53 | 1.0±0.0 | 7.12±0.51 | <0.041 | 15.39±0.61 | 15.2±1.97 | >174.23 | 2.1±0.31 | 1.0±0.0 | | | | | |
| 206.72/8.44 | 5.05±2.03 | <0.033 | 33.78±10.02 | 34.87±6.65 | 0.0±0.0 | >151.57 | 3.42±1.52 | 0.33±0.35 | 7.94±0.44 | <0.035 | 35.76±0.62 | 20.27±1.98 | >220.48 | 3.12±0.35 | 0.5±0.41 | | | | | |
| 206.72/8.44 | 3.32±1.42 | <0.041 | 37.78±11.06 | 13.04±3.2 | 0.33±0.37 | >81.13 | 0.97±0.5 | 0.48±0.43 | 1.34±0.54 | <0.028 | 53.54±4.82 | 20.94±4.5 | >47.57 | 0.54±0.25 | 0.5±0.41 | | | | | |
| 194.89/-11.98 | 17.52 | 0.24±0.07 | -3.45±0.34 | 3.43±0.87 | 1.0±0.0 | 82.1±3.44 | 1.9±0.73 | 3 | 14.48 | 0.19±0.0 | -3.58±0.05 | 5.22±0.13 | 83.68±3.61 | 1.64±0.09 | 0 | | | | | |
| 194.89/-11.98 | 22.22 | 0.41±0.05 | 3.21±0.2 | 3.23±0.43 | 0.0±0.0 | 66.06±3.77 | 1.71±0.32 | 2 | 13.55 | 0.45±0.01 | 3.18±0.03 | 3.49±0.07 | 37.4±16.13 | 1.13±0.49 | 4 | | | | | |
| 194.89/-11.98 | 16.59 | 0.6±0.05 | 9.69±0.25 | 4.79±0.52 | 1.0±0.0 | 36.77±3.69 | 3.05±0.51 | 0 | 5.22 | 0.19±0.02 | 9.18±0.06 | 2.0±0.19 | 30.18±10.28 | 0.22±0.08 | 3 | | | | | |
| 194.89/-11.98 | 20.05 | 0.49±0.4 | 12.84±0.25 | 1.68±0.74 | 0.0±0.0 | 51.75±2.01 | 0.83±0.76 | 3 | 37.1 | 0.5±0.02 | 11.36±0.07 | 8.68±0.16 | 94.29±2.62 | 7.87±0.39 | 1 | | | | | |
| 194.89/-11.98 | 15.68 | 0.29±0.15 | 14.57±1.72 | 3.29±2.24 | 0.0±0.0 | 62.27±3.27 | 1.16±0.98 | 1 | 16.1 | 0.37±0.02 | 13.11±0.03 | 1.92±0.1 | 62.05±1.86 | 0.72±0.05 | 2 | | | | | |
| 194.89/-11.98 | 2.7±0.07 | <0.037 | -26.63±0.18 | 13.22±0.58 | 1.0±0.0 | >73.26 | 1.02±0.05 | 1.0±0.0 | 2.03±0.11 | <0.033 | -26.28±0.15 | 7.19±0.45 | >51.77 | 0.28±0.02 | 1.0±0.0 | | | | | |
| 194.89/-11.98 | 24.75±1.88 | <0.078 | 1.99±0.39 | 9.84±0.25 | 1.0±0.0 | >316.15 | 6.97±0.56 | 0.45±0.04 | 2.19±0.18 | <0.047 | -8.73±1.16 | 58.69±1.83 | >46.19 | 2.49±0.22 | 0.31±0.03 | | | | | |
| 194.89/-11.98 | - | - | - | - | - | - | - | - | 19.33±5.99 | <0.115 | 2.66±0.59 | 5.68±0.36 | >167.56 | 2.13±0.67 | 0.98±0.01 | | | | | |
| 194.89/-11.98 | - | - | - | - | - | - | - | - | 14.91±4.03 | <0.114 | 6.95±0.44 | 4.26±0.85 | >131.33 | 1.23±0.41 | 0.58±0.03 | | | | | |
| 194.89/-11.98 | 47.58±2.76 | <0.076 | 9.7±0.14 | 9.02±0.32 | 0.0±0.0 | >624.88 | 8.33±0.57 | 0.0±0.0 | 12.45±1.04 | <0.102 | 7.77±0.19 | 23.98±0.88 | >122.32 | 5.79±0.53 | 0.0±0.0 | | | | | |
| 194.89/-11.98 | 12.55±0.58 | <0.059 | 19.25±0.1 | 5.47±0.15 | 1.0±0.0 | >212.66 | 1.97±0.11 | 0.5±0.04 | 5.44±0.27 | <0.045 | 19.94±0.07 | 3.38±0.19 | >120.38 | 0.36±0.03 | 0.43±0.04 | | | | | |

TABLE 3 (CONT)

| l/b ($^{\circ}$) | pseudo-Voigt | | | | | Gaussian | | | | | F or O | | | | |
|-----------------------|--------------|-------------------------|-------------------------------------|--------------------------------------|-----------|--------------|--|-----------|--------------|-------------------------|-------------|-------------------------------------|--------------------------------------|--------------|--|
| | T_B (K) | τ (10^{-2}) | V_{lsr} (km s^{-1}) | ΔV (km s^{-1}) | η | T_s (K) | NH I (10^{20} cm^{-2}) | F or O | T_B (K) | τ (10^{-2}) | | V_{lsr} (km s^{-1}) | ΔV (km s^{-1}) | T_s (K) | NH I (10^{20} cm^{-2}) |
| 209.24/-4.64 | 44.35 | 1.13±0.12 | 8.89±0.23 | 6.92±0.43 | 0.0±0.0 | 65.52±4.98 | 9.9±1.46 | 1 | 65.45 | 0.98±0.01 | 7.45±0.04 | 5.09±0.06 | 104.78±1.42 | 10.16±0.2 | 1 |
| 209.24/+4.64 | 72.72 | 2.21±1.56 | 10.81±0.18 | 1.25±0.42 | 0.0±0.0 | 81.68±1.51 | 4.35±3.41 | 0 | 75.94 | 2.32±0.04 | 10.78±0.01 | 1.86±0.03 | 84.22±0.77 | 7.06±0.18 | 4 |
| 209.24/-4.64 | 27.06 | 1.22±0.16 | 22.6±0.11 | 3.16±0.32 | 0.32±0.15 | 38.4±2.02 | 3.3±0.6 | 2 | 20.04 | 0.32±0.01 | 14.01±0.04 | 3.17±0.09 | 73.17±6.19 | 1.43±0.13 | 0 |
| 209.24/+4.64 | 8.81 | 0.19±0.11 | 37.69±0.46 | 1.7±1.16 | 0.0±0.0 | 50.93±7.74 | 0.33±0.29 | 3 | 26.89 | 1.15±0.01 | 22.58±0.01 | 3.46±0.02 | 39.35±2.63 | 3.03±0.21 | 3 |
| 209.24/-4.64 | 13.48 | 0.33±0.1 | 40.16±0.3 | 1.71±0.83 | 1.0±0.0 | 47.95±4.38 | 0.77±0.45 | 4 | 23.68 | 0.24±0.01 | 37.77±0.03 | 1.93±0.07 | 110.96±3.15 | 1.02±0.05 | 5 |
| 209.24/+4.64 | 159.0±10.63 | <0.206 | 8.69±0.05 | 8.31±0.17 | 0.44±0.01 | >770.87 | 30.95±2.17 | 0.04±0.04 | 22.84 | 0.33±0.01 | 40.18±0.02 | 1.53±0.04 | 81.27±2.18 | 0.79±0.04 | 2 |
| 209.24/-4.64 | 37.48±1.26 | <0.15 | 20.29±0.14 | 7.8±0.24 | 0.26±0.22 | >249.72 | 6.36±0.65 | 0.43±0.08 | 83.56±2.08 | <0.175 | 9.28±0.1 | 10.95±0.14 | >477.29 | 17.75±0.5 | 0.28±0.03 |
| 209.24/+4.64 | - | - | - | - | - | - | - | - | 43.59±2.07 | <0.167 | 21.41±0.11 | 5.85±0.17 | >260.55 | 4.94±0.27 | 0.2±0.03 |
| 209.24/-4.64 | - | - | - | - | - | - | - | - | 17.11±0.55 | <0.095 | 25.67±0.2 | 46.12±0.37 | >179.88 | 15.31±0.51 | 0.39±0.04 |
| 209.24/+4.64 | 23.14±1.34 | <0.129 | 38.62±0.14 | 6.53±0.28 | 0.0±0.0 | >178.74 | 2.93±0.21 | 0.33±0.08 | 17.11±0.55 | <0.095 | 25.67±0.2 | 46.12±0.37 | >179.88 | 15.31±0.51 | 0.39±0.04 |
| 209.24/-4.64 | 28.43±1.06 | <0.155 | 39.79±0.54 | 28.19±0.79 | 0.0±0.0 | >183.37 | 15.54±0.73 | 0.22±0.06 | 35.66±0.43 | <0.089 | 43.16±0.09 | 18.34±0.18 | >398.6 | 12.69±0.2 | 0.49±0.04 |
| 209.24/+4.64 | 16.63±1.08 | <0.121 | 46.71±0.27 | 10.62±0.58 | 0.0±0.0 | >137.46 | 3.43±0.29 | 0.42±0.08 | 4.94 | 0.22±0.01 | -13.76±0.09 | 4.26±0.17 | 25.01±6.7 | 0.45±0.12 | 4 |
| 209.24/-4.64 | 3.91 | 0.16±0.06 | -14.09±0.5 | 3.04±1.26 | 0.22±1.33 | 26.42±7.06 | 0.28±0.24 | 3 | 21.17 | 0.44±0.03 | -8.73±0.04 | 3.15±0.14 | 59.46±4.56 | 1.59±0.19 | 1 |
| 174.77/-5.97 | 21.63 | 0.49±0.12 | -8.46±0.37 | 4.14±1.37 | 1.0±0.0 | 55.85±4.97 | 3.26±1.95 | 2 | 34.5 | 0.2±0.05 | -2.9±2.33 | 8.54±4.49 | 190.33±77.74 | 6.34±4.53 | 0 |
| 174.77/+5.97 | 18.93 | 0.54±0.05 | 1.32±0.36 | 6.52±0.86 | 0.0±0.0 | 45.36±2.96 | 3.09±0.54 | 0 | 28.98 | 0.49±0.16 | 1.97±0.19 | 5.32±0.6 | 74.82±2.98 | 3.74±1.34 | 0 |
| 174.77/-5.97 | 28.02 | 0.58±0.1 | 5.84±0.11 | 1.57±0.32 | 0.0±0.0 | 63.67±1.06 | 1.13±0.31 | 1 | 23.66 | 0.6±0.02 | 5.85±0.02 | 1.65±0.05 | 52.44±2.45 | 1.01±0.06 | 0 |
| 174.77/+5.97 | 1.45±0.34 | <0.089 | -28.16±0.42 | 4.33±1.24 | 0.0±0.0 | >16.38 | 0.12±0.04 | 1.0±0.0 | 18.9±0.26 | <0.117 | -14.11±0.29 | 34.79±0.34 | >155.88 | 12.35±0.21 | 0.19±0.03 |
| 174.77/-5.97 | 1.64±0.79 | <0.091 | -20.0±0.51 | 4.38±1.63 | 0.17±1.97 | >17.91 | 0.15±0.16 | 0.5±0.08 | 27.07±2.64 | <0.137 | -10.45±0.18 | 7.24±0.19 | >197.73 | 3.8±0.38 | 0.48±0.04 |
| 174.77/+5.97 | 16.69±0.88 | <0.121 | -13.61±0.21 | 36.43±0.54 | 0.0±0.0 | >138.36 | 11.79±0.65 | 0.17±0.05 | 20.6±13.3 | <0.13 | 2.51±3.69 | 13.31±2.33 | >158.51 | 5.32±3.56 | 0.51±0.04 |
| 174.77/-5.97 | 28.31±1.77 | <0.132 | -9.58±0.17 | 7.93±0.36 | 0.0±0.0 | >214.17 | 4.36±0.34 | 0.4±0.08 | 15.53 | 0.29±0.0 | 6.56±0.03 | 4.28±0.47 | >133.38 | 1.38±0.37 | 0.43±0.04 |
| 174.77/+5.97 | 59.81±1.74 | <0.158 | 0.91±0.08 | 11.2±0.2 | 0.0±0.0 | >378.64 | 13.0±0.44 | 0.0±0.0 | 2.99 | 0.14±0.0 | 36.13±0.04 | 2.55±0.09 | 22.88±2.13 | 0.10±0.02 | 0 |
| 174.77/-5.97 | 21.05 | 0.33±0.05 | 6.36±0.2 | 3.33±0.67 | 0.68±0.36 | 74.89±38.25 | 2.09±1.22 | 0 | 16.58±4.09 | <0.124 | 5.57±0.17 | 4.38±0.06 | 61.7±18.71 | 1.52±0.46 | 0 |
| 203.85/+5.82 | 3.35 | 0.14±0.03 | 36.11±0.2 | 2.63±0.44 | 0.0±0.0 | 25.62±2.2 | 0.18±0.05 | 1 | 2.99 | 0.14±0.0 | 36.13±0.04 | 2.55±0.09 | 22.88±2.13 | 0.10±0.02 | 0 |
| 203.85/-5.82 | 2.47±0.17 | <0.046 | -8.54±0.12 | 3.67±0.47 | 1.0±0.0 | >53.7 | 0.26±0.04 | 1.0±0.0 | 2.04±0.17 | <0.047 | -8.75±0.12 | 3.5±0.35 | >43.87 | 1.14±0.02 | 0 |
| 203.85/+5.82 | 203.85±5.82 | - | - | - | - | - | - | - | 3.35±0.98 | <0.045 | 2.35±2.39 | 18.83±3.84 | >74.07 | 1.22±0.43 | 0.5±0.41 |
| 203.85/-5.82 | 13.96±6.4 | <0.119 | 7.88±0.36 | 3.98±1.53 | 0.79±0.63 | >116.93 | 1.48±0.94 | 0.5±0.41 | 15.67±2.41 | <0.131 | 9.14±0.61 | 5.87±0.77 | >119.61 | 1.79±0.36 | 0.34±0.41 |
| 203.85/+5.82 | 9.52±5.29 | <0.204 | 10.44±1.72 | 4.17±1.53 | 0.0±0.0 | >46.56 | 0.77±0.51 | 0.5±0.41 | - | - | - | - | - | - | - |
| 203.85/-5.82 | 13.12±0.52 | <0.218 | 10.58±0.41 | 32.71±0.75 | 0.06±0.05 | >60.13 | 8.58±0.43 | 0.5±0.41 | 12.95±1.04 | <0.05 | 16.65±0.31 | 40.93±0.53 | >254.62 | 10.28±0.84 | 0.5±0.41 |
| 203.85/+5.82 | 12.29±0.46 | <0.082 | 25.12±0.12 | 9.14±0.33 | 0.0±0.0 | >150.81 | 2.18±0.11 | 1.0±0.0 | 10.92±0.61 | <0.082 | 25.18±0.13 | 8.71±0.34 | >133.99 | 1.85±0.13 | 0.0±0.0 |
| 203.85/-5.82 | 13.17±0.27 | <0.056 | 36.46±0.19 | 15.03±0.33 | 0.43±0.04 | >236.31 | 4.62±0.16 | 0.5±0.41 | 8.88±0.36 | <0.062 | 36.73±0.19 | 12.57±0.38 | >143.59 | 2.17±0.11 | 0.5±0.41 |
| 172.23/-25.66 | 5.32 | 0.11±0.35 | -0.92±1.11 | 2.28±2.17 | 0.0±0.0 | 51.09±4.55 | 0.26±0.82 | 1 | 20.97 | 0.36±0.0 | 0.8±0.06 | 4.18±0.1 | 69.36±9.8 | 2.01±0.29 | 0 |
| 172.23/+25.66 | 18.33 | 0.33±0.09 | 1.36±1.48 | 3.8±2.67 | 0.0±0.0 | 65.22±3.77 | 1.58±1.18 | 0 | 2.39 | 0.11±0.06 | 5.3±1.35 | 3.16±1.79 | 22.99±46.32 | 0.16±0.35 | 0.55±0.31 |
| 172.23/-25.66 | 9.52±5.29 | <0.204 | 10.44±1.72 | 4.17±1.53 | 0.0±0.0 | >46.56 | 0.77±0.51 | 0.5±0.41 | 14.61 | 0.27±0.14 | 6.75±0.05 | 1.88±0.29 | 61.76±3.68 | 0.69±0.34 | 1 |
| 172.23/+25.66 | 11.25 | 0.33±0.05 | 6.54±0.19 | 2.63±0.58 | 0.21±1.09 | 41.08±9.46 | 0.73±0.43 | 2 | 16.27 | 0.31±0.01 | 9.93±0.05 | 2.9±0.08 | 61.04±7.86 | 1.07±0.14 | 3 |
| 172.23/-25.66 | 11.57 | 0.33±0.06 | 10.02±0.17 | 2.33±0.48 | 0.57±0.44 | 41.18±3.69 | 0.77±0.25 | 3 | 0.66±0.04 | <0.027 | -40.32±2.18 | 32.02±3.94 | >24.48 | 0.41±0.06 | 1.0±0.0 |
| 172.23/+25.66 | 0.67±0.04 | <0.019 | -38.84±2.33 | 35.81±4.8 | 0.08±0.47 | >34.46 | 0.48±0.13 | 1.0±0.0 | - | - | - | - | - | - | - |
| 172.23/-25.66 | 3.38±0.55 | <0.071 | -0.56±1.18 | 28.06±1.61 | 0.0±0.0 | >47.6 | 1.84±0.32 | 0.5±0.29 | 3.6±0.49 | <0.069 | -0.27±0.97 | 30.68±1.75 | >62.23 | 2.14±0.31 | 0.55±0.31 |
| 172.23/+25.66 | 12.03±4.11 | <0.089 | 3.58±0.12 | 3.55±0.9 | 1.0±0.0 | >135.67 | 1.22±0.52 | 0.43±0.28 | 23.5±4.62 | <0.078 | 3.76±0.82 | 5.8±0.9 | >300.58 | 2.64±0.66 | 0.0±0.0 |
| 172.23/-25.66 | 24.32±4.35 | <0.072 | 5.34±0.09 | 11.92±0.51 | 0.08±0.08 | >336.86 | 5.83±1.09 | 0.43±0.27 | 16.02±3.06 | <0.073 | 5.18±0.16 | 13.51±0.94 | >219.19 | 4.2±0.85 | 0.0±0.0 |
| 172.23/+25.66 | 11.71±2.03 | <0.054 | 10.49±0.18 | 3.79±0.3 | 0.0±0.0 | >216.21 | 0.86±0.19 | 0.48±0.29 | 11.96±2.9 | <0.059 | 10.3±0.46 | 4.93±0.35 | >203.64 | 1.14±0.29 | 0.49±0.29 |
| 206.48/+5.48 | 2.34 | 0.09±0.07 | -2.79±0.4 | 2.77±0.83 | 0.0±0.0 | 27.24±3.0 | 1.33±0.06 | 0 | 2.57 | 0.08±0.0 | -2.74±0.08 | 3.09±0.18 | 33.38±3.1 | 0.17±0.02 | 0 |
| 206.48/-5.48 | 20.93 | 0.59±0.07 | 7.33±0.11 | 2.32±0.31 | 0.25±0.26 | 46.96±1.0 | 0.19±0.29 | 1 | 22.01 | 0.56±0.01 | 7.32±0.01 | 2.52±0.03 | 51.32±0.83 | 1.4±0.03 | 1 |
| 206.48/+5.48 | 2.06 | 0.08±0.04 | 41.4±0.46 | 1.86±1.03 | 0.0±0.0 | 66.77±5.02 | 3.91±0.34 | 0.33±0.35 | 2.11 | 0.08±0.01 | 41.38±0.07 | 1.94±0.15 | 27.38±5.03 | 0.08±0.02 | 2 |
| 206.48/-5.48 | 15.4±0.86 | <0.117 | 5.35±0.1 | 1.01±0.38 | 0.39±0.15 | >131.39 | 0.91±0.34 | 0.22±0.06 | 13.22±0.25 | <0.129 | 5.2±0.08 | 10.05±0.23 | >102.11 | 2.58±0.08 | 0.49±0.43 |
| 206.48/+5.48 | 13.28±0.82 | <0.057 | 19.07±0.6 | 39.13±0.61 | 0.09±0.04 | >231.65 | 10.51±0.7 | 0.39±0.42 | 16.17±0.17 | <0.057 | 19.0±0.2 | 39.88±0.27 | >282.11 | 12.51±0.16 | 0.17±0.25 |
| 206.48/-5.48 | 6.43±0.74 | <0.113 | 22.54±0.21 | 6.31±0.91 | 1.0±0.0 | >57.01 | 1.16±0.21 | 1.0±0.0 | 4.41±0.29 | <0.125 | 22.46±0.15 | 4.28±0.35 | >35.27 | 0.37±0.04 | 1.0±0.0 |
| 206.48/+5.48 | 10.26±1.07 | <0.077 | 29.5±0.09 | 6.33±0.43 | 0.13±0.41 | >133.42 | 29.4±0.09 | 1.0±0.0 | 10.03±0.32 | <0.077 | 29.4±0.09 | 6.57±0.27 | >130.4 | 1.28±0.07 | 1.0±0.0 |
| 206.48/-5.48 | 11.94±0.5 | <0.075 | 39.38±0.37 | 15.11±0.6 | 0.0±0.0 | >159.08 | 3.5±0.2 | 0.11±0.22 | 10.81±0.21 | <0.088 | 39.71±0.19 | 14.21±0.45 | >122.58 | 2.98±0.11 | 0.17±0.25 |

